NORTHWESTERN UNIVERSITY

Studies of Structure and Behavior in Polymer Thin Films: Insights Into Self-Assembly and Thermodynamic Stability

A DISSERTATION

SUBMITTED TO THE GRADUATE SCHOOL

IN PARTIAL FULFILLMENT OF THE REQUIREMENTS

for the degree

DOCTOR OF PHILOSOPHY

Field of Materials Science and Engineering

By

Yan Sun

EVANSTON, ILLINOIS

June 2011

ABSTRACT

Studies of Structure and Behavior in Polymer Thin Films: Insights Into Self-Assembly and Thermodynamic Stability

Yan Sun

Polymer thin films have become an important part of our everyday lives and are ubiquitous in countless industrial and biomedical applications. Nevertheless, new discoveries about their structure, properties, and behavior are still being made. This thesis engages in an exploration of two major topics in the subject of polymer thin films: 1) Thermodynamic stability and dewetting involving homopolymer films, and 2) Self-assembly and ordering of nanostructures in block copolymer films. While a broad understanding of each these topics has already been established in the scientific community, there are still numerous practical questions that emerge when specific systems are considered. This research extends the current understanding of polymer thin films by actively applying what is known theoretically and experimentally in a methodical way to analyze these specific systems. In the first study, the stability and dewetting of a poly(4-bromostyrene) (PBrS) film prepared on a top of a solid substrate are investigated. To control its behavior, a secondary poly(4-vinyl pyridine) (P4VP) film is inserted underneath. By systematically varying the

thicknesses of both the PBrS and P4VP layers, the Helmholtz free energy curve, determined by a combination of long and short-range interactions that drive the dewetting, is tuned. Results from x-ray standing waves generated via total external reflection from an x-ray mirror, time-of-flight secondary ion mass spectroscopy, optical microscopy, and atomic force microscopy are combined to construct the full free energy curve and conclude that the dewetting in this system is autophobic. In the second study, the ability of a poly(methacrylic acid)-poly(methyl methacrylate) (PMAA-PMMA) amphiphilic diblock copolymer film to self-assemble into well-ordered nanostructures is investigated. Due to complications associated with direct solvent and thermal annealing of this diblock, a complex method involving reactive annealing is applied. Here, a precursor poly(*tert*-butyl methacrylate)-poly(methyl methacrylate) (P*t*BMA-PMMA) diblock film is first solvent annealed to induce ordering, which is then followed by thermal deprotection to convert the P*t*BMA block to PMAA. Results from thermogravimetric analysis, atomic force microscopy, x-ray reflectivity, and grazing-incidence small-angle x-ray scattering reveal that ordered morphologies may be retained with a certain amount of conversion, though upon reaching full conversion, the structure becomes more disordered.

Acknowledgements

While this section tucked in the beginning may be the least important to the reader, it is well worth the time to take a moment and look back at my past five years that helped harvest the content presented in this thesis. Coming in as a physics and applied math graduate from the University of Chicago, I knew virtually nothing about polymers (other than the fact that they are found in plastic bottles) before I began my Ph.D. studies at Northwestern. But there was one thing I was sure of: I wanted to engage in challenging experimental work to study these ubiquitous materials, knowing that there are countless applications out there that require a better understanding of their fundamental properties. The start of my research was slow and perhaps aimless, but sooner than expected my goals became clear and I knew where I was headed. My overall experience working with polymer thin films was a rewarding one that allowed me to focus on several interesting problems in this area and learn a number of powerful, state-of-the-art characterization techniques. It has truly been a privilege working at Argonne National Laboratory. Not only did I have a lot of success in examining my polymers with synchrotron x-rays, but I also had the opportunity to learn all I ever wanted to know about how x-rays interact with matter.

My time as a graduate student would not have been smooth and productive without some of the greatest individuals that will undoubtedly be on my mind for the rest of my life. First and foremost, I must express my deepest thanks to my advisors Professor Ken Shull and Dr. Jin Wang. I am truly moved by their kindness and devotion in guiding

me through the complex worlds of polymers and x-rays. The most important thing they have taught me is to never give up in research and in life, and I will always look up to them as role models. Ken was always encouraged by my work, no matter how strange or baffling the results were, and always offered me advice, no matter how busy he was. Jin was always enthusiastic to hear from me and patiently guided me forward through my projects, no matter how difficult they turned out to be. I am also thankful for my committee members, Professor Michael Bedzyk and Professor Monica Olvera de la Cruz, who have always supported my research and provided useful feedback and ideas.

Research becomes so much more meaningful when you can discuss it with other people every day. With that said, I would like to thank all of the past and current Shull group members for being around me all these years. This is indeed a family where everyone helps and encourages each other. My research would not have jump-started without the help of Rafael Bras and Aleta Hagman. Working with Rafael at Northwestern and Argonne during my first two years really got me up to speed with the experiments that can be done to study polymers as he was eager to try out all sorts of instruments and techniques. It has also been wonderful the last three years working with Kevin Henderson, who has provided some really great ideas, collaborated with me on several x-ray-related projects at Argonne, and was always eager to make things happen.

My x-ray experiments at Argonne would not have been successful with the incredible beamline scientists and staff at the Advanced Photon Source. Sector 7 has been my second office for the past five years. Don Walko and Dohn Arms have devoted so much time and effort in helping me set up for my XSW experiments that I do not even know how to thank them for what they have done. Harold Gibson has always made my day a

Finally and most importantly, I am deeply grateful to my parents who were always close by me during my graduate school years. They supported me in everything I did. During times when things in life were not going so well, they were the ones who gave me the needed encouragement that helped me move on. I am very fortunate for that and I owe it all to them. Now that I am about to mark another major milestone in my life, I am proud to keep these five exciting years of graduate school in my recollection. If it were not for the amazing people around me, my advisors, group members, scientists at Argonne, family, and friends, such a colorful memory would not have been created. I definitely made the right decision to pursue a Ph.D. because I can feel how this experience has nourished me, helped test and reflect my potentials, and made me the person I am today who is prepared to solve more critical scientific and technical problems facing society.

My graduate school experience was filled with moments of joy, pride, frustration, and disappointment, but most of all, it was simply delightful and rewarding. Now I'm eagerly looking forward to my next experience. As the famous writer Ralph Waldo Emerson once said, "Life is a journey, not a destination." I am a big believer in that.

Table of Contents

List of Tables

List of Figures

CHAPTER 1

Introduction

1.1. Research Motivation

Polymer thin films are a novel class of materials that have found their way into a wide range of industrial and biomedical applications and are now an integral part of our everyday lives. Their universal presence in paints, coatings, packaging, adhesives, dielectrics, and other common entities has firmly established their versatility, integrity, and dependability. At the same time, their continuing expansion into new technologies and applications has inevitably revealed potential shortcomings and subtleness in their properties and behavior.

To begin with, thermodynamic stability is not always guaranteed, and as design requirements for products become more and more complex, so does the ability to keep the geometry stable under a variety of processing and performance conditions. Experimental testing must certainly be complemented with theoretical predictions in order to generate the complete picture. However, the subtleness in the way polymer thin films behave can often result in misinterpretations, ultimately misguiding the formulation of strategies for maintaining stability in the system. Therefore, a delicate, methodical way of preparing, processing, and analyzing the films must be adopted. The first half of this research engages in a comprehensive study on the stability and dewetting of a model polymer multilayer film, utilizing a systematic approach to develop a full understanding of its behavior.

Secondly, it is well known that block copolymer thin films can phase-separate and elegantly self-assemble into a variety of highly ordered nanostructures. However, there are still limitations to this unconventional lithographic technique. In particular, processing procedures to induce ordering in a number of important block copolymer films are rather nontrivial and require strategic approaches to mobilize their kinetically trapped structure. Amphiphilic block copolymers, in particular, are problematic in that they tend to form spherical micelles in a variety of solvents, rendering them difficult for further manipulation in the melt. The second half of this research highlights the challenges faced in processing a model amphiphilic diblock film, where a scheme involving reactive annealing is evaluated.

Access to the latest high-resolution instruments and the ability to perform real-time, *in situ* measurements have also driven the motivation for taking an in-depth look at these two major established topics in polymer thin film research mentioned above. The power and effectiveness of these novel materials characterization methods can help gain insight into new information that previous experiments have not been able to obtain. These techniques especially involve those that take advantage of synchrotron radiation performed at the Advanced Photon Source at Argonne National Laboratory, which are highlighted in an independent chapter in this thesis.

1.2. Outline of Objectives and Research

The goal of this research is to explore through specific examples the importance of the problems mentioned in the previous section and reveal some of the most subtle issues that can be encountered in working with polymer thin films. Major emphasis is placed on how the polymer thin films are designed (e.g. thickness and composition) and processed

(e.g. temperature and solvent conditions), which determine their ultimate structure and behavior. Parts of this thesis are more or less intended to serve as a practical guide, informing readers not only what works, but what does not work. The results presented here should hopefully serve as a stepping stone toward building more complex yet reliable systems for applications in industry and for use in more advanced fundamental research.

Chapter 2 provides a general introduction and background into the subjects of stability and dewetting in polymer thin films as well as the self-assembly of nanostructures and phase behavior in block copolymer thin films. Experimental methods that can be used to study these phenomena effectively are summarized.

Chapter 3 focuses on the investigation of the stability and dewetting in a specific model homopolymer multilayer system. The geometry consists of a poly(4-bromostyrene) film on top of a poly(4-vinyl pyridine) film, which together rest on a solid substrate. The top film autophobically dewets the bottom film, which remains stable under all conditions. By systematically varying the thicknesses of both layers, the overall stability and the Helmholtz free energy curve are tuned. A combination of x-ray standing waves generated via total external reflection from an x-ray mirror, time-of-flight secondary ion mass spectroscopy, optical microscopy, and atomic force microscopy is used for this investigation.

Chapter 4 explores the subtle processing challenges involved in achieving ordered morphologies in certain amphiphilic block copolymer thin films. Specifically, the model diblock copolymer poly(methacrylic acid)-poly(methyl methacrylate) is tackled by applying a processing strategy involving the thermal deprotection of poly(*tert*-butyl methacrylate) to form poly(methacrylic acid). The precursor poly(*tert*-butyl methacrylate)-poly(methyl methacrylate) films are first solvent annealed to induce the assembly of highly ordered

nanostructures, which is then followed by the thermal deprotection step. A combination of thermogravimetric analysis, grazing-incidence small-angle x-ray scattering (performed *in situ*) and atomic force microscopy is used for this investigation.

Chapter 5 serves as a practical guide to readers who are interested in using various synchrotron radiation techniques to study the structure and behavior of soft materials. In particular, advice pertaining to sample preparation, experimental setup, data collection, and analysis of results are shared. This chapter also walks through some of the fundamental principles behind the x-ray standing wave and grazing-incidence small-angle x-ray scattering techniques.

Chapter 6 supplies a summary of the main results of this Ph.D. work. Based on the experiments and results discussed in this thesis, a few ideas and suggestions for future follow-up investigations involving polymer thin films, categorized based on x-ray technique, are provided.

CHAPTER 2

Background

This chapter provides a general introduction to two major topics in the subject of polymer thin films: 1) Thermodynamic stability and dewetting, and 2) Self-assembly and phase behavior in block copolymer thin films. Specific case studies for each of these topics are explored in subsequent chapters in the rest of this thesis.

2.1. Thermodynamic Stability and Dewetting in Polymer Thin Films

The inevitable question of stability has always been asked by those who work with polymer thin films. It is a problem that has been heavily investigated both theoretically and experimentally and is faced everyday in any industry that employs polymer thin films for its development of products and technology. In most cases, these films are situated on top of a solid substrate, which is the geometry considered in the following background discussion.

The concept of dewetting is best understood from an energy point of view.[1] All of us in our everyday lives have likely witnessed phenomena involving a layer of liquid (e.g. polymer, oil, aqueous solution, etc.) coming into contact with a solid surface (e.g. bottom of a container, frying pan, glass, etc.). A flat, uniform layer is achieved when enough of the liquid covers the surface. However, when only a limited amount of liquid is introduced, it is possible that the liquid does not uniformly cover the surface - it dewets. These two situations can be explained using a quantity called the capillary length given by

$\lambda_{cap} = \sqrt{\gamma/\rho g}$, where g is the acceleration due to gravity, γ is the surface energy of the liquid, and ρ is its density. Substituting in some common values shows that λ_{cap} is generally on the order of a few millimeters. For liquid thicknesses greater than λ_{cap}, gravitational forces dominate which stabilize the liquid. For thicknesses less than λ_{cap}, intermolecular forces dominate and are responsible for creating potential instabilities and dewetting of the liquid. If we now consider the parameters γ_s and γ_{sl} as the substrate surface energy (the substrate may not be completely dry or absent of adsorbed molecules[2]) and substrate/liquid interfacial energy, respectively, then at final equilibrium a dewetted droplet of the liquid must obey the Young equation given by

$$\cos\theta_e = \frac{\gamma_s - \gamma_{sl}}{\gamma}, \tag{2.1}$$

where θ_e is the equilibrium contact angle that the droplet makes with the substrate surface. The condition $\gamma_s - \gamma_{sl} \geq \gamma$ corresponds to the $\theta_e = 0°$ case where the liquid completely wets the surface. Partial wetting occurs for $0° < \theta_e < 180°$ and non-wetting for $\theta_e = 180°$. However, in order to predict the dewetting process accurately, one must consider the full Helmholtz free energy curve of the liquid given as a function of its thickness.[3] By doing so, both long and short-range interactions are taken into account, which are equally crucial for determining the dewetting behavior for a thin liquid film with a thickness in the range of tens to hundreds of nanometers. For a much thicker film, the free energy can simply be given by $\gamma_{sl} + \gamma$. The strong influence of film thickness on the dewetting process is demonstrated in Figure 2.1 with a poly(4-bromostyrene) (PBrS) film on top of a substrate consisting of a stable poly(4-vinyl pyridine) (P4VP) layer on silicon. With increasing PBrS thickness, the behavior transitions from a stable structure to spinodal dewetting

PBrS (13 nm)
P4VP (30 nm)

PBrS (26 nm)
P4VP (30 nm)

PBrS (6.5 nm)
P4VP (30 nm)

PBrS (17 nm)
P4VP (30 nm)

Scan Area:
50 μm x 50 μm
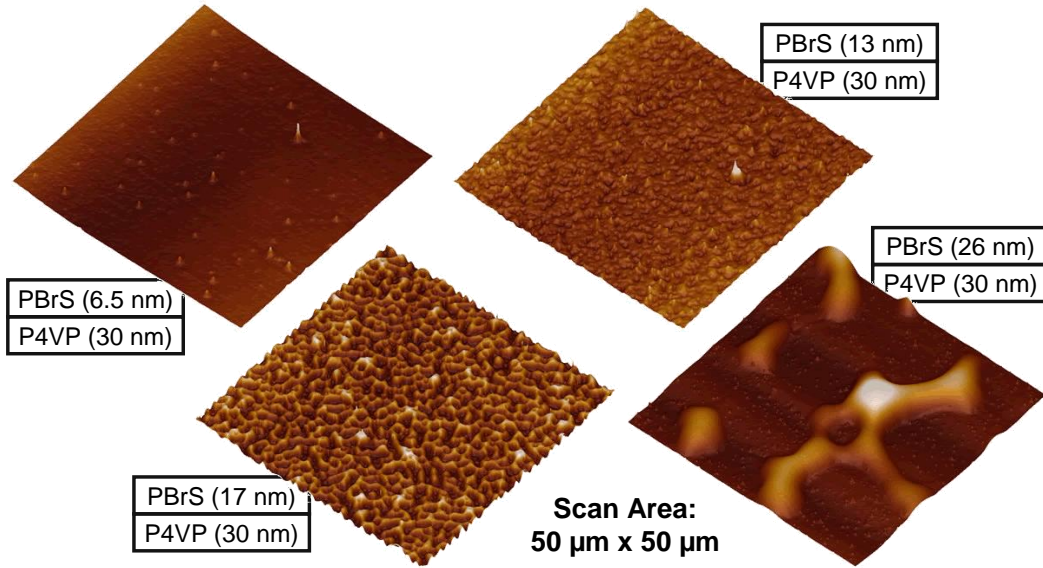
Figure 2.1. AFM topography images showing various dewetting patterns for PBrS/P4VP on silicon after annealing at 170 °C. The PBrS thickness is varied while the P4VP thickness is fixed. The behavior transitions from a stable structure to spinodal dewetting to dewetting by nucleation and growth with increasing PBrS thickness.

and finally to dewetting by nucleation and growth. A more quantitative treatment of this concept is presented in Chapter 3.

Tools for observing and analyzing dewetting in polymer thin films are well established. Obviously, imaging methods such as optical microscopy and atomic force microscopy (AFM) offer the most direct means for probing dewetting on the surface of a sample. The latter provides the capability to generate a one-dimensional profile of a dewetted droplet or a hole, permitting measurements such as the contact angle. *In situ*, real-time optical and AFM measurements to follow a dewetting event, which usually involves the continuous monitoring of the growth of individual holes and the subsequent coalescence of droplets, can also be performed. In the past, such studies have elucidated the kinetics

of the dewetting process and helped quantify its relationship with the film thickness and other physical parameters.[4–11] There are, however, limitations to this approach. First of all, the features being probed must reach a certain size and contrast to be observable, which is problematic for probing the very early stages of dewetting. Moreover, only the top surface of the sample can be probed, thus any dewetting in the interior of the sample is overlooked. Finally, the very local area examined by AFM does not supply sufficiently strong statistics and may not accurately reflect the behavior of the entire sample.[1,12–15] To overcome these difficulties, a class of techniques involving x-ray (or neutron) scattering can be employed. Reflectivity provides accurate measurements of the film thickness and roughness, while off-specular scattering can furnish information related to lateral density fluctuations at both the surface and buried interfaces of a sample over macroscopically large areas.[16–21] Most importantly, the subtle early signs of instabilities and dewetting can be detected with sensitivity to a specific interface.[22–24] The involvement of other complementary techniques, such as ellipsometry and time-of-flight secondary ion mass spectroscopy (ToF-SIMS) (which involves chemical composition mapping and depth profiling), can ultimately generate a complete picture of the dewetting process in polymer thin films. In Chapter 3, the system introduced in Figure 2.1 is investigated with a host of experimental techniques, enabling a comprehensive analysis of its thermodynamic stability and dewetting characteristics.

2.2. Self-Assembly and Phase Behavior in Block Copolymer Thin Films

Block copolymers have been known for a long time as promising candidates for providing self-assembled nanostructures relevant for a variety of novel technologies and applications. Dubbed by some as an unconventional lithographic technique,[25] the microphase separation of block copolymers in the thin film geometry can result in periodic, highly ordered nanopatterns with length scales on the order of tens of nanometers. A large amount of experimental and theoretical work have been undertaken to explore the diverse range of morphologies that block copolymers can generate based on their chemical composition and response to an ever-expanding number of processing strategies.[25–29] The system examined in Chapter 4 is an AB diblock copolymer consisting of two chemically distinct polymer blocks (A and B) covalently linked to each other. The following background discussion offers a brief overview of the behavior and properties of diblocks.

An AB diblock copolymer melt usually exhibits microphase separation due to the immiscibility or incompatibility of the two blocks. This behavior is best understood from an energy point of view.[25,31,32] The free energy of mixing ΔF_{mix} can be represented by the Flory-Huggins equation[33] which is written as

$$\frac{\Delta F_{mix}}{k_B T} = \frac{\phi_A \ln \phi_A}{N_A} + \frac{\phi_B \ln \phi_B}{N_B} + \chi \phi_A \phi_B, \tag{2.2}$$

where k_B is the Boltzmann constant, T is the temperature, χ is the Flory-Huggins interaction parameter, ϕ_A and ϕ_B are the volume fractions of the A and B blocks, and N_A and N_B are the degrees of polymerization of the A and B blocks. Here, the first two terms describe the entropy of mixing, which is always negative (favorable for mixing) and ideally independent of temperature. However, due to the large molecular weight of polymers, the
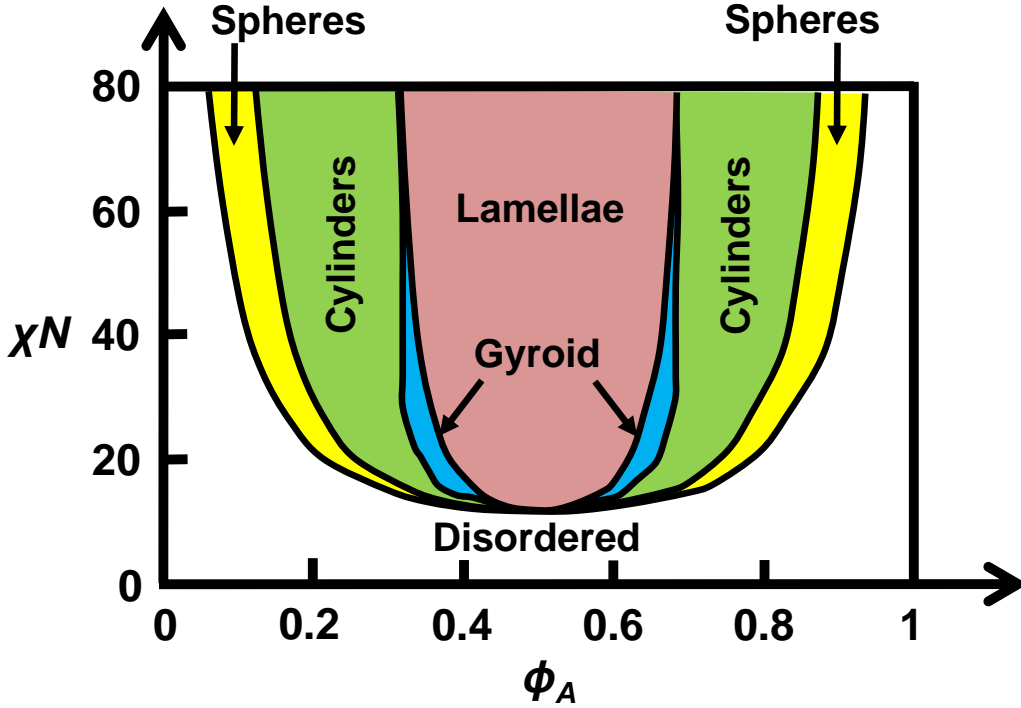
Figure 2.2. Phase diagram for an AB diblock copolymer showing χN given as a function of ϕ_A, the volume fraction of block A. Here, χ is the Flory-Huggins interaction parameter and N is the degree of polymerization of the diblock. Possible equilibrium structures include spheres, cylinders, gyroid, lamellae, and a disordered morphology.[30]

magnitude of the entropic contribution to ΔF_{mix} is usually very small. The last term in equation 2.2 describes the enthalpy of mixing, which is usually positive (unfavorable for mixing) and decreases with increasing temperature. Its contribution to ΔF_{mix} is much more significant, therefore causing ΔF_{mix} to take on a positive value in many cases. The ultimate effect is a microphase-separated structure that minimizes the unfavorable interactions between the blocks but avoids overstretching of the polymer chains. Figure 2.2 shows a typical phase diagram for a diblock copolymer, depicting χN given as a function of ϕ_A (N is the degree of polymerization of the diblock).[30] When the A and B blocks

possess approximately the same lengths, an alternating lamellar structure is achieved at equilibrium. However, when one of the blocks is considerably longer than the other, their interface begins to curve in order to maintain roughly equal stretching of the blocks. Consequently, the equilibrium structure can adopt that of a gyroid or turn into a collection of cylinders or spheres of the shorter block embedded in the matrix of the longer block. During preparation or processing of a diblock copolymer film, it is possible that additional components, such as a small-molecule solvent, are involved. In such a case, the phase diagram in Figure 2.2 can change, with certain phases becoming more accessible than others. The use of a selective solvent, for example, can greatly facilitate the formation of spherical micelles. Thus, with a host of variables involved in determining the equilibrium morphology of a diblock film, numerical simulations involving self-consistent field theory (SCFT) may be needed to make accurate structural predictions of size and shape, which is based on minimization of the free energy.[34–37]

As alluded to in the last paragraph, an as-prepared diblock copolymer film is usually not in its final equilibrium morphology and requires further processing.[26,29] To provide enough mobility to the polymer chains, thermal annealing above the glass transition temperatures of the polymer blocks may be performed. Alternatively, exposure of the diblock film to the vapor of a volatile solvent can also plasticize the structure, though strictly speaking, due to the temporary presence of the solvent component during processing, the film comes close to but never reaches the full equilibrium for its melt state (as predicted in Figure 2.2). Fast removal of the solvent kinetically traps the non-equilibrium structure, though reasonably well-ordered microdomains can usually be obtained nonetheless. From an industrial standpoint, however, perfectly aligned microdomains over very large areas
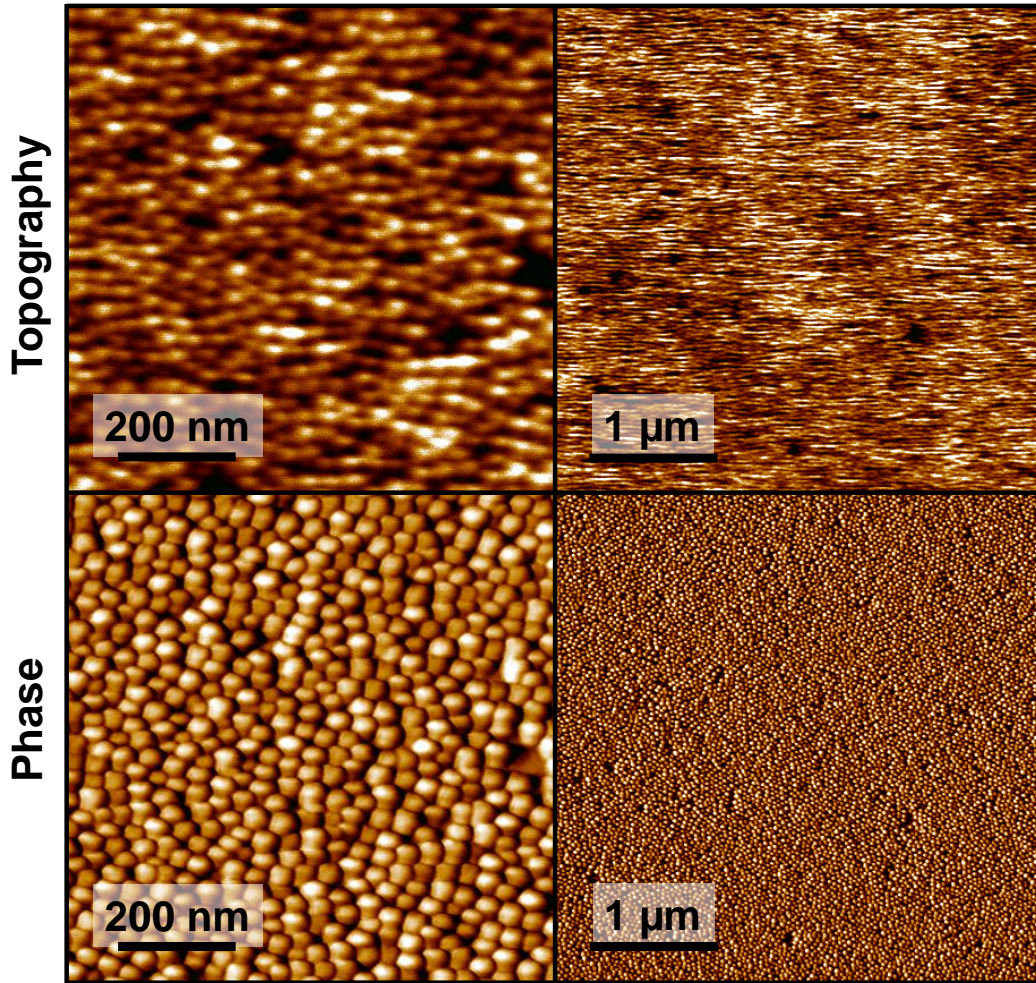
Figure 2.3. AFM topography and phase images of the surface of a PtBMA-PMMA (26.5k-17.9k) diblock copolymer film on silicon, as spun cast from a butanol solution without any further processing. The surface of this ∼30 nm-thick diblock film clearly consists of spherical micelles.

are required. Thus, it is sometimes necessary to manipulate the structure directly via external stimuli such as electric fields[38–40] or temperature gradients.[41] Moreover, the deposition of a diblock film onto a chemically patterned surface[42,43] or one with well-defined topographical features[44] can also be quite effective in guiding the ordering process. Finally, the proper control of surface and interfacial energies as well as the commensurability

of the film thickness relative to the period of the microdomain morphology can efficiently direct the orientation of the nanostructures inside a diblock film.[45,46]

A variety of imaging and scattering techniques can be employed to monitor the morphology adopted by a diblock copolymer thin film. Obviously, popular tools such as AFM are perfect for directly collecting a picture of a surface packed with micelles or one that consists of elegantly formed lamellar structures that are tens of nanometers in size. Figure 2.3, for instance, shows the topography and phase images of a poly(*tert*-butyl methacrylate)-poly(methyl methacrylate) (P*t*BMA-PMMA) diblock copolymer thin film as captured by AFM, revealing that the entire surface is covered with spherical micelles. However, the interior of the sample cannot be accessed with this technique and must be probed using x-ray (or neutron) scattering. Grazing-incidence small-angle x-ray scattering (GISAXS) is a powerful method that permits accurate lateral measurements of the spacing between microdomains with sensitivity toward various depths of the film. *In situ*, real-time measurements of the film structure during processing are especially useful for kinetic studies. Chapter 4 presents a comprehensive investigation of a P*t*BMA-PMMA diblock copolymer film that employs both GISAXS and AFM with focus placed on how processing directly affects the ordering of nanostructures in the film.

CHAPTER 3

Thickness-Dependent Autophobic Dewetting in Homopolymer Multilayer Films

Material in this chapter is reproduced in part with permission from "Thickness-Dependent Autophobic Dewetting of Thin Polymer Films on Coated Substrates," Y. Sun, K. R. Shull, D. A. Walko, and J. Wang; *Langmuir*, 27, 201-208 (2011). Copyright © 2010 American Chemical Society.

3.1. Introduction

In this chapter, we demonstrate that the wetting behavior of a thin liquid film, poly(4-bromostyrene) (PBrS), on top of a solid substrate may be effectively controlled with the insertion of a secondary liquid film, poly(4-vinyl pyridine) (P4VP), underneath the primary film. This secondary film remains stable under all conditions, and can be viewed as an extension of the substrate itself. On the basis of results from x-ray standing waves generated via total external reflection from an x-ray mirror, time-of-flight secondary ion mass spectroscopy, optical microscopy, and atomic force microscopy, we construct the full Helmholtz free energy versus PBrS thickness curve using existing theories that account for both long- and short-range interactions. The form of the free energy curve, which contains an inflection point and an absolute minimum at a nonzero PBrS thickness, accurately reflects our observation that thick PBrS films undergo autophobic dewetting on top of the stable P4VP, while sufficiently thin PBrS films remain stable. The thickness of the

autophobic wetting layer is controlled by the range of the repulsive interaction between the film and the substrate and is found to be $\sim$4 nm for the PBrS/P4VP interface.

3.2. Background

The ability of a thin liquid film to wet and remain thermodynamically stable on top of a solid substrate is of fundamental importance in developing reliable coatings, adhesives, dielectrics, and other industrial products. On the other hand, the breakup of a liquid film can be useful for spontaneous patterning applications[47] and for measuring thermal properties of a material.[48] The relevance of this subject spans across many disciplines with numerous key studies[6,49–55] having been conducted over the past few decades.[13,31,56–59] On the basis of its interaction with the substrate and the surrounding medium, a liquid film can wet or spontaneously dewet the substrate, with the latter case having the potential to produce a rich array of morphological features that are contingent on a number of physical parameters (e.g. film thickness) and processing conditions. Sharma *et al.* demonstrated that the evolutionary pathway and type of dewetting pattern established during the breakup of a liquid film are a direct consequence of the form of the Helmholtz free energy, F, while the characteristic length scales of the pattern are determined by the absolute magnitude of the second derivative of F.[60,61] Thus, by properly manipulating the form and magnitude of the free energy curve, one should be able to control the wetting behavior of a liquid film and its relationship to the film thickness in a predictable manner.

In general, the Helmholtz free energy contains contributions from both long- and short-range interactions, with effects from the long-range component easily extending across distances of 100 nm or more as discussed by Reiter *et al.*[62] Inflection points on the
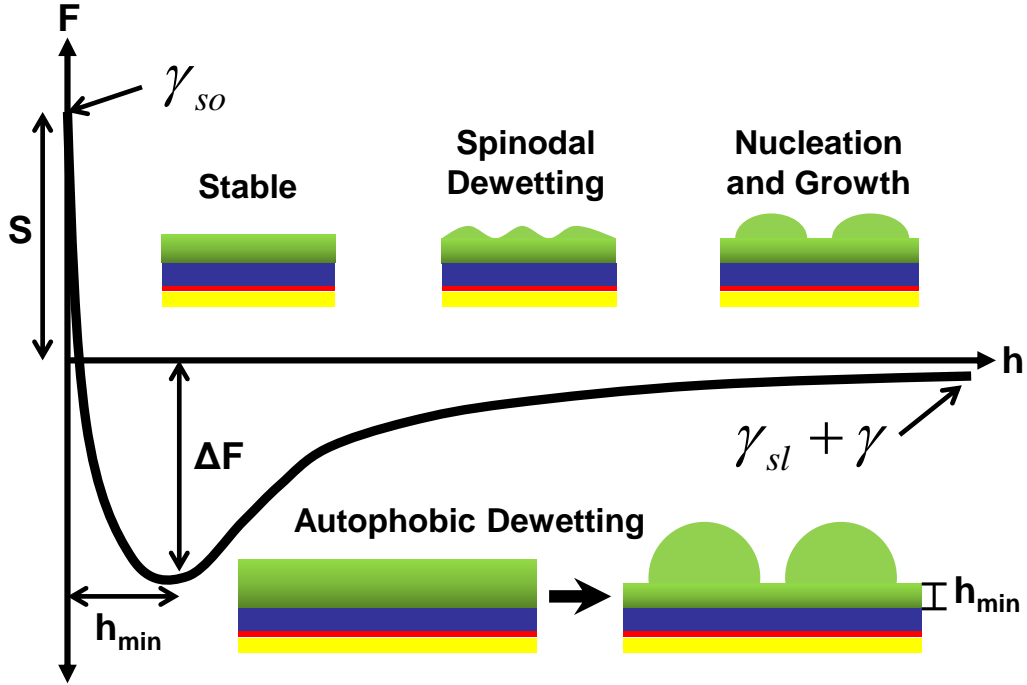
Figure 3.1. Qualitative sketch of the Helmholtz free energy per unit area of a film as a function of film thickness for the case of autophobic dewetting. Also depicted are illustrations of a film on a multilayer substrate undergoing autophobic dewetting and the dewetting behavior typically expected in various thickness regimes as a result of an inflection point on the curve.

free energy versus film thickness (F versus h) curve are particularly important in that they separate stable and metastable regions of positive curvature from unstable regions of negative curvature. Figure 3.1 depicts such an example, which is based on a continuum picture formulated by Brochard-Wyart *et al.*[3] For a single film on a thick, uniform substrate, the shape of the free energy curve is specified by the sign and magnitude of two independent parameters: the Hamaker constant, A, determined by long-range interactions, and the spreading parameter, S, determined by both short- and long-range interactions. For sufficiently large thicknesses, long-range van der Waals forces dominate,

with the shape of F following the general behavior of $A/12\pi h^2$ and asymptotically approaching $\gamma_{sl} + \gamma$, the sum of the substrate/film interfacial energy and the film surface energy. At the limit of zero film thickness, F is equal to γ_{so}, the surface energy of a completely dry substrate surface (which may be different from γ_s as discussed in Chapter 2).[2] The difference between $F(h = 0)$ and $F(h = \infty)$ is the spreading parameter S defined as $\gamma_{so} - \gamma_{sl} - \gamma$. In the case of a multilayer film or substrate, additional long-range terms containing distinct Hamaker constants corresponding to the contributions from each layer must be taken into account. In any scenario, when the free energy curve exhibits an absolute minimum at some nonzero thickness h_{min} as presented in Figure 3.1, autophobic dewetting is observed. Physically, this corresponds to the tendency for an initially uniform film of thickness greater than h_{min} to separate laterally into regions of different thicknesses. A common tangent construction between $F(h = h_{min})$ and $F(h = \infty)$ indicates that, at final equilibrium, macroscopic droplets of the film material tend to sit on top of a uniform wetting layer of itself with thickness h_{min} and an interfacial energy of ΔF, the depth of the minimum in the free energy curve.[2]

More complex behavior is observed when the single liquid layer is replaced by multiple liquid layers. In the simplest case of a bilayer on a solid substrate, it has been experimentally[22,63–65] and theoretically[57,66–70] shown that such a system possesses much richer behavior compared with the single layer case. For example, de Silva *et al.* demonstrated that either of the layers in a particular bilayer system could become unstable, depending on the thickness ratio between the two layers.[65] This observation illustrates the important point that the thickness of any single layer cannot completely determine its wetting behavior. In the case where the lower liquid layer always remains stable, this layer can

be viewed as an extension of the substrate. It still plays an important role, however, in that the Helmholtz free energy curve for the upper liquid film depends on both the film itself and on the substrate on which it rests. The use of these coated substrates is thus a particularly convenient way to control this free energy curve. Müller-Buschbaum *et al.* provided a glimpse of the usefulness of this method with such a system,[71] and we extend this approach in this investigation. On the basis of our experiments, we focus on constructing and monitoring the full free energy curve for a liquid film on a coated substrate, taking into account both long- and short-range interactions.[59] By systematically varying the thicknesses of the upper film and the substrate coating in our measurements, we explicitly quantify the changes in the free energy curve of the upper film and its resulting dewetting behavior.

Our substrate coating in this study comprises a poly(4-vinyl pyridine) (P4VP) film spun cast directly onto a smooth, solid substrate. The upper film for which the free energy versus thickness curve applies is poly(4-bromostyrene) (PBrS). For convenience, we shall refer to this system as PBrS/P4VP. The films are prepared on silicon substrates with a thin native oxide layer for all experiments except the x-ray studies, in which case palladium is used. We characterize the dewetting behavior of the PBrS film after thermal annealing using x-ray standing waves generated via total external reflection from an x-ray mirror (TER-XSW), time-of-flight secondary ion mass spectroscopy (ToF-SIMS), optical microscopy, and atomic force microscopy (AFM). Specifically, we reveal using the first two methods that the presence of the lower P4VP layer causes the upper PBrS layer to undergo autophobic dewetting (as opposed to complete dewetting) by transforming into droplets in equilibrium with a thin residual wetting layer of itself. We then use optical
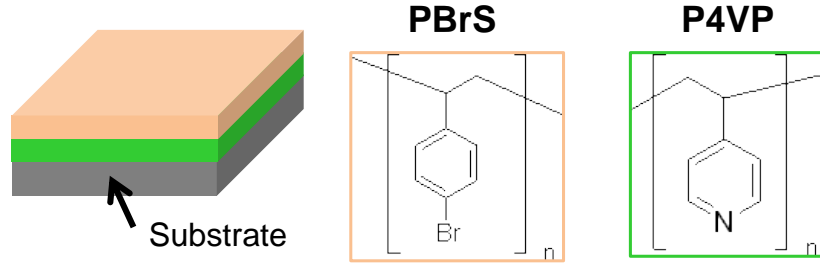
Figure 3.2. Chemical structures of poly(4-bromostyrene) (PBrS) and poly(4-vinyl pyridine) (P4VP). The PBrS/P4VP sample geometry for this study is also shown.

microscopy to image the dewetting patterns of the surface for different combinations of PBrS and P4VP thicknesses. From the optical micrographs, we obtain measurements of the in-plane characteristic wavelength due to spinodal dewetting, allowing us to determine values for the Hamaker constants describing the long-range contribution to the free energy. To estimate the short-range contribution to the free energy, we complement the analysis with AFM contact angle measurements of the dewetted PBrS droplets to determine ΔF, permitting us to sketch a set of plausible full free energy versus PBrS thickness curves for different P4VP thicknesses. Our results indicate that the PBrS characteristic spinodal dewetting length scale increases with increasing PBrS thickness as expected but decreases with increasing P4VP thickness. We subsequently demonstrate that the empirical Hamaker constants used in fitting the data are similar in sign and magnitude to those derived from calculations using refractive indices and dielectric constants given by the Lifshitz method. Moreover, we show that the measured PBrS contact angle increases with increasing P4VP thickness, which is quantitatively reflected in the depth of the minimum on the free energy curves.

3.3. Experimental Details

3.3.1. Materials

The two polymers for this study were acquired from Polymer Source Inc. with the following specifications and used as received: Poly(4-vinyl pyridine) (P4VP) (M_n = 130 kg/mol; M_w/M_n = 1.24) and poly(4-bromostyrene) (PBrS) (M_n = 11.7 kg/mol; M_w/M_n = 1.11). The P4VP was dissolved in 1-butanol to make solutions of 0.5, 1, and 1.5 wt %, which corresponded to approximate film thicknesses of 19.1, 32.7, and 53.0 nm when spun cast at 3000 rpm for 30 seconds onto a substrate. The as-cast thicknesses were measured with ellipsometry (M-2000D, J. A. Woollam Co., Inc.). The PBrS was dissolved in toluene to make solutions ranging from 0.1 to 2 wt %, resulting in film thicknesses that ranged from 3 to 36 nm. All spun-cast films were confirmed through our techniques to be initially flat and free from dewetting.

Samples for optical microscopy, AFM, and ToF-SIMS were prepared on cut pieces of 1-mm-thick silicon wafers (Silicon Quest International) with a thin native oxide layer ($\sim$1 to 2 nm) and rinsed with deionized water, acetone, and methanol before being subjected to ultraviolet/ozone cleaning (UVO Cleaner Model 42, Jelight Co.) for 20 minutes. Samples for the TER-XSW measurements were prepared on x-ray mirrors consisting of cut float glass pieces that had been successively coated with thin layers of Cr (5 nm) and Pd (50 nm), with the Cr serving as a binder between the Pd and glass. The deposition was carried out by the Optics Fabrication and Metrology (OFM) Group at the Advanced Photon Source at Argonne National Laboratory. The use of palladium, which gives rise to a large

critical angle, provides a much broader total external reflection region for generating x-ray standing waves than silicon. P4VP was found to be completely stable after extensive thermal annealing on both silicon and palladium, which was consistent with previous studies.[72] Using a spin coater from Headway Research, Inc. (Model 1-EC101-CB15), a layer of P4VP was first spun cast from butanol onto the substrate. Afterward, a PBrS layer was spun cast directly onto this P4VP layer from toluene, which is a nonsolvent for P4VP, producing our PBrS/P4VP sample.

To test the stability of the system against dewetting, all samples were subjected to thermal annealing treatments well above the glass transition temperatures of the polymers for up to 96 hours (4 days) in a standard laboratory vacuum oven. In most cases, an annealing temperature of 170 °C was used, as it was assumed that the glass transition temperatures of both the P4VP and PBrS are around 140 °C according to literature.[73–75] Due to the large differences in molecular weight, the viscosities for P4VP and PBrS in the bulk were estimated to be on the order of 10^8 and 10^6 Pa s, respectively, at the annealing temperature of 170 °C.[76] As mentioned before, dewetting in our experiment was restricted to the PBrS layer. After annealing, selective dissolution of the dewetted PBrS layer using toluene revealed that the P4VP surface remained very flat, with an rms roughness of ∼1 to 2 nm.

3.3.2. Methods

Four experimental techniques were employed in this work to understand the stability of the PBrS/P4VP system. Long period TER-XSW and ToF-SIMS were first used to determine that the dewetting of PBrS from P4VP is autophobic. In particular, to confirm that

the samples with the thinnest PBrS remained completely stable after annealing, TER-XSW provided a highly sensitive way to monitor slight changes to the interfaces over macroscopically large areas. For samples with thicker PBrS that clearly became unstable, two-dimensional maps of the chemical composition of the dewetted surface, as well as that of the interior (accomplished by sputtering), were generated with ToF-SIMS. We then used optical microscopy to image directly the surface of the annealed samples as a function of PBrS and P4VP thicknesses. Fast Fourier transforms were subsequently performed on these images to extract in-plane characteristic dewetting length scales. Finally, AFM complemented these results with measurements of the shape and height of the dewetted droplets in order to obtain values for the contact angle.

The AFM measurements were conducted in non-contact mode in air at room temperature using a high-resolution scanning probe microscope (JEOL JSPM-5200). A standard silicon probe of pyramidal shape, a tip radius of less than 10 nm, and a tip height of 14 to 16 μm was used (ACTA, Applied NanoStructures, Inc.). The optical microscopy images were taken using a Spot RT Digital Camera attached to a Nikon Epiphot inverted microscope at a 20× magnification. Fast Fourier transforms of the optical micrographs were performed using the *ImageJ* program.

The ToF-SIMS technique involves bombarding the sample surface with a beam of primary ions (typically liquid metal ions), resulting in the emission of secondary elemental or cluster ions from the surface. These secondary ions, which have different masses, are then electrostatically accelerated into a field-free drift region having a nominal kinetic energy of $eV_0 = mv^2/2$, where V_0 is the accelerating voltage, e the ion charge, m the mass of each ion, and v the flight velocity of each ion. Consequently, lighter ions have higher

velocities and reach the detector earlier, whereas heavier ions reach the detector later. This difference allows the chemical composition of the ions to be deciphered with great accuracy. The ToF-SIMS measurements were conducted with a Physical Electronics PHI TRIFT III, which utilizes a pulsed Ga^+ liquid ion gun operated at 25 keV with charge compensation and a typical beam size of 120 nm in diameter. This setting is generally optimized for mapping chemical species from near the surface ($\sim$0.5 to 1 nm) with high sensitivity ($\sim$1 ppm) and high mass resolution ($m/\Delta m \sim$9000). For our samples, we chose to map an area of $100 \times 100 \ \mu m^2$, where each analyzed point within this area monitored and stored an entire mass spectrum of intensities. This procedure allowed us to create intensity maps of specific ions (or regions of interest on the mass spectrum) from the analyzed area. The 256×256 pixel images translated to a resolution of approximately 390 nm per pixel. In the negative ion mode, we focused on the Br^- ($m/z = 79$) and CN^- ($m/z = 26$) peaks, which originated exclusively from PBrS and P4VP, respectively. Data were acquired for 20 minutes to collect adequate counts and develop enough contrast in the intensity maps. Line scans of the maps were subsequently performed to reveal differences in composition between the dewetted droplets and flat regions.

The TER-XSW technique has been demonstrated to be a highly sensitive structural probe suitable for analyzing thin multilayer films with length scales on the order of tens to hundreds of angstroms.[77–80] An x-ray standing wave is generated when there is interference between the incident and reflected x-ray plane waves, which only occurs when there is total external reflection (TER) from the x-ray mirror (see Figure 5.1). The TER condition is found between the incident angles of $\theta = 0$ and the critical angle of the mirror $\theta = \theta_c$ ($\sim$4.35 mrad in our case with Pd), with the period D of the standing wave decreasing

from $D = \infty$ to the critical period given by $D_c = \lambda/2 \sin \theta_c$ ($\sim$95.1 Å in our case with Pd) with increasing angle, where λ is the x-ray wavelength. As formulated by Bedzyk *et al.*,[77] by applying Fresnel theory and considering the complex electric field amplitude ratio of the reflected and incident waves, the normalized electric field intensity I as a function of incident angle θ and distance above the mirror surface z is given by

$$I(\theta, z) = \frac{|E_0 + E_R|^2}{|E_0|^2} = 1 + R + 2\sqrt{R} \cos(\nu - Qz), \tag{3.1}$$

where E_0 and E_R describe the incident and reflected electric field plane waves, R is the reflectivity, ν is the relative phase shift of the reflected plane wave, and Q is the magnitude of the scattering vector pointing in the z direction given by $Q = 4\pi \sin\theta/\lambda$. The presence of a thin, high-Z marker layer (PBrS in our case) positioned at some distance larger than D_c above the mirror surface leads to an oscillatory behavior in the marker (Br) fluorescence signal with increasing angle due to planes of high and low electric field intensities effectively moving past this layer. This provides a direct way to infer the location and distribution of the markers with subnanometer resolution. To this end, the normalized fluorescence yield Y from an arbitrary, one-dimensional distribution $\rho(z)$ of heavy atom markers above the mirror surface of distance z as a function of incident angle θ is expressed by

$$Y(\theta) = \int_{z=0}^{z=\infty} I(\theta, z) \rho(z) \, dz. \tag{3.2}$$

The ability to model the distribution $\rho(z)$ of heavy markers accurately from the electric field intensity I, which can be related to the reflectivity data, and Y, which can be related to the fluorescence data, forms the essence of the TER-XSW technique.

The TER-XSW measurements were performed with synchrotron radiation on the 7-ID and 33-BM beamlines at the Advanced Photon Source at Argonne National Laboratory. An x-ray energy of 15 keV ($\lambda = 0.827$ Å), located above the bromine K-edge of 13.47 keV, was used to generate Br Kα fluorescence coming from PBrS. A typical, narrow beam of approximately 1 mm wide and 0.06 mm high in the z direction was employed.[80] A NaI(Tl) scintillation detector (Oxford Cyberstar X1000) was used for collecting reflectivity data as a function of incident angle, while a Vortex-EX single-element silicon drift detector situated next to the sample, perpendicular to the beam direction, simultaneously captured the fluorescence data (see Figure 5.2). The electric field intensity and the reflectivity were calculated using Parratt's recursion formulation[81] with the data of the latter fit using χ^2-minimization (Levenberg-Marquardt method). For samples with a relatively thin PBrS layer (e.g. 3 nm), the fluorescence yield Y was calculated with $\rho(z)$ assumed as a skewed, normalized Gaussian distribution given by

$$\rho\left(z\right) = \left\{ \begin{array}{ll} \frac{1}{\sqrt{2\pi}\sigma} \exp\left(-\frac{(z-z_{cen})^2}{2[\sigma(1+s)]^2}\right) & z \geq z_{cen} \\[3mm] \frac{1}{\sqrt{2\pi}\sigma} \exp\left(-\frac{(z-z_{cen})^2}{2[\sigma(1-s)]^2}\right) & z < z_{cen} \end{array} \right\}. \tag{3.3}$$

The Gaussian width σ, the center of distribution z_{cen}, and the skew parameter s were adjusted to fit Y to the fluorescence data using χ^2-minimization. For samples with a thicker PBrS layer (e.g. 13 nm), a flat region h representing bulk PBrS had to be added to the center of this model in order to fit the data. After normalization, the expression

for this case was given by

$$\rho\left(z\right) = \begin{cases} \frac{1-2rh}{\sqrt{2\pi}\sigma} \exp\left(-\frac{(z-z_{cen}-r)^2}{2[\sigma(1+s)]^2}\right) & z \geq (z_{cen}+r) \\ \\ \frac{1-2rh}{\sqrt{2\pi}\sigma} \exp\left(-\frac{(z-z_{cen}+r)^2}{2[\sigma(1-s)]^2}\right) & z \leq (z_{cen}-r) \\ \\ h = \frac{1}{\sqrt{2\pi}\sigma+2r} & (z_{cen}-r) < z < (z_{cen}+r) \end{cases}. \tag{3.4}$$

The skew parameter served as an important degree of freedom to account for the fact that the PBrS marker layer was bounded on either side by unidentical media (P4VP and air), allowing the stability and roughnesses of the PBrS/P4VP and PBrS/air interfaces to be decoupled from each other.

3.4. Results and Discussion

3.4.1. Characterization of the Autophobic Wetting Layer

Determining whether an autophobic wetting layer exists as PBrS dewets upon thermal annealing is essential for understanding how the P4VP layer modifies the free energy curve of the PBrS and properly relating the measured dewetting contact angles with interfacial energies. Furthermore, autophobic dewetting behavior generally implies that sufficiently thin PBrS films are thermodynamically stable due to the required local minimum and positive concavity in the Helmholtz free energy curve. With these conditions in mind, the goal for the TER-XSW measurements was to confirm that samples with the thinnest PBrS (in the autophobic/stable regime) remained completely stable after annealing, while
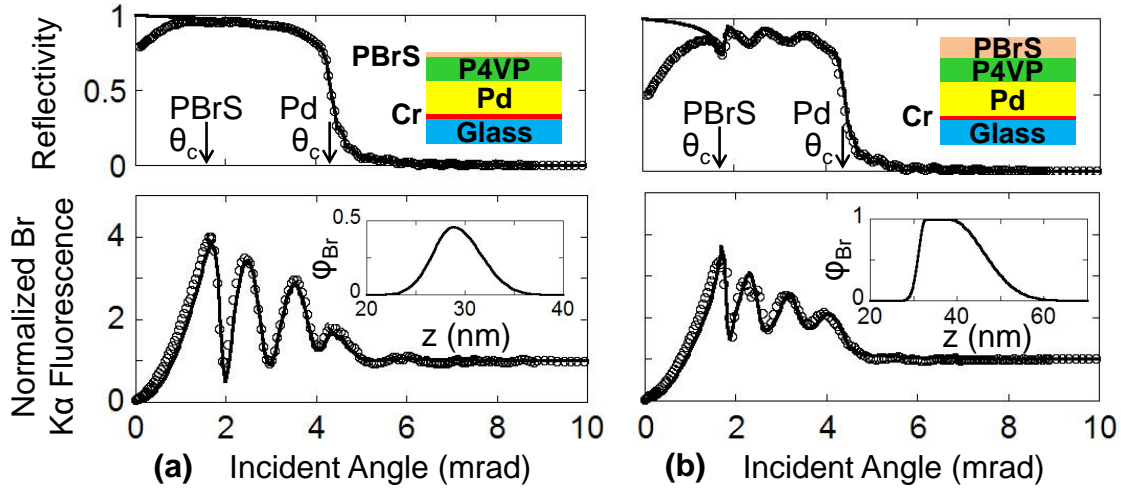
Figure 3.3. X-ray reflectivity and normalized bromine Kα fluorescence profiles for the PBrS/P4VP system prepared on top of an x-ray mirror comprising Pd, Cr, and glass (shown in schematic) and annealed at 160 °C for 10 hours. The thickness of the P4VP is 30 nm. The thicknesses of the PBrS are (a) 3 nm and (b) 13 nm. The solid lines are fits to the experimental data points with the predicted bromine distributions (volume fractions) φ_{Br} shown in the insets.

the aim in the ToF-SIMS measurements was to observe directly in samples with thicker PBrS (in the spinodal regime) that a thin residual wetting layer of PBrS was left behind upon dewetting.

Our PBrS/P4VP samples prepared on top of palladium mirrors for TER-XSW were restricted to PBrS thicknesses of no more than ~13 nm because the technique becomes insensitive to small interfacial fluctuations when the thickness of the marker layer is much larger than the XSW period, which in our case was as small as 9.5 nm. However, this was enough to distinguish the behavior between a relatively thin sample (3 nm PBrS as cast) that remained completely stable and a slightly thicker one (13 nm PBrS as cast) that started to destabilize. Figure 3.3 shows the TER-XSW data for these two cases after

10 hours of thermal annealing at 160 °C, which was sufficient to see this difference. The as-cast thickness of the P4VP layer in both samples was 30 nm, yielding at least three full oscillations in the Br Kα fluorescence curve so that good fits to the data could be obtained. The predicted bromine marker distributions from fitting the reflectivity and Br Kα fluorescence, expressed in terms of the volume fractions φ_{Br} of PBrS, are shown in the insets. Taking into account the Gaussian width and the skew of the distribution, we can easily estimate the roughnesses of the PBrS/air and PBrS/P4VP interfaces. For a PBrS thickness of 3 nm, they are determined to be 2.8 and 2.1 nm, respectively. For 13 nm, these values are 7.0 and 2.1 nm, respectively, with the distribution clearly skewing to the right. These results suggest that, while the PBrS/P4VP interface remained fairly stable (at its intrinsic roughness) after annealing in both cases, the PBrS/air interface in the 13 nm PBrS sample became comparatively larger after annealing, possibly due to the development of instabilities. For the 3 nm PBrS sample, no changes were seen between the 10-hour data and those obtained after just a few minutes of annealing (not shown) even with the high spatial sensitivity of TER-XSW. This result confirms that, over macroscopically large areas, the PBrS for small thicknesses remains as a very stable layer on top of the P4VP but dewets for larger thicknesses, suggesting that the free energy curve must contain an inflection point with positive and negative concavities at small and large thicknesses, respectively.

To deduce whether a minimum at a nonzero thickness exists in the free energy curve, we directly probed via ToF-SIMS the in-plane distribution of PBrS and P4VP on the surface and in the interior of PBrS/P4VP samples with thicker PBrS layers, which fell into the spinodal regime of the free energy curve. Shown in Figure 3.4 are two-dimensional
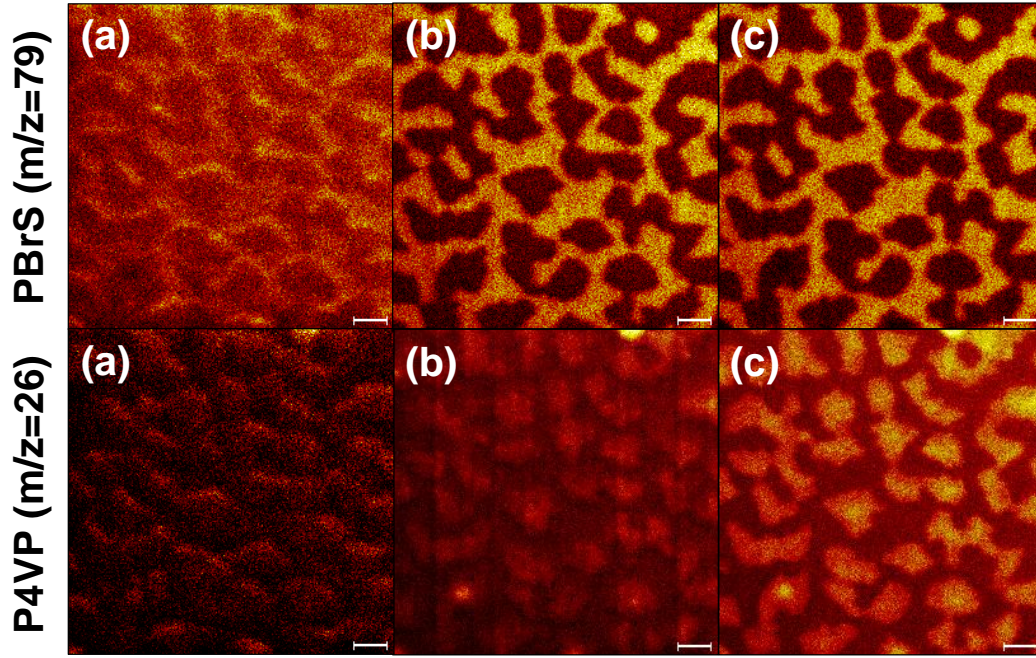
Figure 3.4. ToF-SIMS intensity maps of the PBrS/P4VP system after annealing at 170 °C for 96 hours. The P4VP layer is 30 nm thick, while the PBrS layer is 27.6 nm thick. Shown are maps for PBrS (Br$^-$ peak; $m/z = 79$) and P4VP (CN$^-$ peak; $m/z = 26$) after 20 minutes of collection time. Presented here is the sample surface (a) without any sputtering, (b) after 30 seconds of sputtering, and (c) after 120 seconds of sputtering. The scale bars are 10 μm.

ToF-SIMS intensity maps for a representative sample (PBrS thickness 27.6 nm and P4VP thickness 30 nm as cast) that had been annealed at 170 °C for 96 hours. This combination of PBrS and P4VP thicknesses produced dewetting features large enough to accommodate the resolution of the maps and yielded more Br$^-$ and CN$^-$ counts than thinner samples in the same amount of collection time. For a relative comparison of the intensities, corresponding horizontal line scans across the maps are shown in Figure 3.5. The immediate surface, as depicted in Figure 3.4a without any sputtering, shows that it is covered almost entirely with PBrS with little evidence of P4VP. After sputtering uniformly for 30 and 120
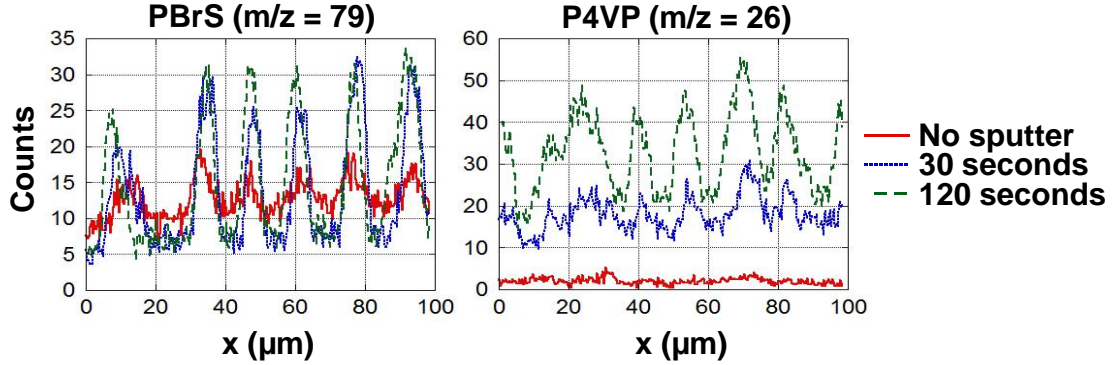
Figure 3.5. Horizontal line scans of the ToF-SIMS intensity maps from Figure 3.4. Shown are the absolute counts from PBrS (Br$^-$ peak; $m/z = 79$) and P4VP (CN$^-$ peak; $m/z = 26$) after 20 minutes of collection time.

seconds, we see in Figures 3.4b-c that the PBrS in specific locations, which correspond to the flat regions and valleys between dewetted droplets, have more or less been sputtered away, leaving behind PBrS only on the droplets and ridges. At the same time, P4VP becomes progressively more noticeable in the flat regions and valleys. This is also evident in Figure 3.5, which shows that after sputtering the P4VP signal is the strongest where the PBrS signal is the weakest, and vice versa. This result clearly points to the presence of a thin PBrS wetting layer which is in equilibrium with thick dewetted PBrS droplets.

3.4.2. Spinodal Dewetting and Curvature of the Free Energy Function

Since PBrS autophobically dewets P4VP, the shape of the Helmholtz free energy versus PBrS thickness curve should contain similar features to the one shown in Figure 3.1. In order to construct a specific free energy curve for our system, we begin by considering an experimentally measurable parameter that is directly related to the strength of the long-range forces, the in-plane characteristic spinodal dewetting wavelength λ, which is a dominant rupture length scale corresponding to the fastest growing unstable mode of
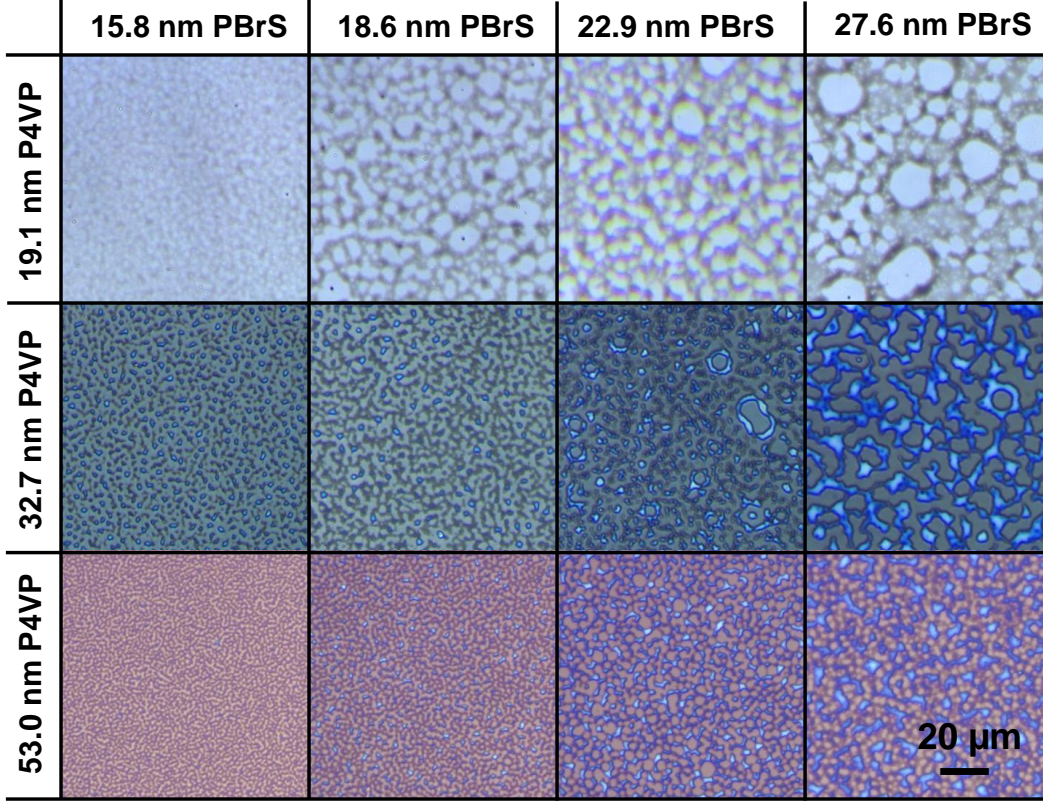
Figure 3.6. Optical micrographs of the PBrS/P4VP system on silicon, for different combinations of PBrS and P4VP thicknesses as shown, after annealing at 170 °C for 96 hours.

thickness fluctuations. It has been shown that this quantity can be related to the free energy via the relationship

$$\lambda\left(h\right) = \sqrt{-\frac{8\pi^2\gamma}{F''\left(h\right)}}, \tag{3.5}$$

where F'' is the second derivative of the free energy, γ the surface energy of PBrS, and h its thickness.[49,50] Thus, we can in practice obtain experimental data points for the second derivative of the free energy curve, which can then be used to generate the long-range portion of the free energy curve itself.

To measure the parameter λ in equation 3.5, we used optical microscopy to image the dewetted surface of a series of samples comprising different combinations of PBrS and P4VP thicknesses that have been annealed at 170 °C for up to 96 hours. λ is then defined as the inverse of the peak position acquired from a Fourier transform of the optical images and subsequent radial integration.[1,10,82] Figure 3.6 shows the surfaces of selected samples possessing spinodal dewetting patterns after 96 hours of annealing. Patterns taken after 24 hours (not shown) and 96 hours, even for the thinnest films, exhibited almost identical dewetting length scales, confirming our assumption that these experiments correspond to the early stages of spinodal dewetting, where the use of equation 3.5 is appropriate. From observation across each row in Figure 3.6, it is apparent that there exists a trend of increasing PBrS dewetting length scale with increasing PBrS thickness. From observation down each column, it can be seen that the PBrS dewetting length scale decreases with increasing P4VP thickness. Samples with PBrS thicker than 27.6 nm (not shown) apparently required much longer annealing time to rupture due to the weaker driving force, but these samples already exhibited many uncorrelated holes due to nucleation and growth before spinodal dewetting was able to appear. Patterns reminiscent of spinodal dewetting were seen in PBrS thicknesses as thin as 10.0 nm. Regardless of the P4VP thickness, samples with PBrS thicknesses of ∼6 nm and smaller optically did not seem to exhibit any signs of dewetting. As a further check, these samples were also probed with AFM to obtain finer and higher-resolution scans of the surface (not shown), which, in agreement with the TER-XSW measurements, did not demonstrate any appreciable topographical variations reminiscent of dewetting. In this light, we estimate that the transition from stable to unstable regimes should occur between the PBrS thicknesses of 6 and 10 nm
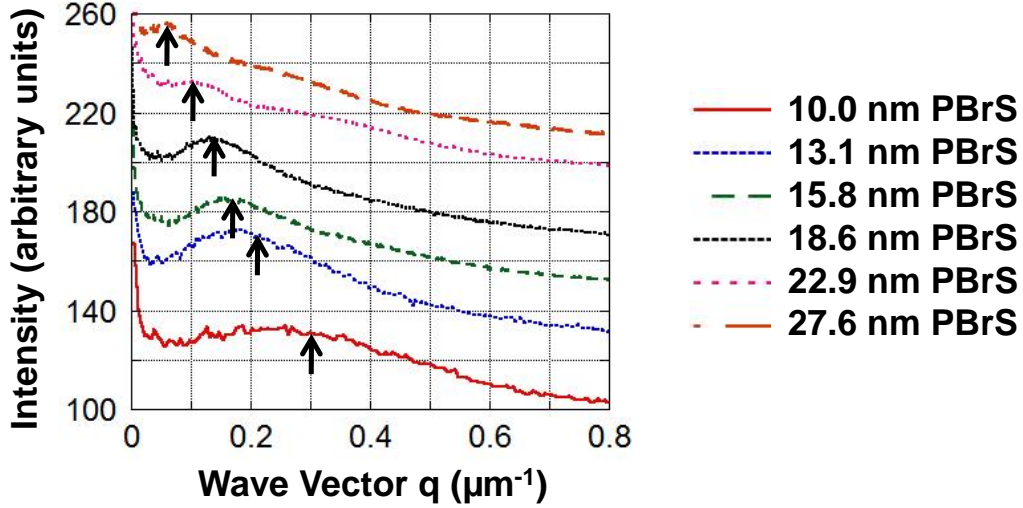
Figure 3.7. Results of fast Fourier transforms after radial integration of optical micrographs of the surface of dewetted PBrS/P4VP samples. Shown is the data set for a fixed P4VP thickness of 32.7 nm. The arrows point to local maxima, which we regard as the characteristic spinodal dewetting wavelengths. The curves have been shifted vertically for clarity.

for the three P4VP thicknesses studied. We must note, however, that, for the case where the P4VP layer is absent (0 nm P4VP), completely different behavior in the PBrS was observed: Regardless of PBrS thickness, all samples dewetted upon annealing via nucleation and growth from defects or dust particles within the films on much faster time scales compared to the samples with the P4VP layer.

Next, we performed fast Fourier transforms on the optical micrographs with spinodal dewetting patterns to obtain quantitative values for λ. As an example, Figure 3.7 presents the results of fast Fourier transforms (after performing radial integration) for a series of samples with a fixed P4VP thickness of 32.7 nm. In each of these curves, we readily pick up a peak position in q by fitting a quadratic function over the vicinity of the peak and obtaining a local maximum (indicated by the arrows). The inverse of these peak positions,
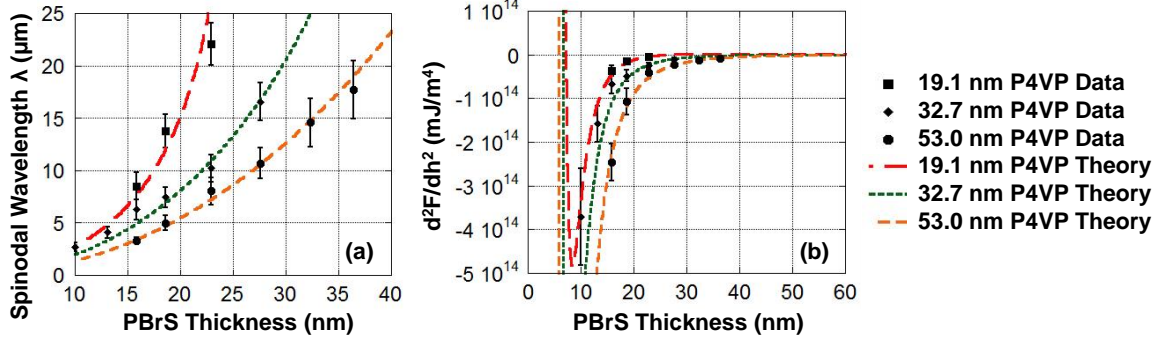
Figure 3.8. (a) Plots of the in-plane characteristic spinodal dewetting wavelength λ versus PBrS thickness, as extracted from the peaks in the fast Fourier transforms in Figure 3.7, for three different P4VP thicknesses. The lines are theoretically calculated based on the free energy curves in Figure 3.9. (b) Plots of the second derivative of the Helmholtz free energy versus PBrS thickness, obtained via equation 3.5, for three different P4VP thicknesses. The lines are theoretically calculated based on equation 3.6 using the parameters in Table 3.1.

which we regard as the characteristic spinodal dewetting wavelengths, are plotted against the PBrS thickness and are presented in Figure 3.8a along with data sets from the two other P4VP thicknesses (19.1 and 53.0 nm).

To use the data in Figure 3.8a in constructing a free energy curve, we follow the general procedure that was carried out by Seemann $et\ al.$,[1,10,82] taking into account both long- and short-range contributions to the free energy. To develop the long-range portion of the curve, we relate the measured spinodal wavelength λ to the second derivative of the free energy F'' using equation 3.5. Assuming a literature value of $\gamma = 33.7\ mJ/m^2$ for PBrS,[73,74] we convert the λ versus h data to that of F'' versus h, which are shown in Figure 3.8b. Next, we write a general expression for F to use in our analysis. We consider, for the long-range part, a five-layer model comprising the components air/PBrS/P4VP/SiOx/Si (SiOx is silicon oxide), where we sum the van der Waals contributions from each of the

layers. Following the assumption of Seemann *et al.*, for the short-range part, we assume that factors such as chemical interactions and steric repulsion between two planar surfaces follow a $1/h^8$ dependence, so that for the total free energy we have

$$F\left(h\right) = \frac{c}{h^8} - \frac{A_{P4VP}}{12\pi h^2} + \frac{A_{P4VP} - A_{SiOx}}{12\pi(h + d_{P4VP})^2} + \frac{A_{SiOx} - A_{Si}}{12\pi(h + d_{SiOx} + d_{P4VP})^2}, \qquad (3.6)$$

where A_{P4VP} is the Hamaker constant of the air/PBrS/P4VP system, A_{SiOx} of the air/PBrS/SiOx system, A_{Si} of the air/PBrS/Si system, and c is a parameter characterizing the strength of the short-range interactions. Here, d_{P4VP} and d_{SiOx} are the thicknesses of P4VP and silicon oxide layers, respectively. A fixed value of 2 nm (estimated with ellipsometric measurements) is assumed for d_{SiOx}, which, we note, has a noticeable effect on the calculations, especially for the 19.1 nm P4VP data set. Therefore, we choose not to neglect the SiOx layer from our analysis. After finding the second derivative of equation 3.6, we fit the parameters A_{P4VP}, A_{SiOx}, and A_{Si} in the resulting expression to the F'' versus h data in Figure 3.8b, obtaining empirical values which are given in Table 3.1. We note from the results that a single value for A_{SiOx} and A_{Si} can satisfactorily be used for all three P4VP thickness cases, while A_{P4VP} needs to be varied in order to fit the data. These values for the Hamaker constants can be compared with those obtained from utilizing refractive indices and dielectric constants given by the Lifshitz method. We refer to the chapter on van der Waals forces between surfaces in the book of Israelachvili for the complete formula.[83] Table 3.1 lists the estimated values for A_{P4VP}, A_{SiOx}, and A_{Si} determined using the Lifshitz method, with the refractive indices acquired from ellipsometric measurements (PBrS ∼1.6-1.7; P4VP ∼1.55). Considering the inevitable small variations in experimental conditions and sample architecture which sometimes can dramatically

Table 3.1. Empirical Values for the Helmholtz Free Energy Parameters in Equation 3.6.

Data Set	c (Jm^6)	A_{P4VP} (J)	A_{SiOx} (J)	A_{Si} (J)
0 nm P4VP	$\sim 10^{-76}$ (*)	–	1.2×10^{-19}	-2.7×10^{-19}
19.1 nm P4VP	8.0×10^{-72}	2.7×10^{-20}	1.2×10^{-19}	-2.7×10^{-19}
32.7 nm P4VP	8.0×10^{-72}	4.6×10^{-20}	1.2×10^{-19}	-2.7×10^{-19}
53.0 nm P4VP	8.0×10^{-72}	9.0×10^{-20}	1.2×10^{-19}	-2.7×10^{-19}
Lifshitz Theory	–	$\sim 1 \times 10^{-19}$	$\sim 1 \times 10^{-19}$	$\sim -2 \times 10^{-19}$

(*) This value for c was assumed and based on previous experiments.[1,10,82]

affect the results, the values of our Hamaker constants determined using these two independent methods are reasonably consistent with each other. The value of the short-range parameter c in Table 3.1 is determined using AFM measurements of the PBrS contact angle and its relationship to ΔF, the depth of the free energy minimum (explained in detail in the next section), which is directly affected by the magnitude of c. The full (long- and short-range) theoretical curves of F'' versus h simulated using Table 3.1 are shown as lines in Figure 3.8b, and the predicted dependences of λ on h converted using equation 3.5 are shown as lines in Figure 3.8a.

Figure 3.9 presents the full theoretical curves of the Helmholtz free energy versus PBrS thickness simulated using equation 3.6 and the parameters in Table 3.1 for the three P4VP thickness cases studied. Performing a straightforward calculation of the locations of the absolute minimum ($F' = 0$) and inflection point ($F'' = 0$), for the 19.1 nm P4VP curve, we obtain respective values of 6.08 and 7.20 nm for h_{min} and the PBrS thickness at which the system transitions from stable to unstable. For the 32.7 nm P4VP curve, they are 5.47 and 6.55 nm, and for the 53.0 nm P4VP curve, they are 4.88 and 5.85 nm. These values are all consistent with our optical and AFM observations. Also shown in Figure
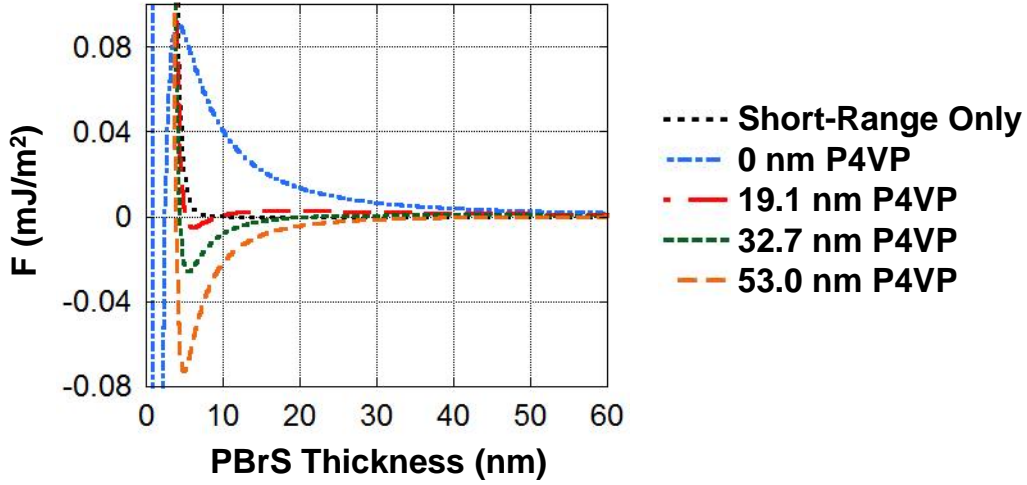
Figure 3.9. Theoretical curves of the Helmholtz free energy per unit area versus PBrS thickness for three different P4VP thicknesses, calculated using equation 3.6 and the parameters in Table 3.1, which are based on results from the optical microscopy images and AFM contact angle measurements. Also shown are the theoretical curves for the case where the P4VP layer is absent (0 nm P4VP) and of the short-range contribution only (with P4VP present).

3.9 is the case where the P4VP layer is absent (0 nm P4VP), calculated using the same A_{SiOx} and A_{Si} values but a different c value due to the now direct interaction of PBrS with the silicon substrate. Here, a potential barrier exists and positive concavity for all PBrS thicknesses greater than ~4 nm (in the metastable regime) implies that dewetting of the PBrS can only occur by nucleation and growth.

3.4.3. Determination of the Free Energy Minimum and the Role of Short-Range Interactions

The short-range parameter c in equation 3.6 has been used in the past to describe short-range interactions in thin liquid films[1,10] and is used here largely because of this historical

precedent. We do not have enough information from our experiments to rule out alternative forms of this potential that might also be appropriate.[54,60,62] The important point here is that some short-range repulsion must exist in our system, and the c parameter provides a useful way of describing these interactions in phenomenological terms and comparing to previous results. Our procedure is to adjust this parameter until ΔF, the depth of the minimum in the free energy curve, matches the experimentally measured values from the contact angle measurements. A larger value of c reduces ΔF and shifts the position of the minimum to larger h_{min}. The $1/h^8$ dependence can clearly not persist to extremely low thicknesses, since $F(h = 0)$ must equal the spreading parameter. This spreading parameter is almost certainly positive, since the surface energy of P4VP $(50\ mJ/m^2)$[75] is much larger than that of PBrS $(33.7\ mJ/m^2)$.[73,74] The equilibrium contact angle θ_e in our samples is that between dewetted PBrS droplets and its autophobic wetting layer, which is related to the free energy minimum by $\Delta F \approx \gamma\theta_e^2/2$ assuming that θ_e is small.[2] We measured θ_e from AFM scans of annealed PBrS/P4VP samples (170 °C for 96 hours) in the glassy state, which means that we must take into account a volume contraction of $\sim$7 to 8% of the droplets due to quenching of the samples from 170 °C to room temperature.[84] Figure 3.10 shows an example of one such droplet profile, where the height H and radius R are used to calculate θ_e according to the relationship $\tan(\theta_e/2) = H/R$ (the correction due to volume contraction is assumed to be restricted to the height direction). In Figure 3.10, for a P4VP thickness of 32.7 nm and PBrS thickness of 27.6 nm, we obtain an equilibrium contact angle of $\theta_e = 2.2° \pm 0.2°$ (after averaging over at least twenty such measurements), which corresponds to a free energy minimum depth of $\Delta F = 0.025\pm0.005$ mJ/m^2. For a P4VP thickness of 53.0 nm and PBrS thickness of 27.6 nm (not shown), we
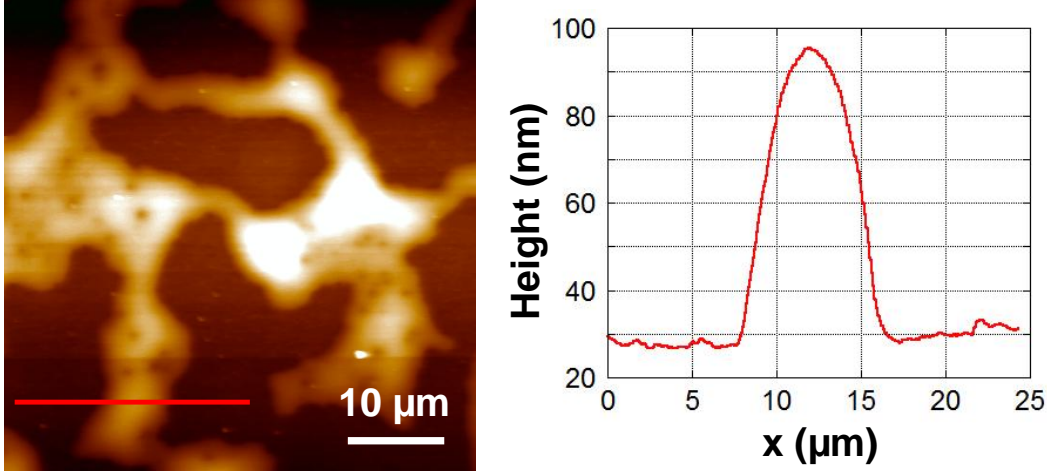
Figure 3.10. AFM topography image and line scan of the surface of a PBrS/P4VP sample on silicon after annealing at 170 °C for 96 hours. The thickness of the P4VP is 32.7 nm, and the thickness of the PBrS is 27.6 nm.

obtain an equilibrium contact angle of $\theta_e = 3.6° \pm 0.3°$ and a free energy minimum depth of $\Delta F = 0.067 \pm 0.011 \ mJ/m^2$. We did not obtain satisfactory results for a sample with a P4VP thickness of 19.1 nm due to large discrepancies in the measurement of the very small PBrS contact angle in this case. Nevertheless, it turns out that a single value for the parameter c listed in Table 3.1 seems to be sufficient to complete the free energy curves at small PBrS thicknesses (excluding the 0 nm P4VP case) in Figure 3.9. This value is given such that the resulting ΔF's in the plots are consistent with the experimentally determined ΔF values from AFM.

The magnitude of c, which dictates the strength of the short-range interactions, can be related directly to the range of the short-range repulsive potential. If we define a characteristic thickness h_0 as the value of h that gives an interaction potential of F_0, we have

$$h_0 = (c/F_0)^{1/8}. \tag{3.7}$$

From Figure 3.9, we see that the magnitude of the interaction potential in the thickness range of interest is ~ 0.1 mJ/m^2. Using this value for F_0, with $c = 8.0 \times 10^{-72}$ Jm^6, gives $h_0 \approx 4$ nm. By comparison with the results of Seemann *et al.*[1,10,82] for poly(styrene) on a silicon substrate covered with an oxide layer, where $c \approx 10^{-76}$ Jm^6, the short-range interaction is found to persist up to distances of ~ 1 nm. The existence of a short-range repulsion out to the unexpectedly large distance of 4 nm in the PBrS/P4VP system is one of the important conclusions of this work.

3.5. Conclusions

We demonstrated in this chapter that the form and magnitude of the Helmholtz free energy curve of a thin liquid film may be tuned in order to control the films stability and thickness-dependent wetting behavior. Here, we explicitly observed and quantified changes to the behavior of a PBrS film on a solid substrate with the insertion of a P4VP film between the PBrS and the substrate. By systematically varying the thicknesses of both the PBrS and P4VP films, we produced the full free energy versus PBrS thickness curves for different P4VP thicknesses. Our conclusions can be summarized as follows: The Hamaker constants (associated with the long-range interactions) determined from the characteristic dewetting wavelength in the spinodal regime are consistent with those obtained from a calculation using the optical properties of the different layers in the system. We find the necessary existence of a short-range potential describing the interaction between the P4VP substrate and the PBrS film. This potential has a range of around 4 nm and determines the thickness of the autophobic layer.

CHAPTER 4

Effects of Reactive Annealing on the Structure in Amphiphilic Diblock Copolymer Thin Films

Material in this chapter appears in the paper "Effects of Reactive Annealing on the Structure of Poly(methacrylic acid)-Poly(methyl methacrylate) Diblock Copolymer Thin Films," Y. Sun, K. J. Henderson, Z. Jiang, J. W. Strzalka, J. Wang, and K. R. Shull; *Macromolecules*, submitted.

4.1. Introduction

In this chapter, we monitor the structural evolution of a poly(*tert*-butyl methacrylate)-poly(methyl methacrylate) (P*t*BMA-PMMA) diblock copolymer thin film undergoing conversion via reactive annealing to yield poly(methacrylic acid)-poly(methyl methacrylate) (PMAA-PMMA). Using grazing-incidence small-angle x-ray scattering (GISAXS) and atomic force microscopy (AFM), we confirm the generation of well-ordered cylindrical micelles in the P*t*BMA-PMMA precursor film after solvent annealing. After initiating thermal deprotection, the high degree of ordering can be maintained up to 25% conversion of the diblock into PMAA-PMMA. Beyond this point, a significant decrease in the overall film thickness associated with the conversion process cannot accommodate the hexagonal lattice adopted by the cylindrical micelles. At the same time, rearrangement of PMMA cores in a P*t*BMA matrix that is becoming progressively glassier presents further difficulties in maintaining a reasonable structure. The fully converted PMAA-PMMA

film contains a system of disordered cylindrical micelles and other microdomains that lack good ordering.

4.2. Background

Block copolymer thin films have been well exploited for their generation of highly ordered nanostructures, which are necessary for a myriad of nanopatterning and lithographic applications. The self-assembly process is governed by a combination of thermodynamic and kinetic contributions, posing a variety of challenges from a fabrication and processing standpoint. The morphologies adopted by a block copolymer film are dependent on a host of adjustable parameters, including the chemical composition and relative lengths of the blocks, interaction strength between the blocks, film thickness, substrate chemistry and patterning, and surface and interfacial energies.[26,85–88] In addition, effects from extra components involved in processing a film, such as a small-molecule solvent, often need to be taken into account.[89,90] A final complication, which is the focus of this chapter, concerns the *in situ* modification of the chemistry of the block copolymer itself, where its composition evolves with time during processing.[91]

The block copolymer of interest in this study is a diblock copolymer consisting of a hydrophobic block connected to a second block that can undergo conversion from a hydrophobic polymer to a hydrophilic one during processing. Films of these resulting amphiphilic block copolymers are an attractive class of materials offering a foundation for numerous industrial and biomedical applications in aqueous environments. Their responsive behavior (toward pH or ions) and reactive functionalities (i.e. COOH) provide the opportunity for developing sophisticated filtration technology and vehicles for drug delivery.[92,93]

Direct preparation and processing of amphiphilic copolymer films such as poly(styrene)-poly(acrylic acid) (PS-PAA) to generate nanopatterns and ordered morphologies have traditionally been more challenging than the more versatile and manageable hydrophobic ones such as poly(styrene)-poly(methyl methacrylate) (PS-PMMA).[94–97] Due to the large solubility differences between the blocks of amphiphilic copolymers in water, organics, and a variety of other solvents, solvent casting usually results in films comprised of spherical micelles that are kinetically trapped and are extremely difficult to manipulate any further. PS-PAA is a diblock that has been thoroughly investigated in solution since the mid-1990s.[98] Due to the formation of reverse micelles in most organic solvents, PS-PAA was at first only studied in colloidal assemblies spun cast from toluene.[99] Consequently, the ester linkage in poly(*tert*-butyl acrylate) (P*t*BA) was advantageously employed in thin films of the non-amphiphilic PS-P*t*BA[100–103] to convert the P*t*BA block into PAA via thermal or acid-catalyzed deprotection.[104] This same procedure has also been used in an ABC-type triblock copolymer to generate water-swollen perforated lamellar structures composed of poly(styrene)-poly(vinyl pyridine)-poly(*tert*-butyl methacrylate) (PS-PVP-P*t*BMA).[105] Such an *in situ* conversion process has made copolymers such as PS-PAA more accessible in terms of available thin film morphologies and has contributed to their success in the generation of responsive surfaces,[101,102] cavitated nanoreactors,[99,106] and templates for forming inorganic nanostructures.[100,107,108]

The structural evolution of these block copolymer films during annealing where one of the blocks, P*t*BA or P*t*BMA, undergoes *in situ* conversion to PAA or poly(methacrylic acid) (PMAA), is a complex yet intriguing process where ordering and arrangement in the film can be directly dictated by alterations in the chemical identity and interactions

of the blocks, glass transition temperature, film density and thickness, and numerous other factors. In the study by La *et al.* involving fabrication methods for nanodots,[100] the conversion of PS-PtBA diblock films to PS-PAA via thermal deprotection was accompanied by a transition of well-ordered cylindrical micelles to spherical ones due to an inevitable change in the volume fraction of the converting block. Here, annealing was conducted well above the glass transition temperatures of both the PtBA ($T_g = 49$ °C)[109] and PAA ($T_g = 106$ °C)[110] so that the diblock always remained kinetically mobile for morphological arrangement throughout the conversion process. In the case of PtBMA ($T_g = 111$ °C)[111] converting to PMAA ($T_g = 228$ °C),[112] however, thermal annealing can only be conducted below ∼200 °C due to anhydride formation or depolymerization at higher temperatures.[112,113] Thus, kinetic trapping of micelles in a matrix that is becoming progressively glassier must be taken into account, complicating the processing scheme. In this chapter, we focus on monitoring the ability for a PtBMA-PMMA diblock film to provide ordered nanostructures during an *in situ* thermal deprotection process to yield PMAA-PMMA. We show that such a state may be attained with a considerable amount of PtBMA conversion, although once the system achieves full conversion, the structure is found to be kinetically frozen in a less ordered state. While, for practical purposes, acid-catalyzed deprotection could be a better alternative in this case,[104,114,115] the intent of this study is to demonstrate an important pitfall which may be encountered during such an *in situ* chemical modification procedure for block copolymer films similar to this one.
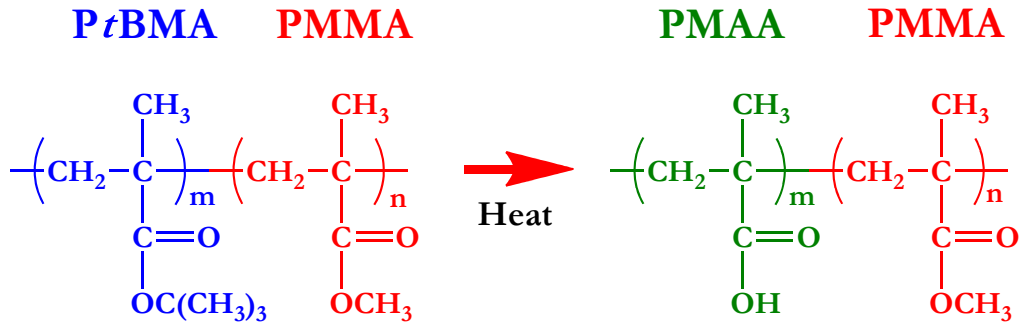
Figure 4.1. Chemical structures of the P*t*BMA-PMMA and PMAA-PMMA diblock copolymers. The *tert*-butyl functionality of P*t*BMA can be cleaved off to generate PMAA via thermal deprotection.

High Temperature Solution (80 °C)   **Swollen Spherical Micelles in Solution**   **Deswollen Spherical Micelles on Substrate**   **Cylindrical Micelles on Substrate**   **Converted, Frozen Structure**
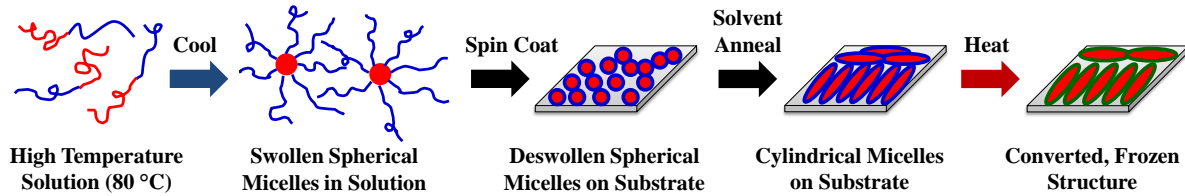
Figure 4.2. Illustration showing the complete annealing procedure undertaken in this study for generating nanostructures in a PMAA-PMMA film from a P*t*BMA-PMMA (22.5k-11.0k) precursor diblock. Red, blue, and green colors represent PMMA, P*t*BMA, and PMAA, respectively.

Thermal deprotection of the precursor P*t*BMA-PMMA diblock film to generate PMAA-PMMA involves cleaving off the *tert*-butyl functionality in P*t*BMA, as presented in Figure 4.1. An annealing temperature between 160 °C and 200 °C provides reasonable time scales for the conversion (hours to a few days) while preventing anhydride formation or depolymerization. The complete annealing procedure we have performed in this study is illustrated in Figure 4.2. After preparation of the precursor P*t*BMA-PMMA diblock in solution and subsequent spin coating to produce a micellar film, a major step in our processing scheme involves solvent annealing of the P*t*BMA-PMMA film prior to thermal

annealing in order to generate an array of well-ordered nanostructures, in this case cylinders, to be carried through the conversion process. Without this crucial step (that is, if thermal annealing were performed on the PtBMA-PMMA film directly after spin coating), the system of spun-cast spherical micelles would be too kinetically slow for major structural organization compared to the rate of conversion, freezing in the morphology too soon. Based on our knowledge, solvent annealing of a fully converted PMAA-PMMA film also presents difficulties due to the very limited selection of suitable volatile solvents that can mobilize both blocks.[92] Therefore, the solvent annealing step shown in Figure 4.2 is intended to provide the necessary head start for the system to release itself from the kinetically trapped as-prepared structure and move toward thermodynamic equilibrium. In this work, a combination of thermogravimetric analysis (TGA), atomic force microscopy (AFM), x-ray reflectivity, and grazing-incidence small-angle x-ray scattering (GISAXS) performed *in situ* reveals a complete picture of the effects that the thermal deprotection process has on the structural evolution of a PtBMA-containing diblock copolymer film.

4.3. Experimental Details

4.3.1. Materials

The precursor diblock copolymer poly(*tert*-butyl methacrylate)-poly(methyl methacrylate) (PtBMA-PMMA) was synthesized via anionic polymerization as given in a previous paper.[92] Using gel-permeation chromatography, we determined the molecular weights of the PtBMA and PMMA blocks to be 22.5 kg/mol and 11.0 kg/mol, respectively, with a polydispersity index of 1.07, resulting in a PMMA volume fraction of 0.3. The diblock was dissolved in 1-butanol at 80 °C to make solutions of up to 5 wt % and cooled through the

critical micelle temperature down to room temperature prior to spin coating. As a result, the alcohol solution consisted of swollen spherical micelles of the diblock with PMMA as the cores.[116,117]

Samples for AFM and the x-ray experiments were prepared on cut pieces of 1 mm-thick silicon wafers (Silicon Quest International) with a thin native oxide layer ($\sim$1 to 2 nm) and rinsed with deionized water, acetone, and methanol before being subjected to ultraviolet/ozone cleaning (UVO Cleaner Model 42, Jelight Co.) for 20 minutes. A spin coater from Headway Research, Inc. (Model 1-EC101-CB15) was used to deposit the diblock onto the silicon substrates. Spin coating from butanol at 3000 rpm for 30 seconds, we obtained film thicknesses from several tens of nanometers up to $\sim$150 nm (as measured with an ellipsometer, M-2000D, J.A. Woollam Co., Inc.) depending on the solution concentration. From our experimental data, the general behavior and structural evolution of our system did not depend crucially on the initial film thickness.

Two types of annealing treatments were carried out in this study. *Ex situ* solvent annealing was conducted at room temperature by placing the sample alongside a tetrahydrofuran (THF) solvent bath inside a well-sealed container to ensure the solvent vapor was able to plasticize the polymer film effectively. The vapor pressure of the THF was controlled by mixing with non-volatile 2-ethyl-1-hexanol (2EH) at a 90/10 molar ratio, yielding an approximate vapor pressure of 129 Torr at 20 °C. *Ex situ* thermal annealing was performed in a standard laboratory oven under vacuum at 160 °C and 180 °C. For the GISAXS measurements, both *in situ* thermal and solvent annealing utilized a sealed chamber with Kapton® polyimide windows penetrable by x-rays. Here, the temperature

of the sample was controlled by a Peltier heater as well as by a heated copper block positioned underneath the chamber. During this procedure, the interior of the chamber was placed under nitrogen to minimize beam damage to the polymer film.

4.3.2. Methods

Four experimental techniques were employed in this work to investigate the structural evolution of our diblock system. TGA was used to determine the temperature-dependent rate at which PtBMA-PMMA converted to PMAA-PMMA through the weight loss that occurred during heating. This information served as a guide for understanding our x-ray structural measurements during various stages of annealing. X-ray reflectivity provided measurements of the film thickness as well as electron density via the polymer critical angle. GISAXS patterns collected at various grazing incident angles over macroscopically large areas of the sample were used to monitor changes in the microdomain spacing and overall extent of the nanostructure ordering with high accuracy. Finally, AFM characterization provided a complementary real-space confirmation of the morphology on the sample surface.

Thermogravimetric analysis was performed using a Mettler Toledo Thermogravimetric Analyzer (model TGA/SDTA851^e) on bulk PtBMA-PMMA samples with initial weights of 3 to 5 mg in a nitrogen environment. The weight of the dry polymer powders was monitored over time as they were isothermally heated at 160 °C and 180 °C. AFM measurements were conducted in non-contact mode in air at room temperature using a high-resolution scanning probe microscope (JEOL JSPM-5200). We utilized a standard silicon probe of pyramidal shape, a tip radius of less than 10 nm, and a tip height of 14 to 16

μm (ACTA, Applied NanoStructures, Inc.). Both topography and phase images were captured, but only the phase images were able to reveal the boundaries and packing of the micelles with the necessary clarity.

Both GISAXS and x-ray reflectivity are well-known, powerful techniques capable of characterizing the nanostructure and thickness of thin films averaged over long distances.[14,15] The experiments were performed with synchrotron radiation on the 8-ID beamline at the Advanced Photon Source at Argonne National Laboratory. The standard configuration involved an x-ray energy of 7.35 keV ($\lambda = 1.69$ Å) and a beam size of 0.1 mm wide and 0.05 mm high before impinging on the sample. An avalanche photodiode detector was used for sample alignment and the reflectivity measurements, while a MAR165 CCD (or PILATUS 1M pixel array) detector captured the two-dimensional GISAXS patterns with a pixel size of 79 (or 172) μm. The distance between the sample and the area detector, which was calibrated with a silver behenate standard, was close to 2 m. A lead beam stop was also placed in front of the detector to block the intense specular beam. GISAXS patterns were collected at several incident angles, which determined the penetration depth of x-rays into the film and thus the region from which data was collected. We focused on obtaining patterns from right below and above the critical angle of the film, corresponding to information originating from the surface and interior of the film, respectively.[118] The GISAXS patterns were saved as 2048×2048 16-bit TIFF images (for the case of MAR165) and processed with a beamline MATLAB program (which took into account the sample-to-detector distance and detector resolution) to produce intensity maps in the q_y-q_z plane, where q_y is the scattering vector component parallel

to the sample surface and perpendicular to the scattering plane and q_z is the component perpendicular to the sample surface.

The thickness of the diblock films were extracted from fitting the reflectivity data according to Parratt's recursion formulation[81] via χ^2-minimization (Levenberg-Marquardt method). The microdomain spacing was obtained by taking line scans of GISAXS patterns in q_y at a fixed q_z and measuring the q_y position of the first-order peak using a Gaussian fit. For samples that exhibited higher-order peaks, the physical arrangement or packing geometry of the micelles was determined by matching the positions of the diffraction peaks on the GISAXS patterns to theoretically calculated positions from an assumed lattice structure. Our choice for this assumed structure was based on the AFM images and the arrangement of the empirical peaks in the q_y-q_z plane, which were expected to translate into a similar arrangement of micelles in real space. The simulated peak positions were calculated using the theory of the distorted-wave Born approximation (DWBA), as described in detail in previous papers.[118–122] Specifically, we followed the procedure of Stein *et al.* to generate an array of diffraction coordinates which we overlaid with our GISAXS patterns.[118] Changes in the corresponding lattice constants revealed the structural evolution of the diblocks in each annealing step. We describe this analysis in more detail in the next section.

4.4. Results and Discussion

4.4.1. Kinetics of the P*t*BMA-to-PMAA Conversion

Obtaining an accurate measurement of the rate at which P*t*BMA-PMMA converts to PMAA-PMMA via thermal deprotection is essential for analyzing and understanding the
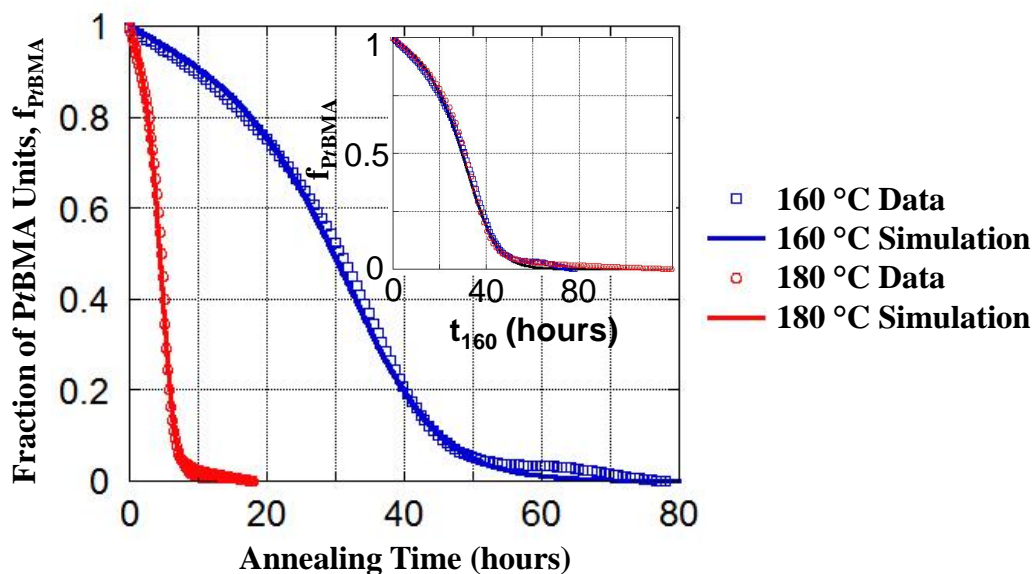
Figure 4.3. TGA data showing the fraction of unconverted PtBMA units versus annealing time for the PtBMA-PMMA diblock at 160 °C and 180 °C. The solid lines are simulated curves based on chemical kinetics calculations. The inset shows the master curve obtained from time-temperature superposition using a reference temperature of 160 °C.

observed structural changes in our films. In the next two subsections, we quantify precisely the conversion kinetics of the diblock, comparing the behavior in the bulk and in thin films. We confirm that the conversion behavior is identical in both cases, allowing us to consider bulk properties when analyzing the results for our thin films.

4.4.1.1. Reaction Kinetics in the Bulk Material. Measurement of the chemical conversion of a polymer in the bulk and in thin films can be readily performed with a variety of available approaches. Wallraff *et al.* have previously reported on the kinetics of the conversion for a PtBMA homopolymer in the range of 180 °C to 220 °C, though ignoring the effects of anhydride formation above 200 °C.[104] The results from these isothermal

heating experiments suggested a two-step process involving an induction period (slow conversion rate) followed by a gradual transition to an auto-accelerated mechanism (faster conversion rate) where converted PMAA facilitates the further production of PMAA from PtBMA. Accordingly, a reaction scheme given by 1) PtBMA $\rightarrow$ PMAA and 2) PtBMA + n PMAA $\rightarrow$ $(n + 1)$ PMAA was used in a stochastic simulation of chemical kinetics to determine the rate constants for this multistep reaction mechanism. In our study, we performed isothermal heating on our specific PtBMA-PMMA diblock using TGA. The weight of the bulk diblock was monitored as a function of time at 160 °C and 180 °C until it approached some constant value, indicating that conversion of the PtBMA block was complete. In both cases, a final weight loss of $\sim$28% was observed, which is reasonably close to the predicted value of 26.5% from simple stoichiometric calculations. The PMMA block was not altered by the heating. Figure 4.3 plots the fraction of PtBMA units remaining in the system as a function of annealing time. As can be directly observed, the conversion of the PtBMA block is initially slow but later speeds up, which is consistent with the mechanism proposed by Wallraff *et al.* A theoretical calculation with the same reaction scheme as above was performed using the *Chemical Kinetics Simulator* program from IBM Research-Almaden.[123,124] Input parameters included the rate constants for each reaction step, which comprise the activation energy E_a in addition to a pre-exponential factor. Here, the parameters from Wallraff *et al.* were used as a starting point and the simulated curves were carefully matched to our experimental data through fine adjustments of the values.[104] The best fit to our data gave $E_a = 40.9 \ kcal/mol$ for the first reaction and $E_a = 37.9 \ kcal/mol$ for the second reaction, with $n = 1.5$. The simulated curves for 160 °C and 180 °C are shown with the TGA data in Figure 4.3. As a

further step, the data at our two temperatures can be merged into a single master curve following the time-temperature superposition principle, using a reference temperature of 160 °C (433 K) in this case. The inset of Figure 4.3 plots the shifted TGA data with the horizontal time axis t_{160} defined as

$$t_{160} = \int_0^t \exp\left[-\frac{E_a}{R}\left(\frac{1}{T(t)} - \frac{1}{433K}\right)\right] dt, \tag{4.1}$$

where t is the original annealing time, T is the absolute temperature at which the TGA data is collected, E_a is the activation energy, and R is the universal gas constant. Through this method, we obtain for E_a a single value of 37.5 $kcal/mol$, which is quite close to the result obtained for the second reaction (auto-acceleration step) in the chemical kinetics simulation above. This master curve is utilized in the next subsection for comparing the bulk kinetics to the physical changes observable in our PtBMA-PMMA films during thermal annealing.

4.4.1.2. Reaction Kinetics in Thin Films. For our PtBMA-PMMA diblock films, the thermal deprotection process is expected to have a significant impact on the overall film thickness and electron density, which, in turn, can affect the ordering of nanostructures inside the films. The *tert*-butyl group on the PtBMA is removed during conversion to form PMAA, which has a higher known bulk density (1.29 g/cm^3) than PtBMA (1.02 g/cm^3). X-ray reflectivity was employed to obtain the film thickness and electron density for a variety of samples. Figure 4.4a presents two examples of reflectivity curves and their corresponding fits for a PtBMA-PMMA film as spun cast and thermally annealed for 72 hours at 160 °C, which is essentially a fully converted PMAA-PMMA film. The number of fringes is clearly reduced after the annealing process, which through fitting corresponds to
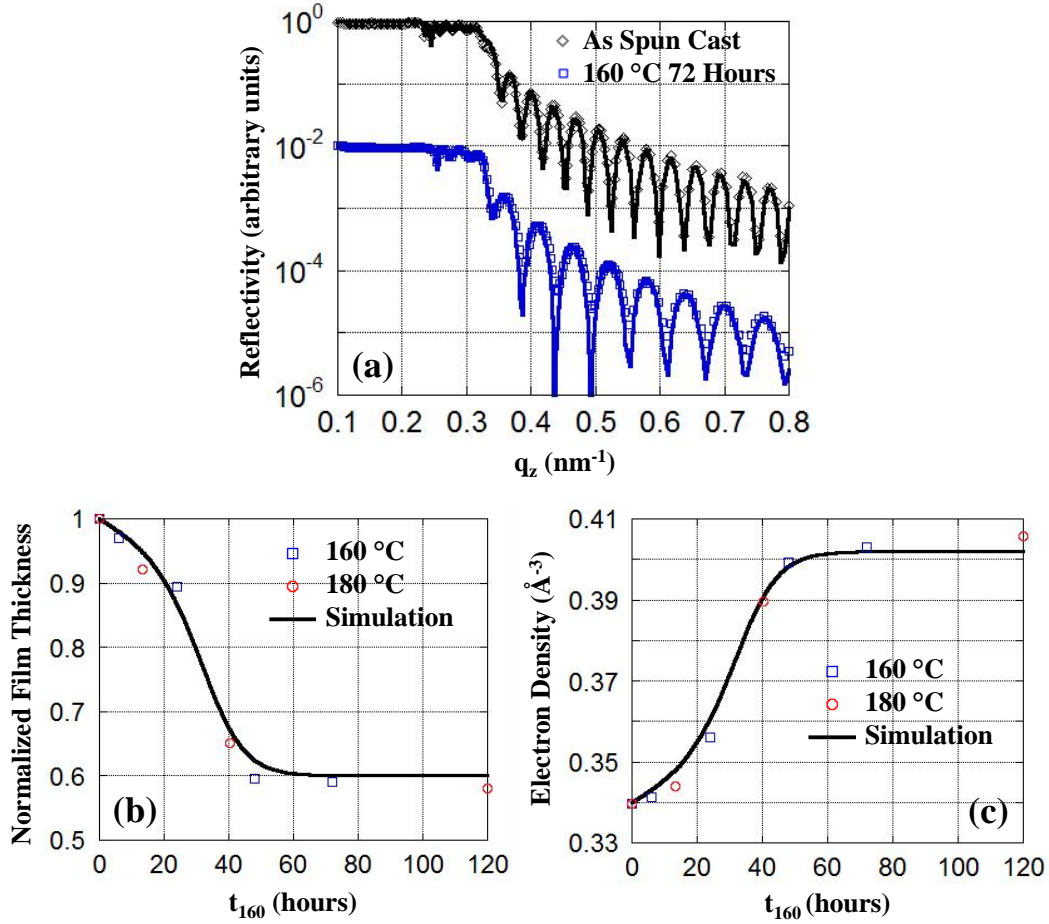
Figure 4.4. (a) Reflectivity data near $\theta_{c,film}$ for a PtBMA-PMMA film as spun cast and thermally annealed at 160 °C for 72 hours. The solid lines are fits to the data. The curves are shifted vertically for clarity. (b) Plot of normalized film thickness versus shifted annealing time t_{160}, which forms a master curve with a reference temperature of 160 °C. (c) Plot of electron density of the film versus shifted annealing time t_{160}. The solid lines in (b) and (c) correspond to kinetic predictions obtained from the TGA data of a bulk sample.

a thickness change from ∼154 nm to ∼96 nm, a decrease of roughly 38%. Measurements were also performed on films with other initial thicknesses (not shown), and we find that all of them generally undergo a decrease of 40% in thickness after full conversion, which

agrees reasonably well with stoichiometric predictions. We also collected the reflectivity at various time points during thermal annealing at 160 °C and 180 °C. Figure 4.4b plots the evolution in the film thickness, normalized by the initial thickness, as a function of the shifted annealing time t_{160}. Additionally, the master curve in Figure 4.3 obtained from TGA is rescaled and shown with the data. A remarkable agreement can be seen between the film thickness and conversion behavior, which confirms our expectations. The reflectivity curves also furnish information about the electron density of the film via measurement of the polymer critical angle $\theta_{c,film}$. Through fitting of our data, $\theta_{c,film}$ is seen to increase from ~0.17° to 0.18° (q_z ~0.22 to 0.24 nm^{-1}) during the course of the conversion, corresponding to an electron density increase from ~0.34 to 0.40 electrons/Å^3. These values translate into a density of ~1.04 g/cm^3 for the unconverted PtBMA-PMMA film and ~1.24 g/cm^3 for the fully converted PMAA-PMMA film, which match well with predictions obtained from a weighted average (using weight fractions) of the known bulk density values for the polymer blocks. Figure 4.4c plots the evolution in the electron density of the film as a function of t_{160}. Again, the TGA master curve in Figure 4.3 is shown with the data, yielding an excellent agreement. This similarity means that the kinetic parameters obtained from the thermogravimetric analysis of the bulk polymer samples can be used to quantify the conversion state of the thin films as well.

4.4.2. Structural Development During Processing

With an understanding of the kinetics of the thermal deprotection process, we now focus on monitoring the structural changes in our PtBMA-PMMA films during various stages of processing. In the next three subsections, we explore the evolution of nanostructures

in the diblock films during solvent annealing at room temperature and during subsequent thermal annealing for two different scenarios: Annealing for a short time prior to thermal conversion and annealing for a long time during which thermal conversion is fully underway. We show that these morphological changes are consistent with thermodynamic considerations and with the effects that the conversion process has on the overall thickness of the films as discussed in the previous section.

4.4.2.1. Structural Development During Solvent Annealing. As indicated previously in Figure 4.2, the first step in processing our precursor PtBMA-PMMA films is performing solvent annealing in order to plasticize the material and generate ordered morphologies prior to starting the thermal deprotection process. For this diblock, volatile organics such as THF can work effectively to mobilize both blocks, though exposing the sample for too long to THF vapor (more than $\sim$1 to 2 hours) may completely disorder the nanostructure. Therefore, 90/10 molar ratio mixtures of THF and 2EH were used to control the THF vapor pressure for solvent annealing. *In situ* GISAXS measurements were conducted to monitor the structure of the film during the annealing process at room temperature for up to 2 hours. Figure 4.5a-f shows a series of patterns taken with the incident x-ray angle slightly above the polymer critical angle ($\theta_i = 1.03\ \theta_{c,film}$), providing information from the entire extent of the film. The as-spun cast morphology according to Figure 4.5a consists of deswollen spherical micelles which lack good ordering. A layer of micelles at the surface of the film contributes to a set of long vertical rods observed in the pattern (also seen more prominently in a pattern taken below the polymer critical angle, $\theta_i < \theta_{c,film}$ - not shown), while a semicircular ring (seen only for $\theta_i > \theta_{c,film}$) corresponds to partially disordered microdomains in the interior of the film. Analysis of the first-order
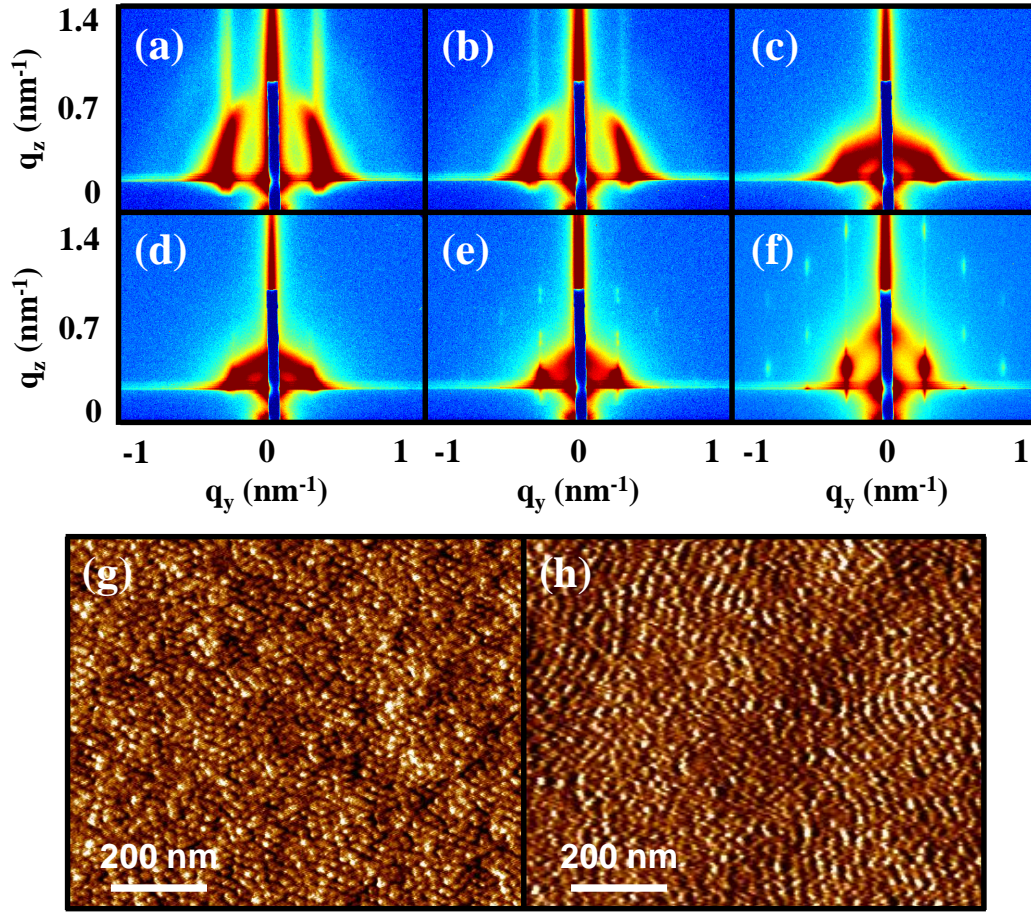
Figure 4.5. GISAXS patterns ($\theta_i = 1.03\ \theta_{c,film}$) of a P$t$BMA-PMMA film (a) as spun cast, during solvent annealing in a 90/10 THF/2EH mixture at room temperature for (b) 10 minutes, (c) 30 minutes, (d) 1 hour, (e) 2 hours, and (f) after solvent removal. Also shown are AFM phase images of the film surface (g) as spun cast and (h) after solvent annealing for 2 hours and solvent removal.

peak from a horizontal line scan in q_y reveals that the spacing between micelles is around 19.0 nm. Figure 4.5g is an AFM phase image of the as-spun cast surface and confirms this observation. As the film is being solvent annealed (Figure 4.5b-d), we see the vertical rods quickly start to disappear and the semicircular ring collapses, corresponding to significant disordering of the as-spun cast structure both at the surface and in the interior of the

film. Due to solvent uptake, the spacing between the disordered microdomains increases along with the entire film thickness, swelling by $\sim 68\%$ according to *in situ* reflectivity measurements. After 2 hours of solvent annealing, individual diffraction spots start to appear as seen in Figure 4.5e, signifying the creation of an array of cylindrical micelles lying parallel to the substrate in a hexagonally packed fashion. Finally, upon fast removal of the solvent from the film (by opening the annealing chamber), the diffraction spots are shifted upward as seen in Figure 4.5f, corresponding to a collapse of the cylinders in the vertical direction in real space. In the horizontal direction, the cylinders are pinned by the substrate and alter little. Therefore, the lattice after drying is a distorted hexagonal lattice (or centered rectangular lattice). From a simulation of peak positions as depicted in Figure 4.8a, the exact lattice constants are determined to be $a = 24.8$ nm (horizontal direction) and $c = 28.8$ nm (vertical direction) as defined on the diagram in the figure, translating to a distortion of 33% relative to a perfect hexagonal lattice. The coherent scattering domain size, estimated from the FWHM of the peaks, is ~ 300 nm in the horizontal direction and ~ 80 nm in the vertical direction. We must note that a GISAXS pattern taken with $\theta_i < \theta_{c,film}$ (see Figure 5.6c) does not exhibit any high-order diffraction spots. Appropriately, Figure 4.5h is an AFM phase image of the solvent annealed and dried PtBMA-PMMA film, showing the indication of only short parallel cylinders on the surface. Based on the fact that high-order diffraction spots appear in our GISAXS patterns only for $\theta_i > \theta_{c,film}$, we suspect that well-stacked cylinders with a high degree of ordering only exist in the interior of the film. Nevertheless, this structure represents a significant improvement from the as-spun cast one and is in a more equilibrium morphology appropriate for the volume fractions of these polymer blocks.
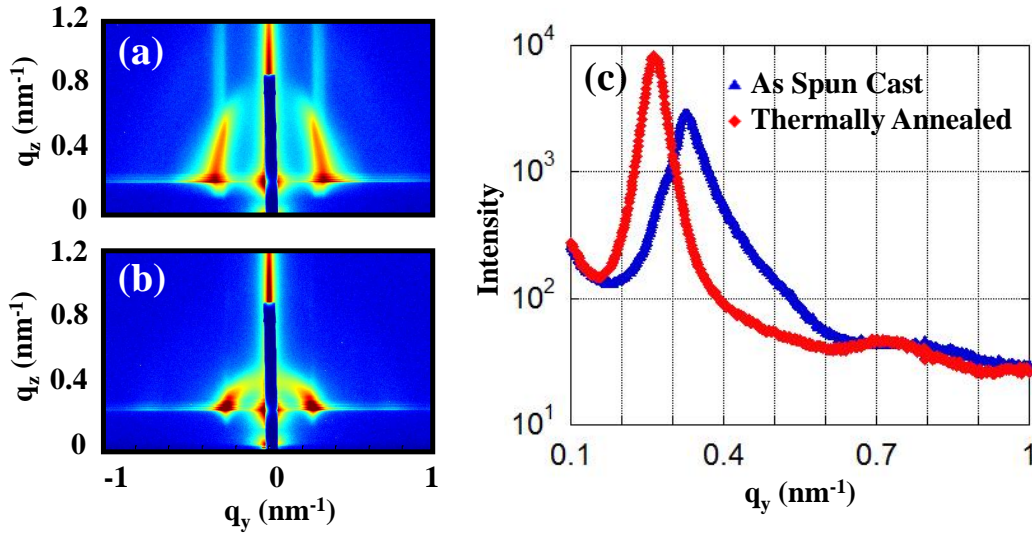
Figure 4.6. GISAXS patterns ($\theta_i = 1.03\,\theta_{c,film}$) of a P$t$BMA-PMMA film (a) as spun cast and (b) directly thermally annealed at 160 °C for 12 hours, without first being subjected to solvent annealing. Horizonal line scans at $q_z = 0.23$ nm^{-1} for both patterns are compared in (c). The spacing between microdomains (according to the position of the first-order peak) increases from ~19 to 24 nm.

As mentioned in the background, this solvent annealing step is quite important for providing a head start for the generation of ordered morphologies in the diblock film. If thermal annealing were directly performed on a PtBMA-PMMA film that had not received the solvent annealing treatment, then there would not be enough time for major structural organization to occur before the system converts to PMAA-PMMA and becomes kinetically frozen. As a comparison with the behavior observed in Figure 4.5, we present in Figure 4.6 the result seen for a PtBMA-PMMA film after undergoing direct thermal annealing at 160 °C for 12 hours, without first being subjected to solvent annealing. Instead of an improvement in order, the GISAXS pattern suggests that the quality of the overall structure deteriorates upon heating and, in particular, the layer of as-spun
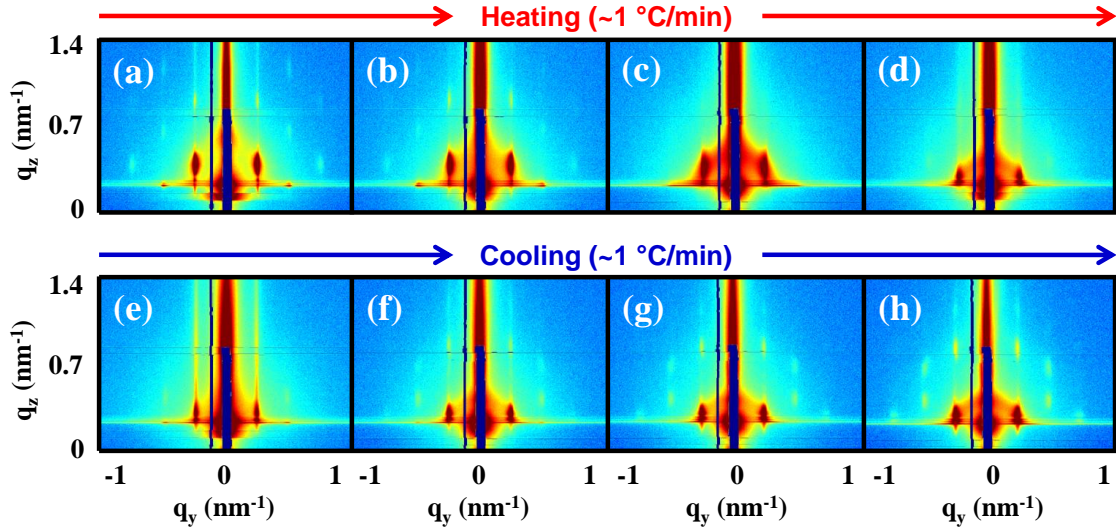
Figure 4.7. GISAXS patterns ($\theta_i = 1.03\,\theta_{c,film}$) of a solvent annealed PtBMA-PMMA film undergoing thermal annealing at 160 °C for 4 hours, which does not convert the diblock. Shown are patterns taken during heating at (a) 120 °C, (b) 133 °C, (c) 145 °C, and (d) 157 °C. After annealing for 4 hours, shown are patterns during cooling at (e) 157 °C, (f) 133 °C, (g) 121 °C, and (h) 111 °C. The heating and cooling rates are both ~1 °C per minute.

cast spherical micelles at the surface completely disintegrates. Most importantly, high-order diffraction spots never have a chance to appear, demonstrating that well-ordered morphologies cannot be achieved with direct thermal annealing of the film.

4.4.2.2. Structural Development During Thermal Annealing Prior to Reaction. After executing the necessary solvent annealing step to induce ordered morphologies in our precursor PtBMA-PMMA films, it was then appropriate for thermal annealing to be performed to convert the films to PMAA-PMMA. Our TGA results estimate that an annealing time of at least 72 hours at 160 °C or 18 hours at 180 °C is required for full conversion. Due to this extended length of time, we performed *ex situ* thermal annealing on most of our samples and examined the structure with GISAXS at various points
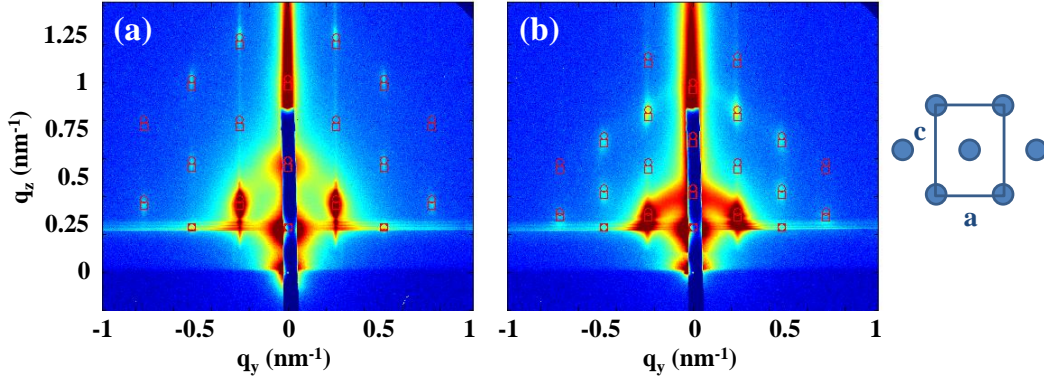
Figure 4.8. GISAXS patterns ($\theta_i = 1.03\ \theta_{c,film}$) of (a) dried P$t$BMA-PMMA film after solvent annealing in a 90/10 THF/2EH mixture for 2 hours and (b) after subsequent thermal annealing at 160 °C for 4 hours. Red circles and squares correspond to simulated diffraction peaks due to the reflected and transmitted beams, respectively. The patterns correspond to cylinders stacked parallel to the substrate. The packing motif is that of a centered rectangular lattice distorted in the film thickness direction (see schematic). The lattice constants are (a) $a = 24.8$ nm and $c = 28.8$ nm, and (b) $a = 26.9$ nm and $c = 44.3$ nm.

of the conversion after retrieving them from the vacuum oven. The samples were given time to cool significantly before the oven was opened and therefore were never quenched. This method helped to protect the nanostructure inside the films and prevent undesirable roughening of the film surface. We, however, first performed *in situ* thermal annealing on a PtBMA-PMMA film for a short length of time, allowing us to gather structural data at high temperatures with GISAXS. *In situ* thermal annealing was performed for no longer than 4 hours, consequently resulting in a conversion of no more than 1%. This process permitted us to observe the reorganization of the film without the additional complication associated with the conversion process. Figure 4.7 shows a series of GISAXS patterns of a PtBMA-PMMA film taken during heating as well as during cooling after a 4-hour hold at 160 °C. The heating and cooling rates were estimated roughly to be around 1 °C per
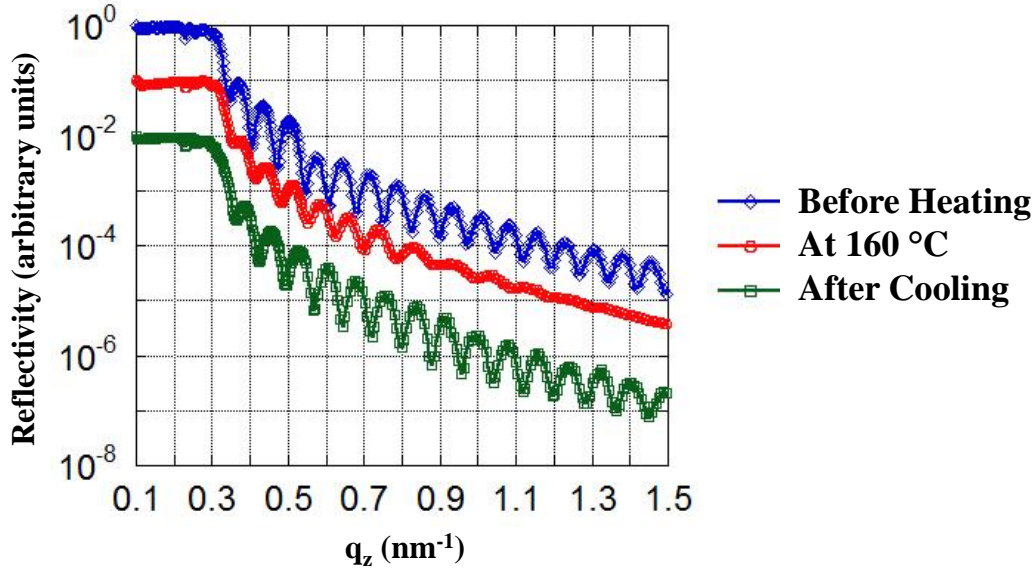
Figure 4.9. Reflectivity data for a solvent annealed PtBMA-PMMA film prior to thermal annealing (collected at room temperature), during thermal annealing at 160 °C, and after cooling (collected at room temperature). The film was annealed for ∼4 hours. The curves are shifted vertically for clarity.

minute, but data were always collected at fixed temperatures that were stabilized for ∼10 minutes during the heating or cooling process. Here, we see that the diffraction spots obtained after solvent annealing can be retained up to a temperature of ∼120 °C, which is around the glass transition temperature of both polymer blocks (Figure 4.7a). Beyond this temperature, all spots except the first-order peak disappear as seen in Figure 4.7b-c, indicating the loss of good ordering of the parallel cylinders and the initiation of a major restructuring and reorganization event. A noticeable shift in the position of the first-order peak toward smaller q_z is seen upon reaching ∼160 °C (Figure 4.7d), suggesting that this new, larger micelle spacing that has formed is more thermodynamically favorable than before. After 4 hours of annealing at ∼160 °C, we see in Figure 4.7e that a set of long rods

appears in the GISAXS pattern. This feature, along with reflectivity data taken at ∼160 °C (Figure 4.9) showing duller fringes, suggests that the surface of the film has developed roughness bumps from the PMMA cores that are physically emerging from the top of the PtBMA matrix. Upon slowly cooling the film, the surface roughness improves and we see in Figure 4.7f-h that the set of long rods give way to become individual diffraction spots, which appear now in different locations compared to those before thermal annealing. These spots again correspond to well-ordered cylindrical micelles stacked parallel to the substrate. From a simulation of peak positions as depicted in Figure 4.8b, the exact lattice constants are determined to be $a = 26.9$ nm (horizontal direction) and $c = 44.3$ nm (vertical direction) as defined on the diagram in the figure, translating to a distortion of now only 5% relative to a perfect hexagonal lattice. Thus, this structure is clearly a more thermodynamically favorable packing geometry containing cylindrical micelles in a hexagonally packed fashion.

4.4.2.3. Structural Development During Thermal Annealing with Reaction. The question now regards whether the hexagonally packed cylindrical micelles with the high degree of ordering obtained in the previous section can be retained with a much longer thermal annealing treatment, enough for conversion of the diblock into PMAA-PMMA. An obvious concern is the inevitable decreasing film thickness associated with the thermal deprotection process as the reflectivity analysis has shown. Additionally, both the PtBMA matrix and PMMA cores are sufficiently mobile for some reorganization to occur. Figure 4.10 shows GISAXS patterns of the diblock taken at room temperature after *ex situ* thermal annealing at 160 °C for 6, 24, 48, and 72 hours. As can be seen in Figure 4.10a-b, the series of diffraction spots identical to the one in Figure 4.7h
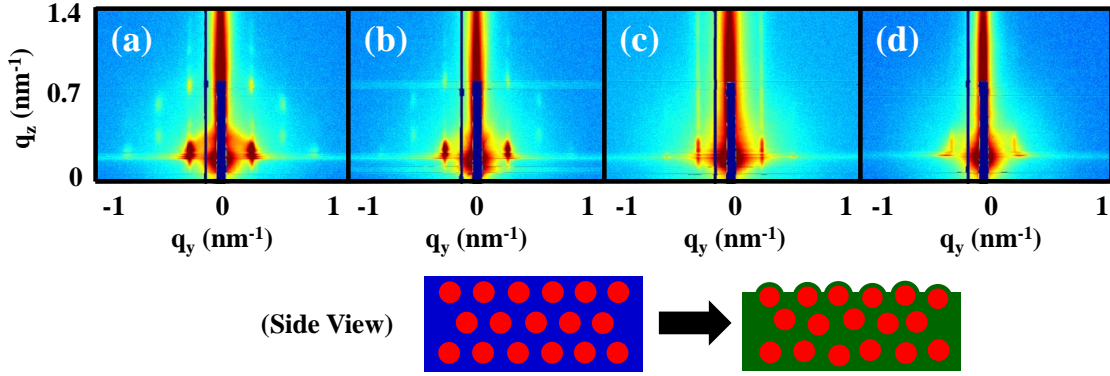
Figure 4.10. GISAXS patterns ($\theta_i = 1.03\ \theta_{c,film}$) of a solvent annealed PtBMA-PMMA film after thermal annealing at 160 °C for (a) 6 hours, (b) 24 hours, (c) 48 hours, and (d) 72 hours. The data were collected at room temperature. The corresponding percentage conversions of the film into PMAA-PMMA are approximately (a) 3%, (b) 25%, (c) 89%, and (d) 99%. Also shown is an illustration (side view) depicting the structural changes in the film during the thermal deprotection procedure.

are retained up to at least 24 hours of annealing at 160 °C, corresponding to a percent conversion to PMAA-PMMA of ∼25%. After 48 hours of annealing (Figure 4.10c), a set of long rods that normally appears at high temperatures (as in Figure 4.7e) is retained even after cooling, signifying that enough of the matrix material has converted to PMAA that the structure is now kinetically frozen. As mentioned before, the long rods correspond to the emergence of PMMA cores from the film surface, with the thickness of the entire film having decreased by almost ∼40% at this point. The absence of high-order diffraction spots implies the packing geometry has been physically perturbed enough to deviate from a perfect hexagonal lattice, where cylindrical micelles no longer possess a high degree of ordering. Finally, after 72 hours of annealing (Figure 4.10d), the ordering of the micelles both at the surface and in the interior of the film is essentially lost due to the significantly reduced film thickness, which is clearly unable to accommodate the

original, thermodynamically favorable lattice. Therefore, a rather disordered system of microdomains is obtained in the final fully converted PMAA-PMMA film. We also note that annealing the same system using a temperature of 180 °C results in almost identical behavior as that of 160 °C, with disordered micelles obtained at the end of the conversion process. This reduction in the order of the cylindrical micelles is very difficult to avoid in the thermal conversion process that we have used. As mentioned in the background, acid-catalyzed deprotection at lower temperatures may be a better alternative for maintaining good ordering during the conversion of the *tert*-butyl methacrylate groups to methacrylic acid.[114,115]

4.5. Conclusions

The thermal deprotection of P*t*BMA-PMMA diblock copolymer films is a subtle procedure that may not necessarily lead to ordered morphologies in converted PMAA-PMMA films. However, by solvent annealing the precursor P*t*BMA-PMMA films using a volatile common solvent, kinetically trapped spherical micelles can be mobilized to yield other nanostructures such as cylinders that are well-ordered. The high degree of packing of these cylindrical micelles can be retained up to at least 25% conversion of the diblock to PMAA-PMMA via thermal annealing. Beyond this point, the hexagonal packing geometry of the micelles cannot be accommodated, resulting in the loss of good ordering and elimination of the hexagonal lattice.

CHAPTER 5

Synchrotron Radiation Techniques for Investigating Soft Materials

5.1. Introduction

The content of this chapter is intended to serve as a practical guide for readers who are interested in applying synchrotron radiation to their investigation of soft materials, especially polymers. The techniques to be presented in this chapter are categorized into two scattering geometries, reflection and transmission, applicable for looking at a wide range of soft material systems. While the basic principles behind these techniques are to be covered to some degree, focus here is placed more on the practical matters for successfully carrying out experiments using these techniques. General guidelines for proper sample preparation, data collection, and analysis of results are discussed. Comments are also made regarding potential challenges and pitfalls that may be encountered in the process, all of which are based on the author's own experiences. All experiments were performed at the Advanced Photon Source at Argonne National Laboratory.

5.2. Reflection Geometry

5.2.1. X-ray Standing Waves via Total External Reflection

The technique of x-ray standing waves generated via total external reflection from an x-ray mirror (TER-XSW) can be viewed as a powerful structural probe for thin films and

is primarily used for obtaining the distribution of high-Z marker atoms as a function of distance from the x-ray mirror with subnanometer resolution. In the area of soft materials, this technique has been successfully applied in the past to study the distribution and motion of gold nanoparticles embedded in low-Z polymer matrices.[80,125–127] Through *in situ*, real-time experiments carried out above the glass transition temperature of the polymers, both Guico and Hagman were able to probe the diffusive behavior of the gold particles as well as that of the polymer chains, allowing diffusion coefficients to be calculated. Consequently, measurements of this mobility provided a direct understanding of the polymer-metal interactions and substrate effects that were playing a considerable role in these systems. The TER-XSW technique has also been previously applied by Wang *et al.* to observe structural changes in membranes in response to thermal annealing[79] as well as ion binding at a charged membrane/water interface,[128] making use of zinc as the high-Z markers. As demonstrated by these experiments, the high spatial resolution combined with the *in situ* annealing and incubation capabilities that can be realistically achieved nowadays makes TER-XSW a very attractive approach for investigating soft materials in the thin film geometry.

The basic principle of TER-XSW has already been introduced in Chapter 3 and has also been covered extensively in literature.[129] To review briefly, an x-ray standing wave is generated from the interference of incident and specular-reflected x-ray plane waves that have undergone total external reflection from an x-ray mirror. Figure 5.1 illustrates the geometry of this effect. It is apparent here that the period of the standing wave given by $D = \lambda/2\sin\theta$ decreases as the incident x-ray angle θ is increased (λ is the wavelength of the incident x-rays). The expression for the electric field intensity I is thus given as a function
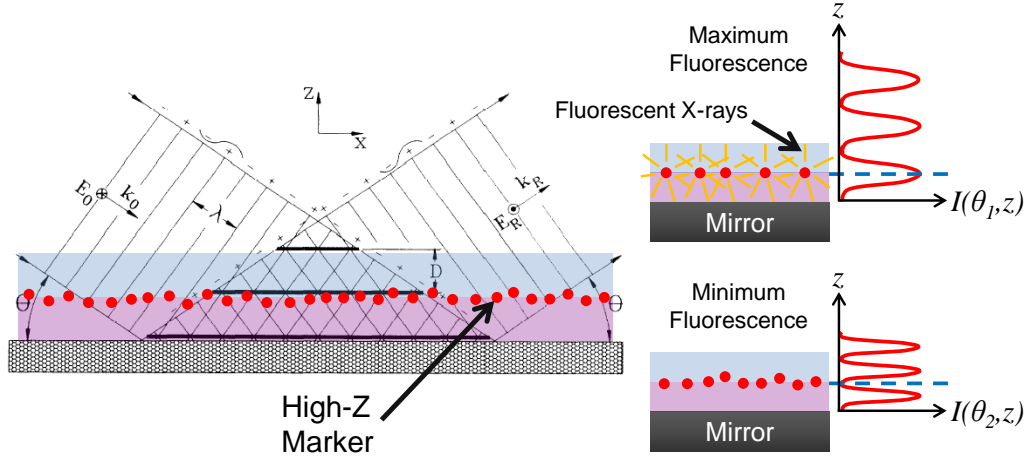
Figure 5.1. Illustration showing an x-ray standing wave field generated from the interference of incident and reflected plane waves (adapted from Bedzyk *et al.*[77]). Also depicted on the right are electric field intensity profiles as a function of distance from the mirror z for two different incident x-ray angles θ_1 and θ_2. Due to this changing intensity profile with incident angle, the fluorescence signal generated from a thin layer of high-Z markers above the mirror surface varies with incident angle as well.

of both incident angle θ and distance above the mirror surface z (see equation 3.1). The collapsing motion (along with a phase shift) of the standing wave with increasing θ is the key to probing the distribution of high-Z markers above the mirror. As shown in Figure 5.1, when an antinode of the standing wave coincides with the marker layer, maximum fluorescence is produced from the markers (assuming that the incident x-ray energy is above the absorption edge of the marker atoms). On the other hand, fluorescence is at a minimum when a node coincides with the marker layer. Therefore, a certain number of oscillations are observed in the fluorescence yield Y versus θ curve depending on the number of nodes and antinodes that pass through the marker layer as θ increases from 0 to the critical angle of the mirror θ_c. This behavior can be used to estimate the distance of the marker layer from the mirror via the handy formula $(X - 0.5)D_c$, where X is the

number of oscillations observed below θ_c and $D_c = \lambda/2\sin\theta_c$ is the critical period of the standing wave. More oscillations result when the marker layer is placed farther away from the mirror. On the other hand, if the marker layer is very close or adjacent to the mirror, fluorescence oscillations become irregular and are not very well defined, and the formula above may not be that useful. The formal way to deconvolute the marker distribution $\rho(z)$ from Y is through equation 3.2, where a model for $\rho(z)$, such as a Gaussian function, must be assumed. In this way, the sharpness of the oscillations can also be accounted for, which dictates how broad the distribution is. Through a rigorous fitting routine, values for the model parameters (e.g. peak position and width) that minimize the error between the fluorescence data and prediction can be accurately determined. One can obviously imagine that the more apparent oscillations that exist in the data, the easier and more confident the modelling process and results are going to be. In fact, oscillations that occur at larger θ are generally more sensitive to the fitting parameters than those at smaller θ, since the shape of the standing wave at larger θ is narrower and thus, in a sense, can more finely probe the marker layer.

In light of these properties of the TER-XSW technique, a few necessary suggestions regarding sample preparation must be made. The first and most important recommendation is that the high-Z marker layer should be thin and well-defined for the technique to be sensitive. Specifically, the thickness of the marker layer should not be much greater than the XSW period D, which reaches its smallest value at the critical angle of the mirror θ_c. Thus, in general, this thickness should be no more than a few nanometers. If the layer is too thick, then there can be the situation where both a node and antinode of the standing wave simultaneously hover over the layer. For such samples, the oscillations in

the fluorescence data become diffuse and not very well defined. In the most extreme case, only a single, broad oscillation with no features is observed. While fitting may still be attempted on the data, it must be cautioned that adjustments to the model parameters for the marker distribution of even up to a few tens of angstroms may not result in a noticeable change in the predicted fluorescence curve. With such small differences and the natural error or fluctuations typically associated with any data collection, one therefore may have difficulty obtaining confident parameter values with angstrom accuracy in such cases. For the second recommendation, the last paragraph has already alluded to the fact that the marker layer should be placed some distance away from the mirror so that some oscillations in the fluorescence data may be generated. While not mandatory, such a sample geometry can result in a cleaner looking fluorescence curve. A low-Z spacer layer such as a polymer film placed between the mirror and the marker layer generally takes care of this issue. For the third recommendation, it must be noted that attention must also be paid to any overlayers placed above the marker layer, which, like the marker layer, should not be unreasonably thick. Since the x-ray beam must travel through the overlayers to reach the marker layer, attenuation of the x-rays in the overlayers is something that must be taken into consideration. For instance, in an extreme case of a water layer or membrane with a thickness of several microns placed at the top of a sample, the reflectivity can lose a significant amount of intensity below θ_c as the optical path length of the x-rays may become as large as a few centimeters. Consequently, the shape and quality of the fluorescence curve can also become seriously affected. Overall, a sample most suitably designed for a TER-XSW experiment should have a total thickness above the mirror that is kept within the range of several tens to a few hundreds of nanometers.
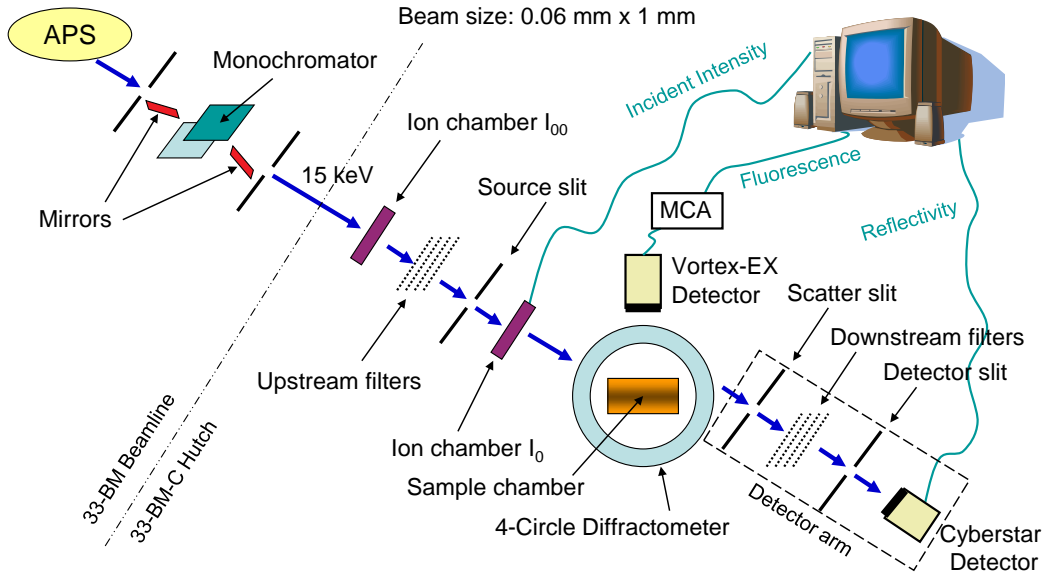
Figure 5.2. Schematic of the TER-XSW setup at the 33-BM beamline at the Advanced Photon Source. The Vortex-EX detector is placed as close to the sample chamber as possible, perpendicular to the beam direction.

The layout for a TER-XSW experiment is reasonably straightforward and can be readily set up on a beamline that offers scattering capabilities. The x-ray energy at the beamline should be tunable so that a proper energy right above the absorption edge of the marker atoms of interest may be chosen. Moreover, the availability of a diffractometer usually ensures proper sample manipulation for alignment and measuring reflectivity. For studies on soft material samples, it is also suggested (but not mandatory) that the experiment be conducted on a bending magnet (BM) beamline instead of an insertion device (ID) beamline, since the former is able to provide a much smaller beam flux density (by a few orders of magnitude), significantly reducing the probability of radiation damage to the samples.[130] A schematic of a typical TER-XSW setup at the 33-BM beamline[131]

is shown in Figure 5.2. A double-crystal monochromator is involved in selecting the x-ray energy. A motorized or fixed slit placed upstream from the sample is used to define the size of the beam that strikes the sample. The beam should be made as small as possible in the z direction so that it can be approximated as a plane wave. Usually, a beam height of several tens of microns is acceptable. The required data for analysis are the incident intensity, reflectivity, and fluorescence, which are respectively collected by an ionization chamber, NaI(Tl) scintillation detector (Oxford Cyberstar X1000), and a Vortex-EX single-element silicon drift detector. The ionization chamber and Cyberstar detector are chosen for their ability to measure high count rates, while the Vortex-EX detector is chosen for its excellent energy-resolving capability. The setup also consists of filters, usually made of Cu, Al, Mo, Ti or other metallic films with known thicknesses, which can be moved into and out of the beam to control its attenuation. To this end, the amount of attenuation provided by each filter can be predicted[132,133] and should also be checked with the direct x-ray beam prior to starting data collection on the sample. Upstream filters are used to prevent radiation damage to the sample, while downstream filters are required to protect the Cyberstar detector from receiving too high of a count rate, which can affect its performance and introduce an inevitable dead time.[134] In general, during a TER-XSW measurement, more attenuation of the reflected beam (downstream) is needed below θ_c due to the high reflectivity, and this beam should be attenuated less above θ_c where the reflectivity drops significantly by several orders of magnitude. X-ray fluorescence emitted from marker atoms within the sample may sometimes also produce too high of a count rate in the Vortex-EX detector, causing saturation. Such a scenario can especially happen in a sample with a relatively thick marker layer that contains
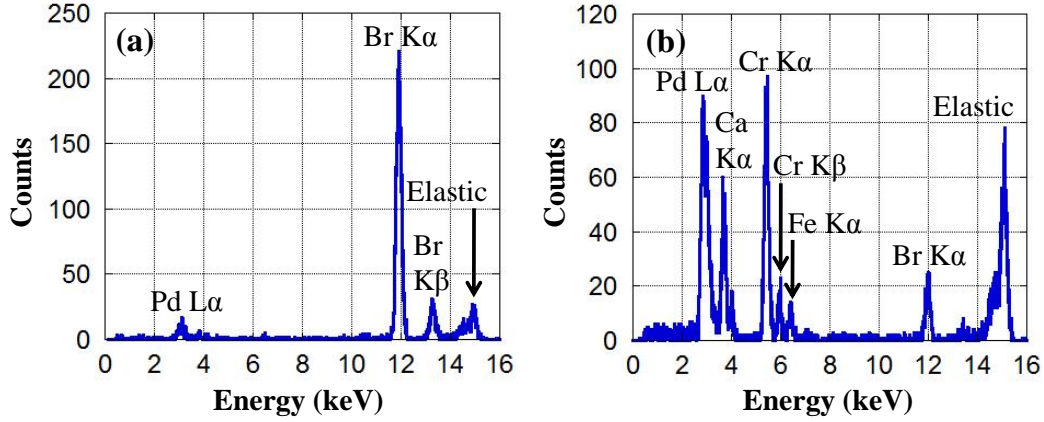
Figure 5.3. X-ray fluorescence spectra captured by a Vortex-EX detector at two incident x-ray angles for a PS/PBrS/P4VP sample prepared on top of an x-ray mirror consisting of Pd, Cr, and Si (from top to bottom). The incident x-ray energy is 15 keV. Shown (a) on the left is a spectrum taken below the critical angle of the mirror θ_c, while (b) on the right is a spectrum taken above θ_c.

more than enough marker atoms to generate fluorescence. To alleviate such a problem, either the Vortex-EX detector can be moved farther away from the sample or filters can be placed in front of the detector. If appropriate, upstream filters may also be used to reduce the incident intensity on the sample, which can decrease the fluorescence count rate that is produced. Note that this option also brings down the reflectivity signal, requiring readjustment of the downstream filters. Finally, some beamlines are also equipped with a harmonic rejection mirror system used for eliminating high-order harmonics from the incident beam. The 7-ID beamline, for example, has Kirkpatrick-Baez (KB) mirrors placed upstream from the sample for this purpose as well as for beam focusing. Harmonic discrimination may also be handled by properly setting the gain and voltage levels on the Cyberstar detector. For more detailed information on a TER-XSW setup, the reader is asked to refer to the Ph.D. theses of Wang, Guico, and Hagman.[125,126,129]

For data collection, a macro is written for simultaneously measuring at each incident angle the reflectivity and fluorescence via a conventional $\theta - 2\theta$ scan. The scan is usually broken up into several shorter scans that allow for filter changes in between and also account for various scan step sizes that are appropriate in different angular regions. Usually, the thicker the sample, the more data points are needed to trace out the finer features in the reflectivity curve. A multichannel analyzer (MCA) connected to the Vortex-EX detector is responsible for capturing the entire fluorescence spectrum at every incident angle. Counts are recorded by the MCA in 2048 channels, each of which corresponds to a specific energy. From the spectrum, the fluorescence signal that belongs to the emission at a characteristic energy from the layer of marker atoms in the sample is extracted. This task can be completed by setting the program to capture a specific region of interest (ROI) on the spectrum that encloses the emission peak, essentially summing all the counts in the selected range of channels (assuming that the background is low and other peaks are not overlapping). The total fluorescence count (summation of counts in all 2048 channels) should also be monitored for detector saturation and possible dead time corrections that may be required. When choosing a high-Z marker for a TER-XSW experiment, it must be ascertained that this element of interest only exists in the expected location in the sample. Due to the high sensitivity of TER-XSW, any contamination of the element in the sample chamber, substrate, and other objects nearby can also be picked up and counted in the fluorescence signal. Moreover, the emission peak of this element should ideally not overlap with emission peaks from other elements in the fluorescence spectrum. If there is overlapping, then a Gaussian function should be used to fit and resolve the single peak, with the area under the Gaussian subsequently quantified as the fluorescence intensity.

Figure 5.3 shows ideal examples of MCA fluorescence spectra collected from a homopoly-mer multilayer film comprised of poly(styrene), poly(4-bromostyrene), and poly(4-vinyl pyridine) (PS/PBrS/P4VP) situated on an x-ray mirror comprised of Pd, Cr, and Si from top of bottom. In this case, the incident x-ray energy is 15 keV and the Br Kα and Kβ emissions at 11.9 and 13.3 keV originating from PBrS are of interest. At an incident angle below θ_c, as the standing wave interrogates the polymer multilayer, a reasonably strong Br signal surrounded by very low background with no other contaminants present is seen. At an incident angle above θ_c, fluorescence signals from other elements originating from the interior of the x-ray mirror are detected, all harmlessly emitting at much lower energies than bromine. The situation may be more subtle to confront in other cases, as it should be reminded that the higher the incident x-ray energy chosen, the more elements that may be excited and populate the fluorescence spectrum.

For data processing and analysis, the reader is once again asked to refer to the Ph.D. theses of Wang, Guico, and Hagman[125,126,129] for in-depth information regarding the nec-essary geometric corrections, normalizations (e.g. incident intensity), and other adjust-ments (e.g. attenuation changes) that should be made to the TER-XSW data prior to fitting. Briefly, one of the important geometric corrections involves considering variations in the beam footprint with increasing incident angle θ. At very low incident angles, only a fraction of the total incident beam falls on the sample as the footprint exceeds the length of the sample. As the incident angle is increased, the footprint size recedes until the entire incident beam falls on the sample. Specifically, the reflectivity data should be corrected according to the factor $\min\{1, (L_S \sin\theta)/H\}$, where L_S is the length of the sample along the beam direction and H is the beam height. The changing footprint size also affects the

fluorescence data since the illuminated area on the sample from which the fluorescence counts originate is not fixed. At low incident angles, the illuminated area is constant with the length of the footprint L being equal to L_S, but for $\theta > \sin^{-1}(H/L_S)$ the footprint size recedes such that L becomes smaller than L_S. Accordingly, a correction factor to the fluorescence data involving an integration across the illuminated length of the sample from 0 to L should be made. This correction should also account for the solid angle of the fluorescence detector, where the size of the detector opening and the horizontal distance from the opening to the illuminated area on the sample must be considered. This procedure effectively normalizes the data with respect to the changing illuminated sample area with the upper limit of integration L given by $L = \min\{L_S, H/\sin\theta\}$. Two Fortran programs are available in the Shull research group for interacting with TER-XSW data: *Padawan* takes the raw reflectivity and fluorescence scans (from SPEC files) and outputs the data in a clean format ready for analysis, and *Jedi* is the program that performs the necessary data corrections, theoretical calculations and simulations (refer to Table 5.1), and χ^2-minimizations to fit the reflectivity and fluorescence data. The appendix in the thesis of Guico provides more details on the *Jedi* program.[125]

5.2.2. Grazing-Incidence Small-Angle X-ray Scattering

The grazing-incidence small-angle x-ray scattering (GISAXS) technique[135,136] is another very powerful tool for the structural evaluation of thin films on solid substrates. Here, information from both in-plane and out-of-plane (with respect to the sample surface) is obtained, making the technique more and more popular for investigating a variety of

Table 5.1. X-ray Parameters for Selected Polymers and Metals Used for Simulations in the *Jedi* Program.

Material	X-ray Energy (keV)	Electron Density ($Å^{-3}$)	δ	β
PS	15	0.34	1.04×10^{-6}	3.42×10^{-10}
PBrS	15	0.45	1.39×10^{-6}	5.07×10^{-8}
P4VP	15	0.37	1.13×10^{-6}	4.17×10^{-10}
Pd	15	3.13	9.45×10^{-6}	2.76×10^{-7}
Cr	15	2.00	6.22×10^{-6}	2.08×10^{-7}
Si	15	0.70	2.16×10^{-6}	1.47×10^{-8}
P*t*BMA	7.35	0.34	4.31×10^{-6}	9.70×10^{-9}
PMAA	7.35	0.41	5.28×10^{-6}	1.48×10^{-8}
PMMA	7.35	0.39	4.93×10^{-6}	1.28×10^{-8}
Si	7.35	0.70	9.11×10^{-6}	2.46×10^{-7}

δ and β are the dispersion and absorption coefficients, respectively.

complex systems in materials science. The ability for GISAXS to be performed with synchrotron radiation has especially helped to establish a more elegant means for analyzing soft materials, including polymers, where their weakly-scattering nature is no longer of major practical concern. Real-time, *in situ* GISAXS experiments are particularly important for observing the structural evolution in polymer thin films during processing, providing direct guidance on generating and controlling specific morphologies that are relevant in many industrial and nanotechnology applications. Systems containing both polymer and metal are also very ideal for GISAXS measurements, since the electron density contrast between the two components is intrinsically high. In fact, in the study by Narayanan *et al.*,[137] the in-plane distribution and diffusion of gold nanoparticles embedded in polymer matrices were characterized with subnanometer resolution, complementing the TER-XSW out-of-plane diffusion studies by Guico *et al.*[80] Here, the GISAXS data collected are particularly of high contrast, due to an effect involving resonance enhancement of the electric

field intensity by x-ray standing waves in the total external reflection regime.[138] Moreover, the use of embedded gold nanoparticles are shown to perturb the resonance modes and affect the electric field intensity distribution as well, further improving the sensitivity of the spatial diffusion measurements.[137,139] Besides polymer-metal nanocomposite systems, GISAXS has also been widely applied in monitoring the self-assembly of nanostructures in block copolymer films. A quick search of literature shows that a large amount of *in situ* and *ex situ* experiments have been conducted on a diverse range of block copolymer systems, elucidating many interesting morphological transitions resulting from different processing strategies that are difficult to follow with other techniques.[44,94,97,140–144] Distinct regions from the surface to the interior (which includes buried interfaces) of the films are able to be resolved with GISAXS, while laterally the x-ray beam illuminates a macroscopically large area of the sample, resulting in statistically significant data which are more meaningful and reliable for analysis than those derived from local probes such as atomic force microscopy. The maturation and success of GISAXS in probing polymer thin films has rendered it an effective, efficient, and reliable technique for the investigation of many new, more complex soft material systems in years to come.

An introduction to the GISAXS technique can readily be found in literature.[14,15,145–147] To review the basics, like the TER-XSW technique, the GISAXS experimental geometry involves striking a thin film sample situated on an x-ray mirror with an incident x-ray beam at a grazing angle α_i, generally below the critical angle of the mirror α_c where total external reflection occurs. Here, the resulting off-specular scattering from the sample is of interest in the GISAXS technique and is captured with a two-dimensional area detector for a fixed incident angle α_i. The specular-reflected beam (reflectivity as a function of
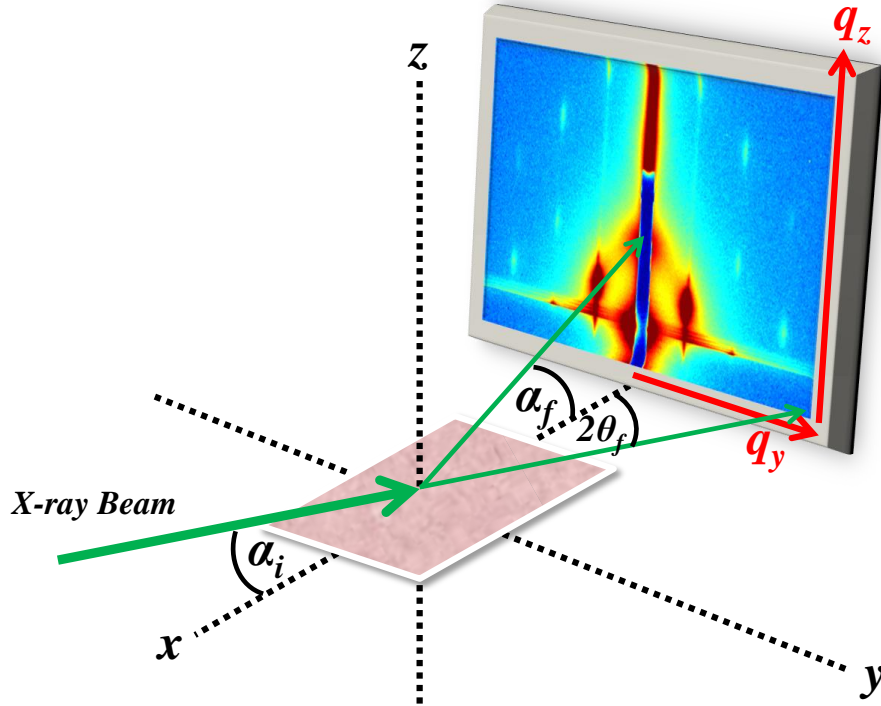
Figure 5.4. Schematic of the GISAXS experimental geometry. An x-ray beam impinges on the sample at an incident angle α_i, and the resulting off-specular scattering is captured with a two-dimensional area detector. Here, α_f and $2\theta_f$ are the out-of-plane and in-plane scattering angles, respectively. The GISAXS pattern is given in the q_y-q_z plane, where q_y and q_z are the in-plane and out-of-plane components of the scattering vector.

α_i) is also collected separately with a point detector for keeping track of the electric field intensity above the mirror and resonance enhancements that can occur at certain incident angles. Figure 5.4 shows a schematic of the GISAXS geometry. Here, α_f and $2\theta_f$ are defined as the out-of-plane and in-plane scattering angles, respectively. The pattern captured by the area detector is given in the q_y-q_z plane, where q_y is the scattering vector component parallel to the sample surface and perpendicular to the scattering plane and q_z is the component perpendicular to the sample surface. The third component q_x is coupled to q_z but is usually neglected since $q_x << q_z$.[14] All three components of the scattering

vector can be expressed in terms of α_f and $2\theta_f$ and are given as follows:

$$\vec{q} = \begin{pmatrix} q_x \\ q_y \\ q_z \end{pmatrix} = \frac{2\pi}{\lambda} \begin{pmatrix} \cos\left(\alpha_f\right)\cos\left(2\theta_f\right) - \cos\left(\alpha_i\right) \\ \cos\left(\alpha_f\right)\sin\left(2\theta_f\right) \\ \sin\left(\alpha_f\right) + \sin\left(\alpha_i\right) \end{pmatrix}. \tag{5.1}$$

Note that the condition $q_x = q_y = 0$, where $\alpha_i = \alpha_f$ and $2\theta_f = 0$, corresponds to specular scattering and belongs only to a single point on the GISAXS pattern (usually blocked by a beam stop due to its intensity being several orders of magnitude higher). The rest of the points are off-specular, collectively conveying information about the in-plane structure of the sample. Simple horizontal line scans in the q_y direction (at a constant q_z) can be used to pinpoint peaks that correspond to characteristic in-plane length scales or correlations present in the sample. For a block copolymer film, the location of the first-order peak may provide information about the characteristic spacing d between phase-separated microdomains such as micelles via the relationship $d = 2\pi/q_y$. Higher-order peaks at larger q may appear if there is good ordering of the microdomains. The arrangement of these peaks in the q_y-q_z plane can sometimes mirror the actual packing of the microdomains in real space as seen by the beam from a small grazing angle. For example, for a system of hexagonally packed cylindrical micelles oriented parallel to the substrate, individual diffraction spots arranged in a hexagonal fashion are directly observed on the GISAXS pattern as seen in Figure 4.8. If hexagonally packed cylinders are oriented perpendicular to the substrate, then long vertical rods are captured on the pattern. Here, an excellent example from the GISAXS work of Park *et al.*[44] shows that if the x-ray beam follows the (10) lattice line, then the ratios of the positions of these rods to that of the first-order rod

obtained from a horizontal line scan in q_y are given as 1, 2, 3, 4, etc., characteristic of the $(h0)$ planes where h is an integer. The same set of peaks is seen if the sample is rotated $60°$ about the sample surface normal. If the sample is rotated $30°$ or $90°$ about the surface normal with the x-ray beam now following the (11) or (21) lattice lines, then the ratios of the rod positions become 1, $\sqrt{3}$, $\sqrt{4}$, $\sqrt{7}$, etc., corresponding to the (hk) planes as determined by $\sqrt{h^2 + hk + k^2}$ with $h, k = 0, 1, 2, 3, ...$ At the other end of the spectrum, when higher-order peaks are not present for this type of analysis indicating a lack of good ordering, the GISAXS pattern is generally more ambiguous for interpreting the structure present, and complementary characterization with other techniques such as atomic force microscopy (AFM) or transmission electron microscopy (TEM) is often required.

When necessary, a GISAXS intensity map can be analyzed more rigorously with the scattering behavior predicted according to the distorted-wave Born approximation (DWBA),[118–122] which accounts for multiple scattering effects that cannot be neglected in the grazing-incidence geometry. Referring to Figure 3 in the paper of Stein *et al.*[118] that is specific to a block copolymer film comprised of microdomains, four types of scattering events involving combinations of diffraction from a microstructure in the film and reflection from the substrate must be considered. Defining the out-of-plane scattering vectors associated with these four events as $q_{z,1}$, $q_{z,2}$, $q_{z,3}$, and $q_{z,4}$, and the in-plane scattering vector as $q_\parallel = \sqrt{q_x^2 + q_y^2}$, the effective form factor F_{DWBA} for this case is given by

$$F_{\text{DWBA}} = T_i T_f F\left(q_\parallel, q_{z,1}\right) + T_i R_f F\left(q_\parallel, q_{z,2}\right) + T_f R_i F\left(q_\parallel, q_{z,3}\right) + R_i R_f F\left(q_\parallel, q_{z,4}\right), \quad (5.2)$$

where F is the classical form factor related to the shape of the microstructure (e.g. sphere, cylinder, etc.). T_i and T_f denote the amplitudes of the incoming and outgoing transmitted

waves and R_i and R_f denote the amplitudes of the incoming and outgoing reflected waves, all of which may be obtained from executing Parratt's recursion formulation.[81] The scattering intensity can then be theoretically expressed as

$$I\left(q\right) \propto \left|F_{\mathrm{DWBA}}\right|^2 S\left(q\right),$$ (5.3)

where S is the structure factor which describes the packing or arrangement of the microstructures in the film. In practice, in order to produce a simulated GISAXS intensity map from DWBA to compare with an experimentally obtained one, equations 5.2 and 5.3 are applied for scattering vectors q that correspond to specific (hkl) planes in an assumed lattice structure. Through a trial-and-error process, the assumed lattice constants (and therefore q_x, q_y, and q_z for each (hkl)) are gingerly adjusted until the locations (and intensity) of the simulated diffraction peaks in the q_y-q_z plane more or less match those seen on the experimental GISAXS pattern, confirming the lattice structure. Several computer programs are also available for analyzing GISAXS patterns, including NANOCELL,[148–150] FitGISAXS,[151] and IsGISAXS.[152] However, the reader is advised to understand the computations performed by these programs carefully to make sure the underlying theory and assumptions apply to the system being studied.

The typical setup for a GISAXS experiment is straightforward and is shown in Figure 5.5 for one at the 8-ID beamline.[153] Like in the TER-XSW setup, slits placed upstream from the sample are used to define the x-ray beam size, which should be as small as possible in the z direction so that it can be approximated as a plane wave. Here, the height of the beam is typically around 50 μm. Filters are also placed upstream to control
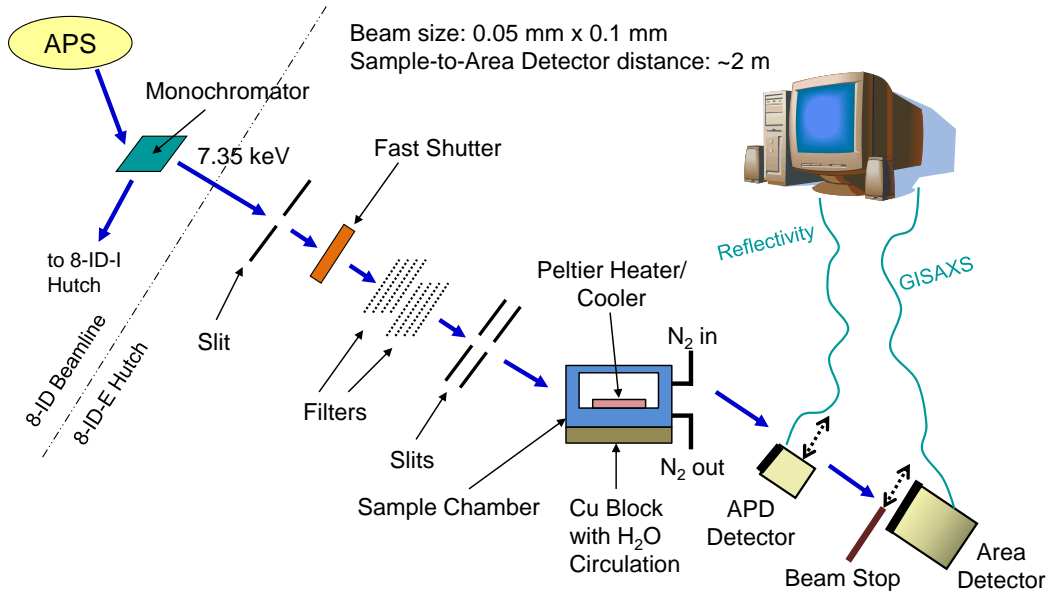
Figure 5.5. Schematic of the GISAXS setup at the 8-ID beamline at the Advanced Photon Source. The APD detector is moved into the beam for reflectivity measurements and out of the beam for GISAXS measurements.

the attenuation of the beam to prevent detector saturation (as described in the TER-XSW section) during both reflectivity and GISAXS measurements. A fast shutter is also utilized, which especially plays an important role when running time-resolved experiments. After the beam scatters off the sample, reflectivity is collected by vertically moving an avalanche photodiode detector (APD) into the path of the specular-reflected beam. The APD motor position and step size are calibrated in such a way that a conventional $\theta - 2\theta$ scan can be mimicked. The APD is moved out of the way for the GISAXS measurements, where patterns are collected by a large area detector (MAR165 CCD or PILATUS 1M pixel array) that sits much farther away. The distance between the sample and the area detector determines the q-range that is seen on the patterns. A low q-region is accessed with a large sample-to-detector distance, and vice versa. At the 8-ID beamline, the

sample-to-detector distance can be chosen to be either $\sim$1.3 or 2 m (total q-range of 0.05 to 2.5 nm^{-1} at 7.35 keV), permitting length scales on the order of a few nanometers to a few hundred nanometers to be probed. A silver behenate standard is typically used for finding the position of the direct beam on the two-dimensional image and measuring the exact sample-to-detector distance for correct pixel-to-q conversion. A movable lead beam stop is placed in front of the area detector to block along q_z the intense direct and specular-reflected beams. The sample sits in a chamber that permits *in situ* thermal and solvent annealing to be conducted. The temperatures of the sample and solvent inside the chamber can each be independently controlled with a Peltier heater/cooler. A copper block located underneath the chamber provides additional heating to the entire chamber via a constant water circulation from a temperature-controlled water bath. A constant flow of nitrogen or helium through the chamber should also be applied to minimize beam damage to the sample during x-ray measurements. The temperature of the sample may be heated to $\sim$100 °C with the Peltier, although with assistance from the water in the copper block heated to 80 °C, the sample temperature can reach a maximum of $\sim$160 °C. This procedure should be executed with caution and touching of the hot sample chamber should be avoided. For experiments that require much higher temperatures, a different chamber that can be placed under vacuum should be used.

For data collection, a reflectivity curve is typically obtained first via a conventional $\theta - 2\theta$ scan (see TER-XSW section) to pick out suitable incident angles below the critical angle of the x-ray mirror for subsequent GISAXS measurements. For a sufficiently thick polymer film prepared on top of a silicon substrate, the possibility exists for taking advantage of resonance-enhanced scattering at certain incident angles which occurs when the period
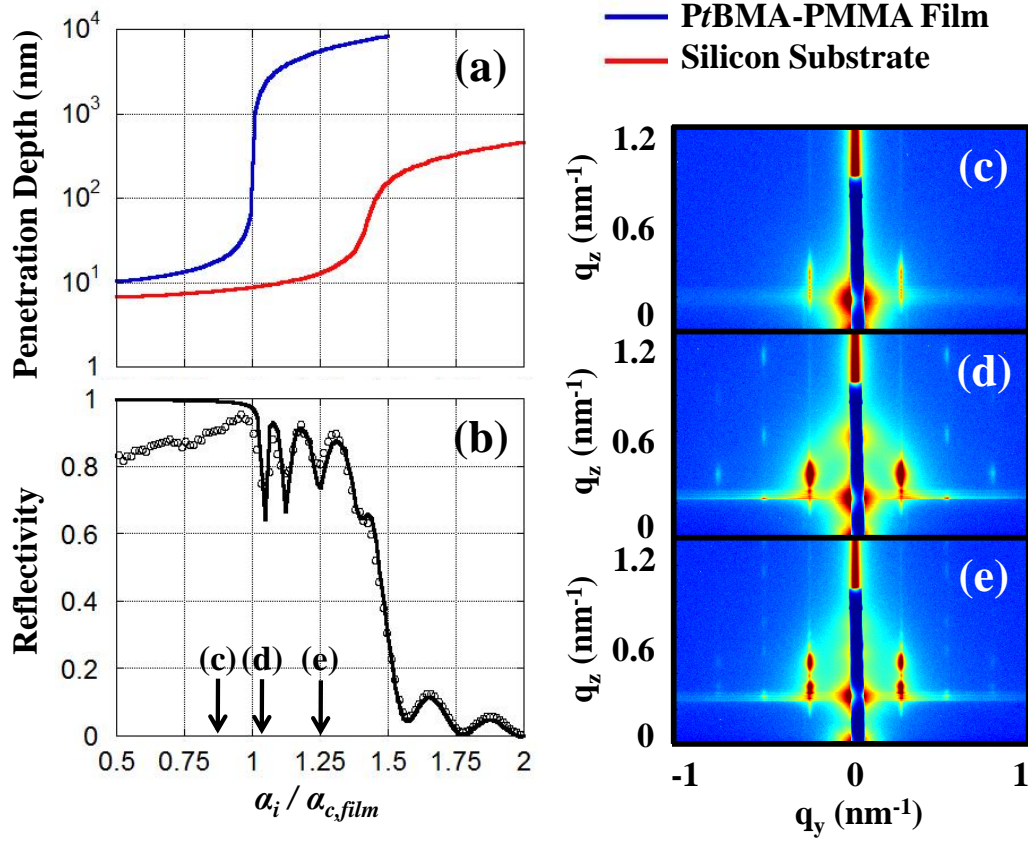
Figure 5.6. (a) Plots of x-ray penetration depth into a PtBMA-PMMA film and its silicon substrate given as a function of incident angle normalized by the critical angle of the film $(\alpha_i/\alpha_{c,film})$, and (b) corresponding x-ray reflectivity curve for the sample where the solid line is a fit to the data points. The arrows point to incident angles where GISAXS patterns as shown are collected: c) $\alpha_i = 0.87\ \alpha_{c,film}$, (d) $\alpha_i = 1.03\ \alpha_{c,film}$, and (e) $\alpha_i = 1.25\ \alpha_{c,film}$. The critical angle of the silicon substrate occurs at around $1.42\ \alpha_{c,film}$.

of the x-ray standing wave coincides with a submultiple of the film thickness, with the film acting as an x-ray waveguide.[137] These discrete incident angles exist between the film and mirror critical angles and are generally indicated by local minima in the reflectivity curve due to relatively more x-rays being trapped inside the film. An example involving a poly($tert$-butyl methacrylate)-poly(methyl methacrylate) (PtBMA-PMMA) film with

a thickness of $\sim$100 nm situated on top of a silicon substrate is shown in Figure 5.6b. Here, the first such minimum is seen right above the critical angle of the film $\alpha_{c,film}$, with a couple more sharp ones evident up to the critical angle of the mirror at $\sim$1.42 $\alpha_{c,film}$. The off-specular scattering intensity in the GISAXS patterns collected at these incident angles are much more enhanced and of higher contrast compared to ones taken at angles that correspond to maxima in the reflectivity curve. A thin polymer film of only a few tens of nanometers may not be sufficiently adequate to serve as an x-ray waveguide and consequently cannot provide resonance enhancement of the GISAXS patterns. The incident angle of the x-ray beam also dictates the depth at which the polymer film is probed. Figure 5.6a plots the penetration depth of the x-ray beam as a function of incident angle, shown for the PtBMA-PMMA film as well as the silicon substrate. A very sharp increase in the x-ray penetration depth into the film is evident when the incident angle transitions from just below $\alpha_{c,film}$ to just above $\alpha_{c,film}$. Thus, a GISAXS pattern taken below $\alpha_{c,film}$ is a reflection of the structure from only the vicinity of the film surface (a few tens of nanometers), while a pattern taken above $\alpha_{c,film}$ probes the entire depth of the film down to the polymer/substrate interface. Figure 5.6c-e shows GISAXS patterns collected at various incident angles below and above $\alpha_{c,film}$, demonstrating that there can be a remarkable difference in the structure at different depths of the film. In this case, the interior of the film appears to be much more highly ordered than the surface, with the lack of high-order diffraction spots below $\alpha_{c,film}$. The two patterns taken above $\alpha_{c,film}$ contain the same structural information. The only distinction seen is that a splitting in each of the diffraction spots, which are contributed by both reflected and transmitted

(from the back edge of the silicon substrate) x-ray beams, is more evident in the pattern taken at the higher incident angle.

Preparation of samples for a GISAXS experiment poses very few limitations. A wide range of film thicknesses from tens to hundreds of nanometers are appropriate for GISAXS. For the choice of substrate, silicon is most ideal, while metals such as Au may be accompanied by unwanted scattering which can bury the information generated by the polymer film. Thus, the lack of elemental specificity in GISAXS is somewhat of a disadvantage. Moreover, when working with two or more types of polymers, their electron density should be inspected for similarities, though a contrast of a few percent is usually satisfactory. The most important requirement for a GISAXS sample is that the length scale of the features to be probed in the film must fall within the appropriate q-range that can be accessed for a particular sample-to-detector distance. Thus, AFM or TEM measurements to establish a sense of the characteristic length scales in the sample are crucial prior to setting up for and running a GISAXS experiment. Usually, large length scales on the order of microns are difficult to probe with GISAXS at the 8-ID beamline. When more than one prominent length scale is present in the sample, the possibility also exists for an overlap of the scattering peaks, making analysis more challenging. Finally, it should be obvious by now that since GISAXS averages data over macroscopic distances and considers correlations in the structure being probed, isolated local features or abnormalities that are of interest in the sample cannot be resolved with this technique.
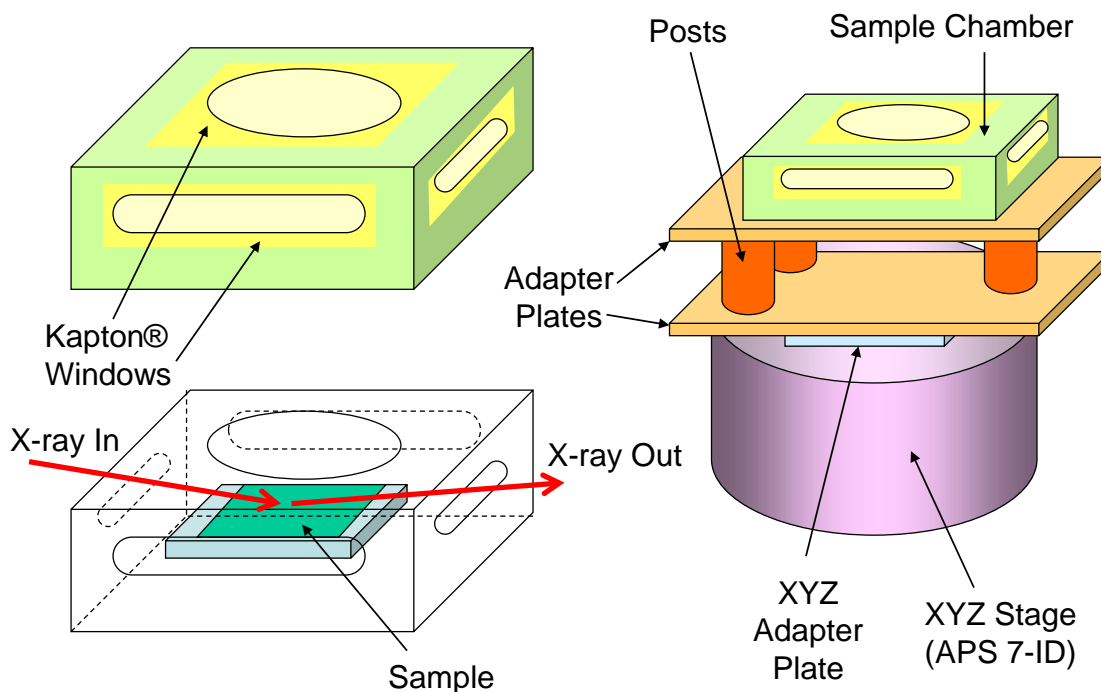
Figure 5.7. Schematic of a simple sample holder that can be used for TER-XSW experiments. Adapter plates and posts needed to install the holder at the 7-ID beamline are also shown. The sample holder was designed by Rafael Bras (Shull Group).

5.2.3. Sample Holder Design

A number of sample chambers and holders are available in the Shull research group and at the APS for conducting experiments requiring the reflection geometry. The first of these designs is a simple aluminum holder that can be used for TER-XSW or any kind of grazing-incidence scattering experiment as shown in Figure 5.7. Originally intended for *in situ* membrane inflation experiments with TER-XSW, the holder has Kapton® windows that exist on the top and sides for easy penetration of x-rays during reflectivity and fluorescence measurements at various orientations. The proper adapter plates for this holder have been made to fit to the XYZ translation stage at the 7-ID beamline as well as
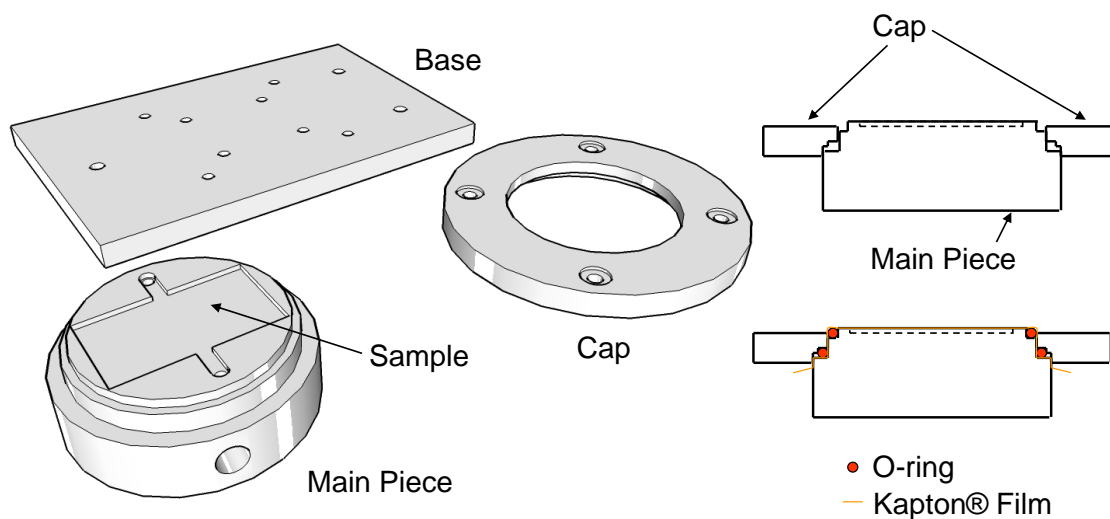
Figure 5.8. Schematic showing the parts of a liquid-solid interface cell that can be used for certain TER-XSW experiments where the presence of a thin liquid layer on top of a sample is required. A thin Kapton® or Prolene® film is placed over the top to trap the thin liquid layer.

a standard goniometer such as one used at the 33-BM beamline. The holder has also been utilized with the 18kW Rigaku rotating anode instrument for TER-XSW measurements in the J. B. Cohen X-ray Diffraction Facility at Northwestern University. No temperature control currently exists for this holder but appropriate modifications can be made to insert a cartridge heater into the body of the holder for heating and a thermocouple for measuring the temperature. The holder currently cannot be placed under vacuum or any type of gas environment such as nitrogen or helium. The holder was designed by Rafael Bras in the Shull group.

The second design is intended for use with a TER-XSW experiment that requires the top of the sample to be in constant contact with a liquid layer. For example, this setup might come in handy for a system where hydrophilic polymer brushes need to be swollen in water. The design and usage of this liquid-solid interface cell are based on those of

Libera and others[128,154] as shown in Figure 5.8. A liquid (e.g. aqueous solution) can be flowed into the cell through one of two ports and fill an area between the sample and a very thin Kapton® or Prolene® film of a few microns that covers the top. After incubation, a negative pressure is applied and maintained by withdrawing most of the liquid through the port using a syringe, leaving behind a ~ 2 μm-thin layer of the liquid on top of the sample for reflectivity and fluorescence measurements. The main body of the liquid cell is made out of Vespel® as it is chemically inert and resists radiation damage. The base and cap, which holds everything in place, are made out of aluminum. The o-rings used for sealing in the liquid are made out of Viton®.

As mentioned in the last section, a sample chamber that can be placed under vacuum and used for *in situ* thermal annealing experiments up to very high temperatures is available at the APS (8-ID beamline). This chamber was employed by Hagman in her Ph.D. work for TER-XSW experiments conducted at the 7-ID beamline.[126] The chamber used for the GISAXS experiments in this Ph.D. work involving *in situ* thermal and solvent annealing under a nitrogen or helium environment is part of the 8-ID beamline (see description in the last section).

5.3. Transmission Geometry

The x-ray investigation of soft materials in the transmission geometry[155] is undoubtedly mature with beamlines and instruments that are well-optimized for this purpose. While the work in this Ph.D. thesis does not directly involve any experiments performed in the transmission geometry, the Shull research group does frequently conduct small-angle x-ray scattering (SAXS) studies on block copolymers at the 5-ID beamline. For
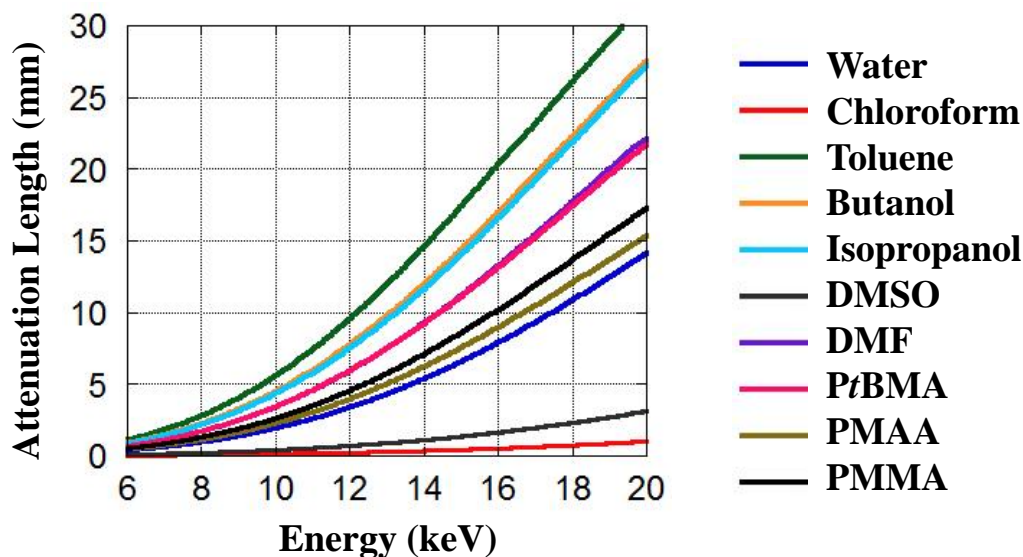
Figure 5.9. Plot of x-ray attenuation length versus energy for a variety of solvents and polymers.

specific details regarding sample preparation, SAXS parameters and measurements, and data analysis, the reader is asked to refer to the Ph.D. theses of Bras, Seitz, and Henderson.[156–158] Like in the GISAXS setup, a proper sample-to-detector distance must be chosen so that the corresponding q-range is appropriate for picking up the characteristic length scales present in the sample. In the past, a sample-to-detector distance of ∼4 m and an x-ray energy of 17 keV have been employed for examining systems containing block copolymer micelles in solution which exhibit length scales on the order of tens of nanometers. In principle, the higher the energy, the deeper the penetration of x-rays into the sample. Figure 5.9 shows a plot of the x-ray attenuation length versus energy for a variety of solvents and polymers.[132,133] Here, the x-ray attenuation length is defined as the depth into the sample where the intensity of the normal-incidence x-ray beam falls to $1/e$ of its initial value. Thus at 17 keV, standard capillary tubes ranging from 1.5 to

2 mm in diameter are, for the most part, reasonable for use in the SAXS measurements as the beam is not severely attenuated after transmission while sample preparation is still fairly manageable. The exceptions according to Figure 5.9 are systems that contain chloroform or dimethyl sulfoxide (DMSO), which absorb a large amount of x-rays even at high energies and consequently are not as ideal for x-ray scattering and imaging experiments as other solvents. Most importantly, contrast between constituents in the sample arising from differences in the attenuation length must be present in order for scattering to occur. A few percent contrast is usually sufficient, which is easily achievable in most samples. However, when mixing two solvents, one must be careful toward the possibility that the solvent mixture and polymer can end up with the same attenuation lengths, in which case the contrast disappears. X-ray imaging experiments performed, for instance, at the 32-ID beamline conform to the same contrast requirements. Additionally, objects of interest here must have length scales on the order of microns in order to be observed. Thus micellar aggregates in solution, as opposed to individual micelles, are appropriate candidates for this technique. Capillary tubes with a small diameter (< 1.5 mm) should be used to reduce the amount of material that the beam travels through, since everything in the line of sight of the x-rays is picked up and appears as a superposition in the image.

CHAPTER 6

Summary and Future Work

6.1. Summary

Polymer thin films have become an important part of industrial processes and are ubiquitous in our everyday lives. Nevertheless, we are undoubtedly still making new discoveries about their structure and behavior. In summary, this thesis explored through case studies two major topics that have always persisted in the science of polymer thin films. Chapter 3 investigated the problem of thermodynamic stability in homopolymer multilayer systems, a geometry that is becoming more mainstream in a variety of applications. It was shown that the dewetting behavior in a model homopolymer bilayer film, poly(4-bromostyrene)/poly(4-vinyl pyridine) (PBrS/P4VP), situated on top of a solid substrate was able to be tuned by systematically varying the thicknesses of the layers.[159] Specifically, a sufficiently thick PBrS layer was observed to undergo autophobic dewetting on top of the P4VP layer, which remained stable under all conditions. The results helped gain insight into the form and magnitude of the Helmholtz free energy, which is determined by a combination of long and short-range interactions among the different layers. These interactions were quantified with a host of experiments involving different techniques that looked into the characteristics of the dewetting patterns. Chapter 4 highlighted the fact that frequent challenges can be encountered during processing of block copolymer films, where the goal in many applications is to induce phase separation and

guide the self-assembly of well-ordered nanostructures. An amphiphilic diblock copolymer film, poly(methacrylic acid)-poly(methyl methacrylate) (PMAA-PMMA), was selected for this study because of difficulties in thermal annealing, due to its glass transition temperature being higher than its thermal degradation temperature, and in solvent annealing, due to a very limited selection of volatile solvents that can plasticize the polymer and induce mobility. A complex method involving reactive annealing was employed where a precursor poly(*tert*-butyl methacrylate)-poly(methyl methacrylate) (P*t*BMA-PMMA) film, after forming well-ordered nanostructures via solvent annealing at room temperature, was thermally converted to PMAA-PMMA. It was experimentally shown that the well-ordered morphologies were able to be maintained with a significant amount of conversion, though upon reaching full conversion, the system became kinetically frozen in a less ordered state. Chapter 5 provided a practical assessment of important characterization methods involving synchrotron radiation that can be used for the study of soft materials. Emphasis was placed on the techniques of x-ray standing waves generated via total external reflection from an x-ray mirror (TER-XSW) and grazing-incidence small-angle x-ray scattering (GISAXS), which were respectively applied in Chapters 3 and 4 for the investigation of polymer thin films. These techniques are expected to play an essential role in the evaluation of systems that are bound to become more and more complex in years to come.

6.2. Future Work

Stemming from the work in this Ph.D. thesis, there are a few possible follow-up experiments that can be pursued in the future. Additionally, there are a couple new projects
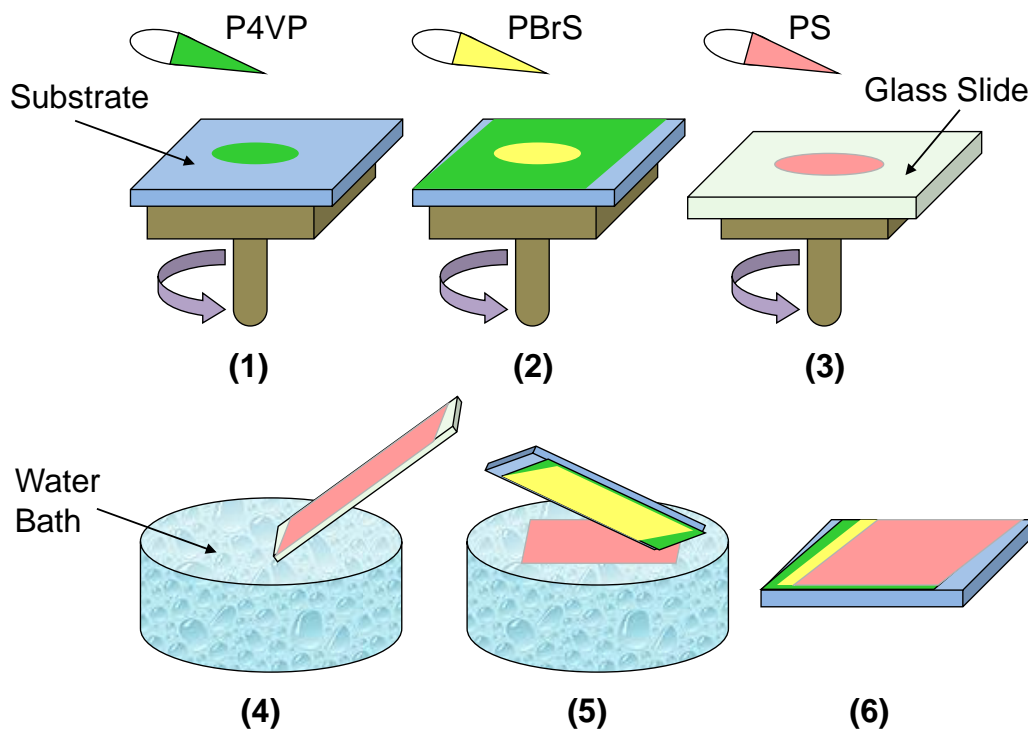
Figure 6.1. Illustration showing the sample preparation steps for creating the PS/PBrS/P4VP trilayer. The complete procedure is as follows: 1) Spin coat P4VP onto a solid substrate from butanol, 2) spin coat PBrS onto the P4VP from toluene, 3) spin coat PS onto a separate glass slide from toluene, 4) float the PS film off the glass slide onto a water surface, 5) carefully pick up the PS film with the sample, and 6) the finished sample is obtained.

involving synchrotron radiation that the Shull research group may embark on. The following paragraphs offer brief descriptions of these projects and are categorized by technique.

6.2.1. X-ray Standing Wave Experiments

Although Chapter 3 focused on the stability and dewetting behavior in the model homopolymer bilayer PBrS/P4VP, preliminary measurements were also performed on the trilayer poly(styrene)/poly(4-bromostyrene)/poly(4-vinyl pyridine) (PS/PBrS/P4VP). The PS layer (M_n = 131 kg/mol; M_w/M_n = 1.05) was easily added on top of the PBrS/P4VP

by either 1) spin coating onto a glass slide from a toluene solution, floating the film onto water, and picking it up with the sample (see Figure 6.1), or 2) direct spin coating from a cyclohexane solution, which is a nonsolvent for both PBrS and P4VP.[160] The top PS film added another level of complexity to the picture, both in terms of experimental analysis and theoretical predictions. Unlike the bilayer case where only the PBrS layer dewetted, both the PS and PBrS layers here were expected to dewet on top of the P4VP (as a side note, the geometry PS/PBrS itself has been shown to be more or less stable[161,162]). Over many trials, the observed behavior was not consistent possibly due to subtle variations in sample preparation. However, with extreme care and better sample preparation strategies to eliminate inherent defects and dust particles in the system, it should be feasible to conduct a thorough study as in Chapter 3 where the thicknesses of the layers are systematically varied and a free energy curve for the system is ultimately generated. Subsequently, it would be ideal to compare these results to that of the PBrS/P4VP bilayer and see how the extra PS layer tunes the overall stability of the system. The use of TER-XSW is crucial for these experiments since there are buried interfaces present.

Another potential future TER-XSW study intends to follow up on the work of Guico and Hagman[80,125,126] with more accurate measurements of the diffusion dynamics of short polymer chains within a higher-molecular weight polymer matrix. Previously, the diffusion behavior of polymer chains was assumed to be coupled to and quantified via the motion of a marker layer (e.g. gold nanoparticles) embedded within the sample.[80,163] However, as the next step, the ability to track the movement of the polymer chains themselves in a more direct manner should be pursued and is entirely feasible with TER-XSW. Related to the geometry above, the experiment can be conducted using a homopolymer
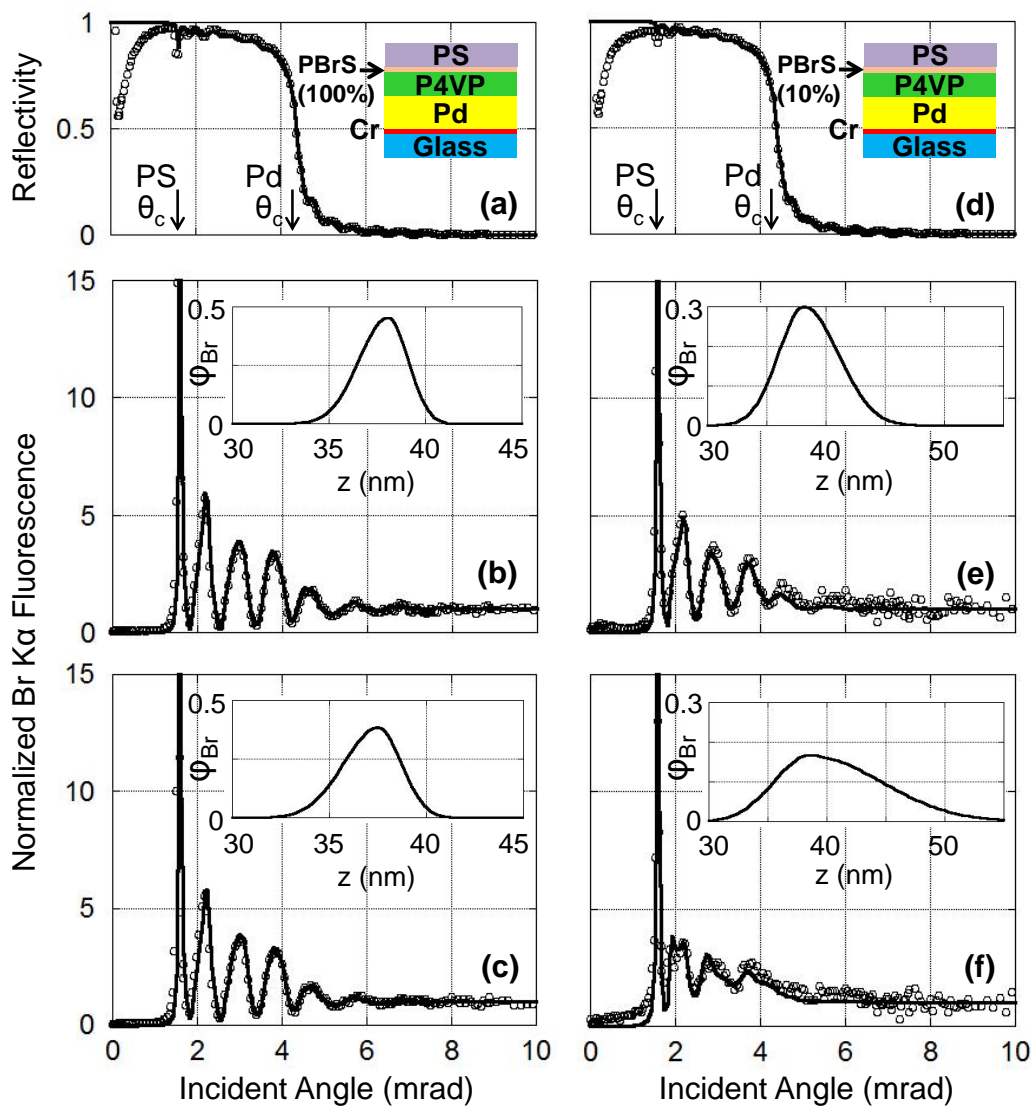
Figure 6.2. X-ray reflectivity and normalized bromine Kα fluorescence profiles for a PS/PBrS/P4VP sample prepared on top of an x-ray mirror comprising Pd, Cr, and glass (shown in schematic). Presented are data from a sample containing PBrS with 100% bromination after annealing at (a, b) 100 °C for an hour and (c) 145 °C for an hour, and from one containing PBrS with 10% bromination after annealing at (d, e) 100 °C for an hour and (f) 145 °C for an hour. The solid lines are fits to the experimental data points with the predicted bromine distributions (volume fractions) φ_{Br} shown in the insets.

trilayer sample with the middle polymer layer (e.g. PBrS) serving as the marker layer for fluorescence. It is obvious, however, that the PS/PBrS/P4VP system possesses some stability issues upon thermal annealing, and preliminary TER-XSW measurements were consequently not able to distinguish between diffusion and dewetting clearly when the changes in the marker distribution were analyzed. To conquer this problem, the model system should ideally contain polymer layers that are miscible with one another while the entire geometry should remain thermodynamically stable. This issue was partially solved by substituting the PBrS layer (where 100% of the repeat units were brominated) with one that was only 10% brominated (provided by the Genzer research group[164]), rendering the marker layer miscible with the PS layer on top.[165] However, the marker layer was still incompatible with the P4VP underneath, and dewetting was ultimately inevitable. The P4VP had to be kept as a spacer layer for TER-XSW (see Chapter 5) and was chosen for the ease of sample preparation. In any case, there was optimism that the diffusion in this system dominated the marker motion behavior early in the annealing process before any dewetting initiated. Figure 6.2 presents preliminary TER-XSW diffusion data from the PS/PBrS/P4VP trilayer for the cases of 10% and 100% PBrS bromination. After a gentle thermal annealing treatment without introducing dewetting (confirmed optically on the surface), the bromine distributions, given as a function of distance from the x-ray mirror z, show that there is clearly much more diffusion of the PBrS toward the top PS layer in the 10% brominated sample than in the 100% brominated one, as expected. More careful TER-XSW measurements should be done to quantify this diffusion behavior, particularly for the 10% brominated case, while avoiding instabilities from occurring anywhere in the sample. To this end, other characterization tools are likely needed to complement the

TER-XSW. An alternative system for studying diffusion may be one involving the polymer poly(tetramethyl bisphenol A polycarbonate) (TMPC)[166,167] with 10% brominated PBrS or poly(ethylene oxide) (PEO), as TMPC is known to be miscible with either PS or PEO. Measurements on TMPC/PBrS/P4VP samples were attempted with TER-XSW but, like with the PS/PBrS/P4VP system, further investigation is required due to the concern of subtle instabilities interfering with the data. The substitution of P4VP with another more compatible homopolymer (e.g. poly(2-vinyl pyridine) - P2VP) or even a block copolymer should hopefully eliminate this difficulty once and for all.

6.2.2. Grazing-Incidence Small-Angle X-ray Scattering Experiments

As a follow-up to the work in Chapter 4, it was mentioned in that chapter that the conversion of the PtBMA-PMMA precursor diblock copolymer film to PMAA-PMMA should be conducted via acid-catalyzed deprotection rather than thermal deprotection which may better preserve the well-ordered nanostructures achieved during solvent annealing in the first step. Once the setup, likely involving gaseous hydrochloric acid,[114,115] is established and tested, *in situ* and *ex situ* GISAXS measurements should be very straightforward to confirm this alternative annealing approach. After well-ordered morphologies can be obtained with full 100% conversion, the next step is to utilize these PMAA-PMMA nanostructures in experiments involving water. Here, the structural changes in this amphiphilic diblock film in response to pH and the introduction of ions, which are relevant in many industrial processes, are of great interest. In particular, the association of ions to the PMAA polyelectrolyte block has the potential to induce major changes in the morphology and arrangement of the microdomains as well as the mechanical properties of the film

controlled by ionic crosslinking. Such a system would essentially be a two-dimensional analog of the three-dimensional hydrogel system investigated by Henderson *et al.*[93] Along the way, however, GISAXS studies may present challenges if a characteristic length scale associated with the ordering of the microdomains is not maintained during the course of the incubation process (i.e. the structural changes are not homogeneous). The incubation procedure itself may likely require extensive adjustments to induce the desired effects in the sample. Therefore, multiple experiments involving atomic force microscopy (AFM) conducted with samples in a liquid environment are essential prior to performing any GISAXS measurements at the APS.

Finally, a separate project that interests the Shull research group involves probing using GISAXS the structural changes within a drop of block copolymer solution on a solid substrate during the course of its evaporation. The geometry of this system mirrors a similar one investigated in the past involving gold nanoparticles suspended in toluene which form two-dimensional nanocrystal superlattices upon evaporation.[168–170] The phenomenon relies on self-assembly at the air/liquid interface before the drop completely dries. To this end, the system should ideally contain surface-active species that spontaneously migrate to the interface. The solvent chosen and its evaporation rate are also crucial factors that affect the final morphology and quality of the ordering obtained. Thus, preliminary testing should be conducted with AFM and other imaging techniques prior to performing *in situ* GISAXS experiments. The procedure for collecting GISAXS data is somewhat different from the traditional method involving thin films. Initially, when the drop is present on top of the substrate, a transmission geometry (SAXS) may be used to look at the vicinity of the air/liquid interface. Toward the end of the evaporation process,

the familiar reflection geometry is adopted as the structure of interest rests directly on top of the substrate surface. This project takes full advantage of the real-time, *in situ* capabilities at the 8-ID beamline, which provides access to structural information that is difficult to acquire through other means.

References

[1] K. Jacobs, R. Seemann, and S. Herminghaus. Stability and dewetting of thin liquid films. In O. K. C. Tsui and T. P. Russell, editors, *Series in Soft Condensed Matter Vol. 1: Polymer Thin Films*, pages 243–265. World Scientific, Singapore, 2008.

[2] K. R. Shull. Wetting autophobicity of polymer melts. *Faraday Discussions*, 98(98):203–217, 1994.

[3] F. Brochard-Wyart, J.-M. di Meglio, D. Quere, and P.-G. de Gennes. Spreading of nonvolatile liquids in a continuum picture. *Langmuir*, 7(2):335–338, 1991.

[4] J. Becker, G. Grün, R. Seemann, H. Mantz, K. Jacobs, K. R. Mecke, and R. Blossey. Complex dewetting scenarios captured by thin-film models. *Nature Materials*, 2(1):59–63, 2003.

[5] R. Fetzer, M. Rauscher, R. Seemann, K. Jacobs, and K. Mecke. Thermal noise influences fluid flow in thin films during spinodal dewetting. *Physical Review Letters*, 99(11):114503, 2007.

[6] R. Xie, A. Karim, J. F. Douglas, C. C. Han, and R. A. Weiss. Spinodal dewetting of thin polymer films. *Physical Review Letters*, 81(6):1251–1254, 1998.

[7] J. C. Meredith, A. P. Smith, A. Karim, and E. J. Amis. Combinatorial materials science for polymer thin-film dewetting. *Macromolecules*, 33(26):9747–9756, 2000.

[8] C. Neto and K. Jacobs. Dynamics of hole growth in dewetting polystyrene films. *Physica A-Statistical Mechanics and Its Applications*, 339(1-2):66–71, 2004.

[9] R. Seemann, S. Herminghaus, and K. Jacobs. Shape of a liquid front upon dewetting. *Physical Review Letters*, 87(19):196101, 2001.

[10] R. Seemann, S. Herminghaus, and K. Jacobs. Gaining control of pattern formation of dewetting liquid films. *Journal of Physics-Condensed Matter*, 13(21):4925–4938, 2001.

[11] J.-L. Masson and P. F. Green. Hole formation in thin polymer films: a two-stage process. *Physical Review Letters*, 88(20):205504, 2002.

[12] M. Stamm. Polymer surface and interface characterization techniques. In M. Stamm, editor, *Polymer Surfaces and Interfaces*, pages 1–16. Springer Berlin Heidelberg, 2008.

[13] P. Müller-Buschbaum. Dewetting and pattern formation in thin polymer films as investigated in real and reciprocal space. *Journal of Physics-Condensed Matter*, 15(36):R1549–R1582, 2003.

[14] P. Müller-Buschbaum. Grazing incidence small-angle x-ray scattering: an advanced scattering technique for the investigation of nanostructured polymer films. *Analytical and Bioanalytical Chemistry*, 376(1):3–10, 2003.

[15] P. Müller-Buschbaum. High-resolution grazing incidence small angle x-ray scattering: Investigation of micrometer sized structured polymer films. *Characterization of Polymer Surfaces and Thin Films*, 132:23–32 171, 2006.

[16] X. S. Hu, X. S. Jiao, S. Narayanan, Z. Jiang, S. K. Sinha, L. B. Lurio, and J. Lal. Resonantly enhanced off-specular x-ray scattering from polymer/polymer interfaces. *European Physical Journal E*, 17(3):353–359, 2005.

[17] M. Tolan, O. H. Seeck, J. P. Schlomka, W. Press, J. Wang, S. K. Sinha, Z. Li, M. H. Rafailovich, and J. Sokolov. Evidence for capillary waves on dewetted polymer film surfaces: A combined x-ray and atomic force microscopy study. *Physical Review Letters*, 81(13):2731–2734, 1998.

[18] J. Wang, M. Tolan, O. H. Seeck, S. K. Sinha, O. Bahr, M. H. Rafailovich, and J. Sokolov. Surfaces of strongly confined polymer thin films studied by x-ray scattering. *Physical Review Letters*, 83(3):564–567, 1999.

[19] P. Müller-Buschbaum and M. Stamm. Correlated roughness, long-range correlations, and dewetting of thin polymer films. *Macromolecules*, 31(11):3686–3692, 1998.

[20] P. Müller-Buschbaum and M. Stamm. Dewetting of thin polymer films: an x-ray scattering study. *Physica B*, 248:229–237, 1998.

[21] P. Müller-Buschbaum, J. S. Gutmann, C. Lorenz-Haas, O. Wunnicke, M. Stamm, and W. Petry. Dewetting of thin diblock copolymer films: Spinodal dewetting kinetics. *Macromolecules*, 35(6):2017–2023, 2002.

[22] M. Sferrazza, M. Heppenstall-Butler, R. Cubitt, D. Bucknall, J. Webster, and R. A. L. Jones. Interfacial instability driven by dispersive forces: The early stages of spinodal dewetting of a thin polymer film on a polymer substrate. *Physical Review Letters*, 81(23):5173–5176, 1998.

[23] C. Carelli, A. M. Higgins, R. A. L. Jones, and M. Sferrazza. Early-stage roughening of the polymer-polymer interface approaching the glass transition temperature by real-time neutron reflection. *Physical Review E*, 73(6), 2006.

[24] A. M. Higgins, M. Sferrazza, R. A. L. Jones, P. C. Jukes, J. S. Sharp, L. E. Dryden, and J. Webster. The timescale of spinodal dewetting at a polymer/polymer interface. *European Physical Journal E*, 8(2):137–143, 2002.

[25] A. P. Marencic and R. A. Register. Controlling order in block copolymer thin films for nanopatterning applications. *Annual Review of Chemical and Biomolecular Engineering, Vol 1*, 1:277–297, 2010.

[26] J. N. L. Albert and T. H. Epps. Self-assembly of block copolymer thin films. *Materials Today*, 13(6):24–33, 2010.

[27] J. L. Zhang, X. H. Yu, P. Yang, J. Peng, C. X. Luo, W. H. Huang, and Y. C. Han. Microphase separation of block copolymer thin films. *Macromolecular Rapid Communications*, 31(7):591–608, 2010.

[28] V. Abetz and P. F. W. Simon. Phase behaviour and morphologies of block copolymers. *Block Copolymers I*, 189:125–212, 2005.

[29] M. Q. Li and C. K. Ober. Block copolymer patterns and templates. *Materials Today*, 9(9):30–39, 2006.

[30] M. W. Matsen and F. S. Bates. Unifying weak- and strong-segregation block copolymer theories. *Macromolecules*, 29(4):1091–1098, 1996.

[31] D. G. Bucknall. Influence of interfaces on thin polymer film behaviour. *Progress in Materials Science*, 49(5):713–786, 2004.

[32] P. Busch and R. Weidisch. Interfaces between incompatible polymers. In M. Stamm, editor, *Polymer Surfaces and Interfaces*, pages 161–182. Springer Berlin Heidelberg, 2008.

[33] P. J. Flory. Thermodynamics of high polymer solutions. *Journal of Chemical Physics*, 10:51–61, 1942.

[34] E. Helfand. Theory of inhomogeneous polymers - fundamentals of Gaussian random-walk model. *Journal of Chemical Physics*, 62(3):999–1005, 1975.

[35] K. R. Shull. Mean-field theory of block copolymers - bulk melts, surfaces, and thin-films. *Macromolecules*, 25(8):2122–2133, 1992.

[36] R. E. Bras and K. R. Shull. Self-consistent field theory of gelation in triblock copolymer solutions. *Macromolecules*, 42(21):8513–8520, 2009.

[37] M. W. Matsen. *Self-Consistent Field Theory and Its Applications*. Soft Matter. Wiley-VCH Verlag GmbH & Co. KGaA, 2007.

[38] T. L. Morkved, M. Lu, A. M. Urbas, E. E. Ehrichs, H. M. Jaeger, P. Mansky, and T. P. Russell. Local control of microdomain orientation in diblock copolymer thin films with electric fields. *Science*, 273(5277):931–933, 1996.

[39] S. Elhadj, J. W. Woody, V. S. Niu, and R. F. Saraf. Orientation of self-assembled block copolymer cylinders perpendicular to electric field in mesoscale film. *Applied Physics Letters*, 82(6):871–873, 2003.

[40] C. Y. Chao, X. F. Li, C. K. Ober, C. Osuji, and E. L. Thomas. Orientational switching of mesogens and microdomains in hydrogen-bonded side-chain liquid-crystalline block copolymers using AC electric fields. *Advanced Functional Materials*, 14(4):364–370, 2004.

[41] J. Bodycomb, Y. Funaki, K. Kimishima, and T. Hashimoto. Single-grain lamellar microdomain from a diblock copolymer. *Macromolecules*, 32(6):2075–2077, 1999.

[42] S. O. Kim, H. H. Solak, M. P. Stoykovich, N. J. Ferrier, J. J. de Pablo, and P. F. Nealey. Epitaxial self-assembly of block copolymers on lithographically defined nanopatterned substrates. *Nature*, 424(6947):411–414, 2003.

[43] G. S. W. Craig, H. Kang, and P. F. Nealey. Equilibration of block copolymer films on chemically patterned surfaces. In O. K. C. Tsui and T. P. Russell, editors, *Series in Soft Condensed Matter Vol. 1: Polymer Thin Films*, pages 27–52. World Scientific, Singapore, 2008.

[44] S. Park, D. H. Lee, J. Xu, B. Kim, S. W. Hong, U. Jeong, T. Xu, and T. P. Russell. Macroscopic 10-terabit-per-square- inch arrays from block copolymers with lateral order. *Science*, 323(5917):1030–1033, 2009.

[45] T. P. Russell, G. Coulon, V. R. Deline, and D. C. Miller. Characteristics of the surface-induced orientation for symmetric diblock PS/PMMA copolymers. *Macromolecules*, 22(12):4600–4606, 1989.

[46] J.-Y. Wang, S. Park, and T. P. Russell. Block copolymer thin films. In O. K. C. Tsui and T. P. Russell, editors, *Series in Soft Condensed Matter Vol. 1: Polymer Thin Films*, pages 1–25. World Scientific, Singapore, 2008.

[47] M. Cavallini. Inhomogeneous thin deposits: a strategy to exploit their functionality. *Journal of Materials Chemistry*, 19(34):6085–6092, 2009.

[48] A. Calo, P. Stoliar, F. C. Matacotta, M. Cavallini, and F. Biscarini. Time-temperature integrator based on the dewetting of polyisobutylene thin films. *Langmuir*, 26(8):5312–5315, 2010.

[49] A. Vrij. Possible mechanism for spontaneous rupture of thin free liquid films. *Discussions of the Faraday Society*, 42(42):23, 1966.

[50] E. Ruckenstein and R. K. Jain. Spontaneous rupture of thin liquid-films. *Journal of the Chemical Society-Faraday Transactions II*, 70:132–147, 1974.

[51] P. G. de Gennes. Wetting - statics and dynamics. *Reviews of Modern Physics*, 57(3):827–863, 1985.

[52] V. S. Mitlin. Dewetting of solid-surface - analogy with spinodal decomposition. *Journal of Colloid and Interface Science*, 156(2):491–497, 1993.

[53] V. M. Starov. Equilibrium and hysteresis contact angles. *Advances in Colloid and Interface Science*, 39:147–173, 1992.

[54] A. Sharma. Equilibrium contact angles and film thicknesses in the apolar and polar systems - role of intermolecular interactions in coexistence of drops with thin-films. *Langmuir*, 9(12):3580–3586, 1993.

[55] G. Reiter. Dewetting of thin polymer-films. *Physical Review Letters*, 68(1):75–78, 1992.

[56] M. Geoghegan and G. Krausch. Wetting at polymer surfaces and interfaces. *Progress in Polymer Science*, 28(2):261–302, 2003.

[57] R. V. Craster and O. K. Matar. Dynamics and stability of thin liquid films. *Reviews of Modern Physics*, 81(3):1131–1198, 2009.

[58] D. Bonn, J. Eggers, J. Indekeu, J. Meunier, and E. Rolley. Wetting and spreading. *Reviews of Modern Physics*, 81(2):739–805, 2009.

[59] R. Seemann, S. Herminghaus, C. Neto, S. Schlagowski, D. Podzimek, R. Konrad, H. Mantz, and K. Jacobs. Dynamics and structure formation in thin polymer melt films. *Journal of Physics-Condensed Matter*, 17(9):S267–S290, 2005.

[60] A. Sharma and R. Khanna. Pattern formation in unstable thin liquid films. *Physical Review Letters*, 81(16):3463–3466, 1998.

[61] A. Sharma and R. Khanna. Pattern formation in unstable thin liquid films under the influence of antagonistic short- and long-range forces. *Journal of Chemical Physics*, 110(10):4929–4936, 1999.

[62] G. Reiter, A. Sharma, A. Casoli, M. O. David, R. Khanna, and P. Auroy. Thin film instability induced by long-range forces. *Langmuir*, 15(7):2551–2558, 1999.

[63] L. Xu, T. F. Shi, and L. J. An. The competition between the liquid-liquid dewetting and the liquid-solid dewetting. *Journal of Chemical Physics*, 130(18):184903, 2009.

[64] J. P. de Silva, S. J. Martin, R. Cubitt, and M. Geoghegan. Observation of the complete rupture of a buried polymer layer by off-specular neutron reflectometry. *EPL*, 86(3):36005, 2009.

[65] J. P. de Silva, M. Geoghegan, A. M. Higgins, G. Krausch, M. O. David, and G. Reiter. Switching layer stability in a polymer bilayer by thickness variation. *Physical Review Letters*, 98(26):267802, 2007.

[66] D. Bandyopadhyay and A. Sharma. Dewetting pathways and morphology of unstable thin liquid bilayers. *Journal of Physical Chemistry B*, 112(37):11564–11572, 2008.

[67] A. Pototsky, M. Bestehorn, D. Merkt, and U. Thiele. Alternative pathways of dewetting for a thin liquid two-layer film. *Physical Review E*, 70(2):025201, 2004.

[68] A. Pototsky, M. Bestehorn, D. Merkt, and U. Thiele. Morphology changes in the evolution of liquid two-layer films. *Journal of Chemical Physics*, 122(22):224711, 2005.

[69] A. Pototsky, M. Bestehorn, D. Merkt, and U. Thiele. Evolution of interface patterns of three-dimensional two-layer liquid films. *Europhysics Letters*, 74(4):665–671, 2006.

[70] L. S. Fisher and A. A. Golovin. Nonlinear stability analysis of a two-layer thin liquid film: Dewetting and autophobic behavior. *Journal of Colloid and Interface Science*, 291(2):515–528, 2005.

[71] P. Müller-Buschbaum, O. Wunnicke, M. Stamm, Y. C. Lin, and M. Müller. Stability-instability transition by tuning the effective interface potential in polymeric bilayer films. *Macromolecules*, 38(8):3406–3413, 2005.

[72] C. J. Clarke, A. Eisenberg, J. LaScala, M. H. Rafailovich, J. Sokolov, Z. Li, S. Qu, D. Nguyen, S. A. Schwarz, Y. Strzhemechny, and B. B. Sauer. Measurements of the Flory-Huggins interaction parameter for polystyrene-poly(4-vinylpyridine) blends. *Macromolecules*, 30(14):4184–4188, 1997.

[73] D. Slep, J. Asselta, M. H. Rafailovich, J. Sokolov, D. A. Winesett, A. P. Smith, H. Ade, Y. Strzhemechny, S. A. Schwarz, and B. B. Sauer. Phase separation of polystyrene and bromo-polystyrene mixtures in equilibrium structures in thin films. *Langmuir*, 14(17):4860–4864, 1998.

[74] D. Slep, J. Asselta, M. H. Rafailovich, J. Sokolov, D. A. Winesett, A. P. Smith, H. Ade, and S. Anders. Effect of an interactive surface on the equilibrium contact angles in bilayer polymer films. *Langmuir*, 16(5):2369–2375, 2000.

[75] B. H. Sohn, B. W. Seo, S. I. Yoo, and W. C. Zin. Sluggish development of parallel lamellae at the strongly interacting interface in thin films of symmetric diblock copolymers. *Langmuir*, 18(26):10505–10508, 2002.

[76] K. R. Shull and A. J. Kellock. Metal-particle adsorption and diffusion in a model polymer/metal composite system. *Journal of Polymer Science Part B-Polymer Physics*, 33(9):1417–1422, 1995.

[77] M. J. Bedzyk, G. M. Bommarito, and J. S. Schildkraut. X-ray standing waves at a reflecting mirror surface. *Physical Review Letters*, 62(12):1376–1379, 1989.

[78] J. Wang, M. J. Bedzyk, T. L. Penner, and M. Caffrey. Structural studies of membranes and surface layers up to 1,000 Å thick using x-ray standing waves. *Nature*, 354(6352):377–380, 1991.

[79] J. Wang, M. Caffrey, M. J. Bedzyk, and T. L. Penner. Structure changes in model membranes monitored by variable period x-ray standing waves - effect of Langmuir-Blodgett-film thickness on thermal-behavior. *Journal of Physical Chemistry*, 98(42):10957–10968, 1994.

[80] R. S. Guico, S. Narayanan, J. Wang, and K. R. Shull. Dynamics of polymer/metal nanocomposite films at short times as studied by x-ray standing waves. *Macromolecules*, 37(22):8357–8363, 2004.

[81] L. G. Parratt. Surface studies of solids by total reflection of x-rays. *Physical Review*, 95(2):359–369, 1954.

[82] R. Seemann, S. Herminghaus, and K. Jacobs. Dewetting patterns and molecular forces: A reconciliation. *Physical Review Letters*, 86(24):5534–5537, 2001.

[83] J. N. Israelachvili. *Intermolecular and Surface Forces*. Academic Press, London, 2nd edition, 1992.

[84] E. Vitt and K. R. Shull. Equilibrium contact-angle for polymer/polymer interfaces. *Macromolecules*, 28(18):6349–6353, 1995.

[85] M. Lazzari and M. A. Lopez-Quintela. Block copolymers as a tool for nanomaterial fabrication. *Advanced Materials*, 15(19):1583–1594, 2003.

[86] C. Park, J. Yoon, and E. L. Thomas. Enabling nanotechnology with self assembled block copolymer patterns. *Polymer*, 44(22):6725–6760, 2003.

[87] R. A. Segalman. Patterning with block copolymer thin films. *Materials Science & Engineering R-Reports*, 48(6):191–226, 2005.

[88] I. W. Hamley. Ordering in thin films of block copolymers: Fundamentals to potential applications. *Progress in Polymer Science*, 34(11):1161–1210, 2009.

[89] M. Bohme, B. Kuila, H. Schlorb, B. Nandan, and M. Stamm. Thin films of block copolymer supramolecular assemblies: Microphase separation and nanofabrication. *Physica Status Solidi B-Basic Solid State Physics*, 247(10):2458–2469, 2010.

[90] M. Y. Paik, J. K. Bosworth, D. M. Smilges, E. L. Schwartz, X. Andre, and C. K. Ober. Reversible morphology control in block copolymer films via solvent vapor processing: An in situ GISAXS study. *Macromolecules*, 43(9):4253–4260, 2010.

[91] S. Krishnamoorthy, C. Hinderling, and H. Heinzelmann. Nanoscale patterning with block copolymers. *Materials Today*, 9(9):40–47, 2006.

[92] M. Guvendiren and K. R. Shull. Self-assembly of acrylic triblock hydrogels by vapor-phase solvent exchange. *Soft Matter*, 3(5):619–626, 2007.

[93] K. J. Henderson, T. C. Zhou, K. J. Otim, and K. R. Shull. Ionically cross-linked triblock copolymer hydrogels with high strength. *Macromolecules*, 43(14):6193–6201, 2010.

[94] T. Xu, J. T. Goldbach, M. J. Misner, S. Kim, A. Gibaud, O. Gang, B. Ocko, K. W. Guarini, C. T. Black, C. J. Hawker, and T. P. Russell. Scattering study on the selective solvent swelling induced surface reconstruction. *Macromolecules*, 37(8):2972–2977, 2004.

[95] D. Y. Ryu, S. Ham, E. Kim, U. Jeong, C. J. Hawker, and T. P. Russell. Cylindrical microdomain orientation of PS-b-PMMA on the balanced interfacial interactions: Composition effect of block copolymers. *Macromolecules*, 42(13):4902–4906, 2009.

[96] I. A. Zucchi, E. Poliani, and M. Perego. Microdomain orientation dependence on thickness in thin films of cylinder-forming PS-b-PMMA. *Nanotechnology*, 21(18):185304, 2010.

[97] X. H. Zhang, K. G. Yager, N. J. Fredin, H. W. Ro, R. L. Jones, A. Karim, and J. F. Douglas. Thermally reversible surface morphology transition in thin diblock copolymer films. *ACS Nano*, 4(7):3653–3660, 2010.

[98] L. F. Zhang and A. Eisenberg. Multiple morphologies of crew-cut aggregates of polystyrene-b-poly(acrylic acid) block-copolymers. *Science*, 268(5218):1728–1731, 1995.

[99] Y. Boontongkong and R. E. Cohen. Cavitated block copolymer micellar thin films: Lateral arrays of open nanoreactors. *Macromolecules*, 35(9):3647–3652, 2002.

[100] Y. H. La, E. W. Edwards, S. M. Park, and P. F. Nealey. Directed assembly of cylinder-forming block copolymer films and thermochemically induced cylinder to sphere transition: A hierarchical route to linear arrays of nanodots. *Nano Letters*, 5(7):1379–1384, 2005.

[101] C. Xu, X. F. Fu, M. Fryd, S. Xu, B. B. Wayland, K. I. Winey, and R. J. Composto. Reversible stimuli-responsive nanostructures assembled from amphiphilic block copolymers. *Nano Letters*, 6(2):282–287, 2006.

[102] C. Xu, B. B. Wayland, M. Fryd, K. I. Winey, and R. J. Composto. pH-responsive nanostructures assembled from amphiphilic block copolymers. *Macromolecules*, 39(18):6063–6070, 2006.

[103] D. H. Park. A new process for fabricating nanodot arrays on selective regions with diblock copolymer thin film. *Nanotechnology*, 18(36):–, 2007.

[104] G. Wallraff, J. Hutchinson, W. Hinsberg, F. Houle, P. Seidel, R. Johnson, and W. Oldham. Thermal and acid-catalyzed deprotection kinetics in candidate deep-ultraviolet resist materials. *Journal of Vacuum Science & Technology B*, 12(6):3857–3862, 1994.

[105] S. Ludwigs, A. Boker, A. Voronov, N. Rehse, R. Magerle, and G. Krausch. Self-assembly of functional nanostructures from ABC triblock copolymers. *Nature Materials*, 2(11):744–747, 2003.

[106] A. C. Miller, R. D. Bennett, P. T. Hammond, D. J. Irvine, and R. E. Cohen. Functional nanocavity arrays via amphiphilic block copolymer thin films. *Macromolecules*, 41(5):1739–1744, 2008.

[107] A. J. Jang, S. K. Lee, and S. H. Kim. Structure and phase transition in thin films of block copolymer micelles complexed with inorganic precursors. *Polymer*, 51(15):3486–3492, 2010.

[108] S. M. Kim, S. J. Ku, and J. B. Kim. SiO_2 nanodot arrays using functionalized block copolymer templates and selective silylation. *Nanotechnology*, 21(23):235302, 2010.

[109] D. H. Cole, K. R. Shull, P. Baldo, and L. Rehn. Dynamic properties of a model polymer/metal nanocomposite: Gold particles in poly(tert-butyl acrylate). *Macromolecules*, 32(3):771–779, 1999.

[110] J. J. Maurer, D. J. Eustace, and C. T. Ratcliffe. Thermal characterization of poly(acrylic acid). *Macromolecules*, 20(1):196–202, 1987.

[111] H. Yang and J. S. Sharp. Interfacial effects and the glass transition in ultrathin films of poly(tert-butyl methacrylate). *Macromolecules*, 41(13):4811–4816, 2008.

[112] J. H. Lai. Thermal-behavior of random copolymers of methacrylic-acid and tert-butyl methacrylate. *Macromolecules*, 17(5):1010–1012, 1984.

[113] D. H. Grant and N. Grassie. The thermal decomposition of poly(t-butyl-methacrylate). *Polymer*, 1(4):445–455, 1960.

[114] A. R. Esker, C. Mengel, and G. Wegner. Ultrathin films of a polyelectrolyte with layered architecture. *Science*, 280(5365):892–895, 1998.

[115] C. Mengel, A. R. Esker, W. H. Meyer, and G. Wegner. Preparation and modification of poly(methacrylic acid) and poly(acrylic acid) multilayers. *Langmuir*, 18(16):6365–6372, 2002.

[116] P. L. Drzal and K. R. Shull. Origins of mechanical strength and elasticity in thermally reversible, acrylic triblock copolymer gels. *Macromolecules*, 36(6):2000–2008, 2003.

[117] M. E. Seitz, W. R. Burghardt, K. T. Faber, and K. R. Shull. Self-assembly and stress relaxation in acrylic triblock copolymer gels. *Macromolecules*, 40(4):1218–1226, 2007.

[118] G. E. Stein, E. J. Kramer, X. F. Li, and J. Wang. Layering transitions in thin films of spherical-domain block copolymers. *Macromolecules*, 40(7):2453–2460, 2007.

[119] S. K. Sinha, E. B. Sirota, S. Garoff, and H. B. Stanley. X-ray and neutron-scattering from rough surfaces. *Physical Review B*, 38(4):2297–2311, 1988.

[120] M. Rauscher, T. Salditt, and H. Spohn. Small-angle x-ray scattering under grazing incidence: The cross section in the distorted-wave Born approximation. *Physical Review B*, 52(23):16855–16863, 1995.

[121] B. Lee, I. Park, J. Yoon, S. Park, J. Kim, K. W. Kim, T. Chang, and M. Ree. Structural analysis of block copolymer thin films with grazing incidence small-angle x-ray scattering. *Macromolecules*, 38(10):4311–4323, 2005.

[122] P. Busch, M. Rauscher, D. M. Smilgies, D. Posselt, and C. M. Papadakis. Grazing-incidence small-angle x-ray scattering from thin polymer films with lamellar structures-the scattering cross section in the distorted-wave Born approximation. *Journal of Applied Crystallography*, 39:433–442, 2006.

[123] D. L. Bunker, B. Garrett, T. Kleindienst, and G. S. Long. Discrete simulation methods in combustion kinetics. *Combustion and Flame*, 23(3):373–379, 1974.

[124] D. T. Gillespie. General method for numerically simulating stochastic time evolution of coupled chemical-reactions. *Journal of Computational Physics*, 22(4):403–434, 1976.

[125] R. S. Guico. *Studies of the Mobility and Organization of Gold Nanoparticles in Polymeric Ultrathin Films by X-ray Scattering and Fluorescence*. PhD thesis, Northwestern University, 2003.

[126] A. L. Hagman. *Studies of Nanoparticle Marker Motion in Ultra Thin Polymer Films With X-ray Standing Waves*. PhD thesis, Northwestern University, 2007.

[127] B. Lin, T. L. Morkved, M. Meron, Z. Huang, P. J. Viccaro, H. M. Jaeger, S. M. Williams, and M. L. Schlossman. X-ray studies of polymer/gold nanocomposites.

Journal of Applied Physics, 85(6):3180–3184, 1999.

[128] J. Wang, M. Caffrey, M. J. Bedzyk, and T. L. Penner. Direct profiling and reversibility of ion distribution at a charged membrane/aqueous interface: An x-ray standing wave study. *Langmuir*, 17(12):3671–3681, 2001.

[129] J. Wang. *X-ray Standing Waves and Their Use in Characterizing Biologically Relevant Thin Film Systems*. PhD thesis, The Ohio State University, 1994.

[130] A. G. Richter, R. S. Guico, K. R. Shull, and J. Wang. Thickness and interfacial roughness changes in polymer thin films during x-irradiation. *Macromolecules*, 39(4):1545–1553, 2006.

[131] E. Karapetrova, G. Ice, J. Tischler, H. Hong, and P. Zschack. Design and performance of the 33-BM beamline at the Advanced Photon Source. *Nuclear Instruments and Methods in Physics Research Section A: Accelerators, Spectrometers, Detectors and Associated Equipment*, In Press, Corrected Proof, 2011.

[132] E. M. Gullikson. CXRO x-ray interactions with matter. `http://henke.lbl.gov/optical_constants/`, April 2011.

[133] B. L. Henke, E. M. Gullikson, and J. C. Davis. X-ray interactions - photoabsorption, scattering, transmission, and reflection at E=50-30,000 Ev, Z=1-92. *Atomic Data and Nuclear Data Tables*, 54(2):181–342, 1993.

[134] D. A. Walko, D. A. Arms, and E. C. Landahl. Empirical dead-time corrections for synchrotron sources. *Journal of Synchrotron Radiation*, 15:612–617, 2008.

[135] J. R. Levine, J. B. Cohen, Y. W. Chung, and P. Georgopoulos. Grazing-incidence small-angle x-ray-scattering - new tool for studying thin-film growth. *Journal of Applied Crystallography*, 22:528–532, 1989.

[136] A. Naudon, T. Slimani, and P. Goudeau. Grazing small-angle scattering of x-rays for the study of thin surface-layers. *Journal of Applied Crystallography*, 24:501–508, 1991.

[137] S. Narayanan, D. R. Lee, R. S. Guico, S. K. Sinha, and J. Wang. Real-time evolution of the distribution of nanoparticles in an ultrathin-polymer-film-based waveguide. *Physical Review Letters*, 94(14):145504, 2005.

[138] J. Wang, M. J. Bedzyk, and M. Caffrey. Resonance-enhanced x-rays in thin-films - a structure probe for membranes and surface-layers. *Science*, 258(5083):775–778, 1992.

[139] D. R. Lee, A. Hagman, X. F. Li, S. Narayanan, J. Wang, and K. R. Shull. Perturbation to the resonance modes by gold nanoparticles in a thin-film-based x-ray waveguide. *Applied Physics Letters*, 88(15):153101, 2006.

[140] Z. Y. Di, D. Posselt, D. M. Smilgies, and C. M. Papadakis. Structural rearrangements in a lamellar diblock copolymer thin film during treatment with saturated solvent vapor. *Macromolecules*, 43(1):418–427, 2010.

[141] J. Jung, H. W. Park, S. Lee, H. Lee, T. Chang, K. Matsunaga, and H. Jinnai. Effect of film thickness on the phase behaviors of diblock copolymer thin film. *ACS Nano*, 4(6):3109–3116, 2010.

[142] I. Park, B. Lee, J. Ryu, K. Im, J. Yoon, M. Ree, and T. Chang. Epitaxial phase transition of polystyrene-b-polyisoprene from hexagonally perforated layer to gyroid phase in thin film. *Macromolecules*, 38(25):10532–10536, 2005.

[143] S. Park, B. Kim, J. Xu, T. Hofmann, B. M. Ocko, and T. P. Russell. Lateral ordering of cylindrical microdomains under solvent vapor. *Macromolecules*, 42(4):1278–1284, 2009.

[144] S. H. Kim, M. J. Misner, and T. P. Russell. Controlling orientation and order in block copolymer thin films. *Advanced Materials*, 20(24):4851–4856, 2008.

[145] P. Müller-Buschbaum. Structure determination in thin film geometry using grazing incidence small-angle scattering. In M. Stamm, editor, *Polymer Surfaces and Interfaces*, pages 17–46. Springer Berlin Heidelberg, 2008.

[146] P. Müller-Buschbaum. A basic introduction to grazing incidence small-angle x-ray scattering. In M. Gomez, A. Nogales, M. C. Garcia-Gutierrez, and T. A. Ezquerra, editors, *Applications of Synchrotron Light to Scattering and Diffraction in Materials and Life Sciences*, volume 776 of *Lecture Notes in Physics*, pages 61–89. Springer Berlin / Heidelberg, 2009.

[147] A. Meyer. Grazing incidence x-ray scattering. `http://www.gisaxs.de/`, April 2011.

[148] M. P. Tate, V. N. Urade, J. D. Kowalski, T. C. Wei, B. D. Hamilton, B. W. Eggiman, and H. W. Hillhouse. Simulation and interpretation of 2D diffraction patterns from self-assembled nanostructured films at arbitrary angles of incidence: From grazing incidence (above the critical angle) to transmission perpendicular to the substrate. *Journal of Physical Chemistry B*, 110(20):9882–9892, 2006.

[149] M. P. Tate and H. W. Hillhouse. General method for simulation of 2D GISAXS intensities for any nanostructured film using discrete Fourier transforms. *Journal of*

Physical Chemistry C, 111(21):7645–7654, 2007.

[150] B. W. Eggiman, M. P. Tate, and H. W. Hillhouse. Rhombohedral structure of highly ordered and oriented self-assembled nanoporous silica thin films. *Chemistry of Materials*, 18(3):723–730, 2006.

[151] D. Babonneau. FitGISAXS: software package for modelling and analysis of GISAXS data using IGOR Pro. *Journal of Applied Crystallography*, 43:929–936, 2010.

[152] R. Lazzari. IsGISAXS: a program for grazing-incidence small-angle x-ray scattering analysis of supported islands. *Journal of Applied Crystallography*, 35:406–421, 2002.

[153] X. F. Li, S. Narayanan, M. Sprung, A. Sand, D. R. Lee, and J. Wang. Developing a dedicated GISAXS beamline at the APS. *Synchrotron Radiation Instrumentation, Pts 1 and 2*, 879:1387–1390 1989, 2007.

[154] J. A. Libera. *X-ray Structural Analysis of In-Situ Polynucleotide Surface Adsorption and Metal-Phosphonate Multilayer Film Self-Assembly*. PhD thesis, Northwestern University, 2005.

[155] F. S. Bates and G. H. Fredrickson. Block copolymer thermodynamics - theory and experiment. *Annual Review of Physical Chemistry*, 41:525–557, 1990.

[156] R. E. Bras. *The Stuctural, Mechanical, and Osmotic Properties of Acrylic Triblock Copolymer Gels Determined by Self-Consistent Mean Field Theory and Experiment*. PhD thesis, Northwestern University, 2008.

[157] M. E. Seitz. *Triblock Copolymer Gels - Structure, Fracture Behavior and Application in Ceramic Processing*. PhD thesis, Northwestern University, 2009.

[158] K. J. Henderson. *Mechanisms Dictating Relaxation and Fracture Mechanics in Physically Associated and Ionically Crosslinked Triblock Copolymer Gels*. PhD thesis, Northwestern University, 2011.

[159] Y. Sun, K. R. Shull, D. A. Walko, and J. Wang. Thickness-dependent autophobic dewetting of thin polymer films on coated substrates. *Langmuir*, 27(1):201–8, 2011.

[160] P. Müller-Buschbaum, J. S. Gutmann, J. Kraus, H. Walter, and M. Stamm. Suppression of roughness replication in bilayer films prepared by spin-coating. *Macromolecules*, 33(2):569–576, 2000.

[161] X. S. Hu, S. Narayanan, L. B. Lurio, and J. Lal. Dynamics of polymer bilayer films. *Journal of Non-Crystalline Solids*, 352(42-49):4973–4976, 2006.

[162] S. Hüttenbach, M. Stamm, G. Reiter, and M. Foster. The interface between two strongly incompatible polymers - interfacial broadening and roughening near T_g. *Langmuir*, 7(11):2438–2442, 1991.

[163] P. F. Green, C. J. Palmstrom, J. W. Mayer, and E. J. Kramer. Marker displacement measurements of polymer-polymer interdiffusion. *Macromolecules*, 18(3):501–507, 1985.

[164] Y. K. Jhon, J. J. Semler, and J. Genzer. Effect of solvent quality and chain confinement on the kinetics of polystyrene bromination. *Macromolecules*, 41(18):6719–6727, 2008.

[165] B. Guckenbiehl, M. Stamm, and T. Springer. Interface properties of blends of incompatible polymers. *Physica B-Condensed Matter*, 198(1-3):127–130, 1994.

[166] R. L. McSwain, A. R. Markowitz, and K. R. Shull. Adhesive bonding of glassy polymer surfaces by an ultrathin layer of a semicrystalline polymer. *Journal of Polymer Science Part B-Polymer Physics*, 42(20):3809–3821, 2004.

[167] M. Guvendiren, R. L. McSwain, T. E. Mates, and K. R. Shull. Welding kinetics in a miscible blend of high-T_g and low-T_g polymers. *Macromolecules*, 43(7):3392–3398, 2010.

[168] S. Narayanan, J. Wang, and X. M. Lin. Dynamical self-assembly of nanocrystal superlattices during colloidal droplet evaporation by in situ small angle x-ray scattering. *Physical Review Letters*, 93(13):135503, 2004.

[169] T. P. Bigioni, X. M. Lin, T. T. Nguyen, E. I. Corwin, T. A. Witten, and H. M. Jaeger. Kinetically driven self assembly of highly ordered nanoparticle monolayers. *Nature Materials*, 5(4):265–270, 2006.

[170] Z. Jiang, X. M. Lin, M. Sprung, S. Narayanan, and J. Wang. Capturing the crystalline phase of two-dimensional nanocrystal superlattices in action. *Nano Letters*, 10(3):799–803, 2010.